Max-Planck-Institut
für Meteorologie

MAX-PLANCK-GESELLSCHAFT

International Max Planck Research School
on Earth System Modelling

On the interaction of precipitating convection with its environment and the role of convective organization

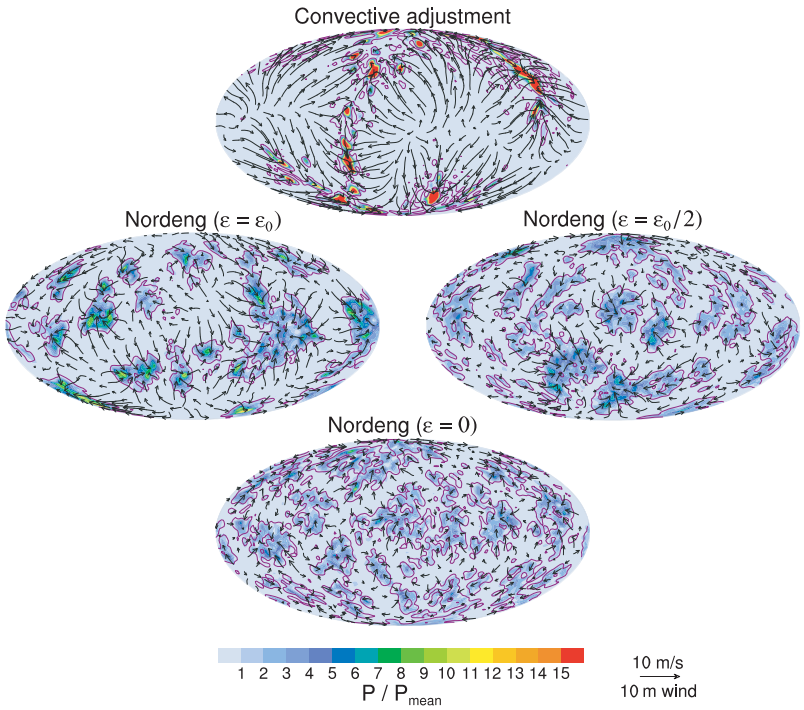

Tobias Benjamin Becker

Hamburg 2018

Berichte zur Erdsystemforschung
Reports on Earth System Science

202
2018

Hinweis

Die Berichte zur Erdsystemforschung werden vom Max-Planck-Institut für Meteorologie in Hamburg in unregelmäßiger Abfolge herausgegeben.

Sie enthalten wissenschaftliche und technische Beiträge, inklusive Dissertationen.

Die Beiträge geben nicht notwendigerweise die Auffassung des Instituts wieder.

Die "Berichte zur Erdsystemforschung" führen die vorherigen Reihen "Reports" und "Examensarbeiten" weiter.

Notice

The Reports on Earth System Science are published by the Max Planck Institute for Meteorology in Hamburg. They appear in irregular intervals.

They contain scientific and technical contributions, including Ph. D. theses.

The Reports do not necessarily reflect the opinion of the Institute.

The "Reports on Earth System Science" continue the former "Reports" and "Examensarbeiten" of the Max Planck Institute.

Anschrift / Address

Max-Planck-Institut für Meteorologie
Bundesstrasse 53
20146 Hamburg
Deutschland

Tel./Phone: +49 (0)40 4 11 73 - 0
Fax: +49 (0)40 4 11 73 - 298

name.surname@mpimet.mpg.de
www.mpimet.mpg.de

Layout

Bettina Diallo and Norbert P. Noreiks
Communication

Copyright

On the interaction of precipitating convection with its environment and the role of convective organization

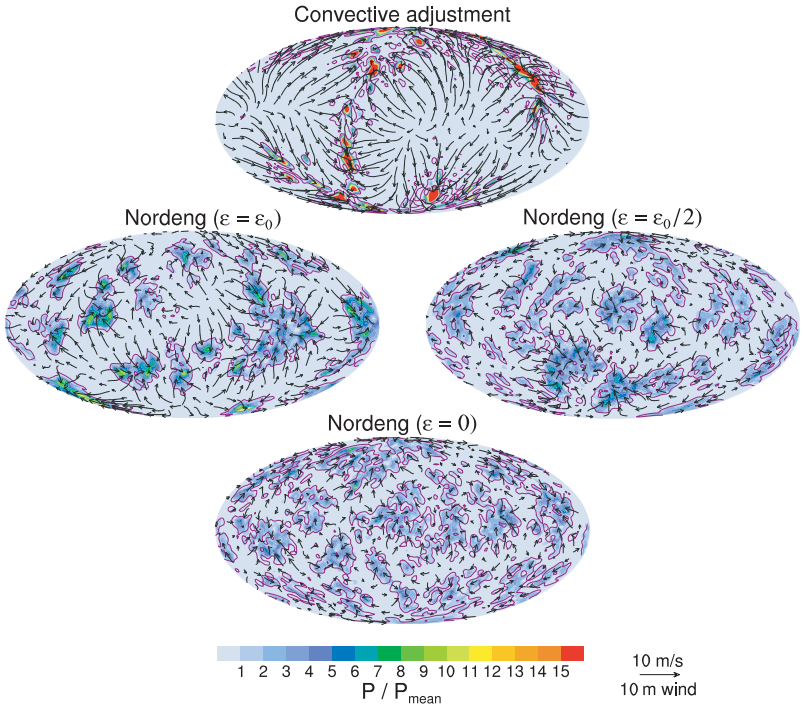

Dissertation with the aim of achieving a doctoral degree
at the Faculty of Mathematics, Informatics and Natural Sciences
Department of Earth Sciences of Universität Hamburg

submitted by

Tobias Benjamin Becker

Hamburg 2018

Tobias Benjamin Becker

Max-Planck-Institut für Meteorologie
Bundesstrasse 53
20146 Hamburg

Tag der Disputation: 06.12.2017

Folgende Gutachter empfehlen die Annahme der Dissertation:

Prof. Dr. Stefan Bühler
Prof. Dr. Bjorn Stevens

Berichte zur Erdsystemforschung / Max-Planck-Institut für Meteorologie 202
Reports on Earth System Science / Max Planck Institute for Meteorology 2018

ISSN 1614-1199

Abstract

Precipitating convection interacts with its environment across a large range of scales. In this thesis, we quantify the role of convective organization in this interaction in two ways: first, we explore how convective organization – in form of convective self-aggregation – is affected by the coupling of convection to its environment, and second, we explore how convective aggregation affects the coupling of convection to the environment.

Using the general circulation model ECHAM6 in a radiative-convective equilibrium (RCE) configuration, we show that the convective parameterization, and in particular the entrainment parameter, control the degree of large-scale convective self-aggregation, and how self-aggregation depends on sea-surface temperature (SST). Self-aggregation is independent of SST when the entrainment rate for deep convection is set to zero or when the convective parameterization is removed from the model. In the former case, convection aggregates very weakly, whereas in the latter case, convection aggregates very strongly. With a nontrivial representation of convective entrainment, large-scale convective self-aggregation depends nonmonotonically on SST. At low SSTs, convection is more aggregated the lower the SST because the relative importance of surface moisture fluxes for the onset of convection increases. At high SSTs, convection is more aggregated the higher the SST because the saturation deficit of entrained air increases with SST.

To investigate how convective aggregation affects the coupling of convection to its environment, we estimate bulk entrainment rates from two convection-permitting RCE simulations with the ICON model, one with unaggregated and one with aggregated convection. We find that bulk entrainment rates are higher in case of aggregated convection because of a strong increase of turbulence in the close environment of the aggregated updrafts. Even though entrainment rate increases with aggregation, we find that aggregated updrafts experience less buoyancy reduction through entrainment because aggregated updrafts are protected by a moist shell.

Bulk entrainment rates estimated in convection-permitting simulations over the tropical Atlantic show that an increase of bulk entrainment rate with aggregation is not confined to RCE simulations. With this more realistic simulation setup, we quantify convective aggregation based on updraft size and updraft isolation, and find that aggregated (large and nonisolated) updrafts have higher entrainment rates than unaggregated (small and isolated) updrafts. Aggregated updrafts also have a moister shell, but as this effect is weaker than in RCE, the moistening of the convective shell is just sufficiently pronounced to balance, with respect to updraft buoyancy, the higher entrainment rate.

Zusammenfassung

Konvektion, die Niederschlag erzeugt, interagiert mit ihrer Umgebung über viele Skalen hinweg. In dieser Doktorarbeit quantifizieren wir die Rolle von konvektiver Organisation in dieser Interaktion auf zwei Weisen: Einerseits erforschen wir, wie konvektive Organisation – in Form von konvektiver Selbstaggregation – von der Wechselwirkung von Konvektion mit ihrer Umgebung beeinflusst wird, andererseits erforschen wir, wie konvektive Aggregation die Wechselwirkung von Konvektion mit ihrer Umgebung beeinflusst.

Mit dem allgemeinen Zirkulationsmodell ECHAM6 in einem Strahlungs-Konvektions-Gleichgewicht (RCE) zeigen wir, dass die Konvektionsparametrisierung und insbesondere der Einmischparameter den Grad der großskaligen konvektiven Selbstaggregation kontrollieren und wie Selbstaggregation von der Meeresoberflächentemperatur (SST) abhängt. Selbstaggregation ist unabhängig von der SST, wenn der Einmischparameter für tiefe Konvektion auf Null gesetzt wird oder wenn die Konvektionsparametrisierung aus dem Modell entfernt wird. Im ersteren Fall aggregiert die Konvektion sehr schwach, wohingegen im letzteren Fall die Konvektion sehr stark aggregiert. Mit einer nichttrivialen Repräsentation von konvektiver Einmischung hängt Selbstaggregation nicht monoton von der SST ab. Bei geringen SSTs ist Konvektion je stärker aggregiert, desto geringer die SST, weil die relative Bedeutung von Verdunstung aus dem Ozean für das Auftreten von Konvektion steigt. Bei hohen SSTs ist Konvektion je stärker aggregiert, desto höher die SST, weil das Sättigungsdefizit von eingemischter Luft mit steigender SST steigt.

Um zu erforschen wie konvektive Aggregation die Wechselwirkung von Konvektion mit ihrer Umgebung beeinflusst, schätzen wir Sammeleinmischraten aus zwei Konvektion auflösenden RCE Simulationen mit dem ICON Modell ab, einmal mit unaggregierter und einmal mit aggregierter Konvektion. Wir entdecken, dass Sammeleinmischraten im Fall von aggregierter Konvektion höher sind, weil die Turbulenz in der unmittelbaren Umgebung von Aufwinden höher ist. Obwohl Einmischraten mit zunehmender Aggregation steigen, erfahren die aggregierten Aufwinde eine geringere Auftriebsreduktion durch Einmischung, weil aggregierte Aufwinde durch eine feuchte Hülle geschützt sind.

Sammeleinmischraten, abgeschätzt aus Konvektion auflösenden Simulationen über dem tropischen Atlantik, zeigen, dass ein Anstieg der Sammeleinmischrate mit zunehmender Aggregation nicht auf RCE Simulationen beschränkt ist. Mit dieser realistischeren Simulationskonfiguration quantifizieren wir konvektive Einmischraten basierend auf Aufwindgröße und Aufwindisolation und entdecken, dass aggregierte (große und nicht-isolierte) Aufwinde höhere Einmischraten als unaggregierte (kleine und isolierte) Aufwinde haben. Aggregierte

Aufwinde haben auch eine feuchtere Hülle, aber weil dieser Effekt schwächer ausgeprägt ist als in RCE, reicht die feuchtere Hülle nur gerade aus, um die höhere Einmischrate bezüglich des Aufwindauftriebs auszugleichen.

Contents

Chapter 1

Introduction

> All models are wrong, but some are useful.
>
> *(George Box, 1978)*

Climate science, based on the principles of physics, is still a rather young science. Envisioned by Vilhelm Bjerknes and Lewis Fry Richardson in the early 20th century, the first numerical weather prediction (NWP) models were developed in the 1950s (*Charney et al.*, 1950; *Bergthorsson et al.*, 1955). In the same decade, the first general circulation model (GCM) was created (*Phillips*, 1956), followed a decade later by the first coupled atmosphere-ocean GCM (*Manabe and Bryan*, 1969). By now, climate science found evidence that, based on observations and models, global mean near-surface temperature has been rising compared to the preindustrial era, and that anthropogenic greenhouse gas emissions are responsible for the rising temperatures. According to the IPCC Fifth Assessment Report (AR5), it is extremely likely (likelihood higher than 95 %) that human influence has been the dominant cause of the observed warming since the mid-20th century (*IPCC*, 2013). However, uncertainty remains in estimating equilibrium climate sensitivity (ECS), the equilibrium state warming in response to a doubling of the atmospheric CO_2 concentration. Based on observed climate change, paleoclimate evidence and climate models, ECS is likely (likelihood higher than 66 %) in the range 1.5 to 4.5 °C, as

stated in IPCC AR5 (*Collins et al.*, 2013). Most of the spread in model-based estimates of ECS can be attributed to the response of clouds to warming, with the response of low clouds deemed especially important and also uncertain (e. g., *Bony et al.*, 2004; *Bony and Dufresne*, 2005; *Randall et al.*, 2007; *Soden and Vecchi*, 2011; *Webb et al.*, 2013; *Vial et al.*, 2013; *Sherwood et al.*, 2014).

The response of clouds to warming is uncertain in climate models mostly because clouds cannot be resolved, and thus need to be parameterized. Parameterizations are essentially conceptual models that encapsulate our understanding of how an unresolved process can be expressed as a function of variables that are resolved by the model. However, most of the processes that clouds depend upon, like moist convection, are also unresolved in GCMs, and thus need to be parameterized as well (*Webb et al.*, 2015). Because of the complexity and interdependence of the involved processes, little progress was made over the last decades to reduce key uncertainties in the representation of moist convection and cloud formation in GCMs (*Stevens and Bony*, 2013a), even though the complexity of climate models strongly increased. As a way forward, the World Climate Research Programme (WCRP) Grand Challenge Initiative on Clouds, Circulation and Climate Sensitivity formulated 'Four Questions' the scientific community should focus on to accelerate progress (*Bony et al.*, 2015). One of the questions deals with the organization of convection and postulates that we should improve our understanding of the vast variety of ways and scales convection can organize on.

In this thesis, we investigate how precipitating convection interacts with its environment, focusing both on how convective organization is affected by this interaction, and in turn how organization affects this interaction. For this purpose, we investigate how convective organization depends on the convective parameterization in GCMs, and compare to high-resolution models that resolve convection. As an introduction to the topic, the role of precipitating convection in the climate system is explained in the next section, followed by a discussion of barriers to an improved understanding of precipitating convection, and how these barriers might be overcome. In the last section of this introduction, the specific research objectives addressed in this thesis are formulated and explained.

1.1. The role of precipitating convection in the climate system

To understand the climate system, the most important processes within the climate system need to be identified first. If the atmosphere contained no greenhouse gases and were not allowed to convect, the Earth system would be in a state of pure radiative equilibrium, and net longwave outgoing radiation would balance net shortwave incoming radiation everywhere in the atmosphere. However, the resulting temperature profile would be unstable to dry convection, and dry convection would adjust the temperature lapse rate to a dry adiabat. When adding greenhouse gases like water vapor or CO_2, the atmosphere be-

comes less transparent to longwave radiation because greenhouse gases absorb and emit longwave radiation. As a consequence, the net longwave cooling reduces at the surface, while longwave cooling intensifies in the atmosphere. Precipitating moist convection can balance the atmospheric longwave cooling through latent heat release: air parcels in rising convecting plumes expand and cool, and after saturation and cloud formation, they follow the moist adiabat because water vapor condenses and releases latent heat, while hydrometeors form, merge and precipitate. In the tropics, the balance between convective heating and radiative cooling – the radiative-convective equilibrium (RCE) – is a surprisingly accurate simplification of the lowest layer of Earth's atmosphere, the troposphere (e. g., *Dines*, 1917; *Manabe and Strickler*, 1964; *Manabe and Wetherald*, 1967; *Ramanathan and Coakley*, 1978; *Popke et al.*, 2013).

RCE is a good approximation for the tropical troposphere because gravity waves are more important than rotational effects in the tropics, as the Coriolis force is small. Therefore, perturbations in air density (essentially in temperature) are damped and spread by gravity waves (e. g., *Emanuel et al.*, 1994; *Sobel and Bretherton*, 2000). Thus, horizontal temperature gradients are weak in the tropics, and the vertical temperature profile is dictated by deep convection.

Water vapor is the most active greenhouse gas in the troposphere and, at the same time, it is not well mixed. Water vapor is not well mixed because the relative humidity of an air parcel depends on its history and, more specifically, on the temperature at which the air parcel was last saturated. Because of that, the water vapor distribution strongly affects the profile of longwave cooling in the troposphere, as well as the hydrological cycle and the large-scale circulation (*Stevens and Bony*, 2013b).

As soon as convection leads to saturation and cloud formation, both shortwave heating and longwave cooling are strongly affected. Longlasting stratiform clouds, which can form when moist air is detrained from convective updrafts, have a particularly pronounced effect. Clouds can either cool or warm the climate system, depending on the height at which they form, the time of day and their position relative to other clouds. This strong diversity in the response, together with the complexity of the processes that cause the formation of clouds, explains why the response of clouds to a changing climate is a key uncertainty in climate models (*Stevens and Bony*, 2013a).

Observations show that convection which grows deep is mostly dynamically forced (*Hohenegger and Stevens*, 2013; *Kumar et al.*, 2013), but local moistening can also be an important precondition for deep convection, as deep convection is very sensitive to relative humidity in the free troposphere (e. g., *Redelsperger et al.*, 2002; *Zhang et al.*, 2003; *Derbyshire et al.*, 2004). The reason why convection is sensitive to its environment is that air from the environment gets laterally entrained into convecting plumes, changing the temperature and humidity of the rising air. Updraft buoyancy is reduced more strongly if the relative humidity in the neighborhood of updrafts is small, as dry air causes more

Figure 1.1.: Deep convection organizing in several thunderstorms over the Maritime Continent in the late afternoon on August 5th, 2014, viewed from the International Space Station.[1]

cloud condensate to evaporate, cooling the updraft. Because of that, deep convection is more likely to form in regions that have already been premoistened by shallower convection (e. g., *Esbensen*, 1978; *Dauhut et al.*, 2017).

As convection favors a moist environment, convection often organizes in clusters. Organized convection ranges from isolated convective cells to multicellular thunderstorms (as in Figure 1.1), squall lines, mesoscale convective complexes (e. g., *Laing and Fritsch*, 1997; *Houze*, 2004), tropical depressions growing into tropical cyclones, and global systems like the intertropical convergence zone (ITCZ) or the Madden-Julian Oscillation (MJO). Possible drivers of organization are the large-scale forcing, the interaction with the large-scale circulation, or the self-organization of convection due to an evolving convection-driven secondary circulation. Convective organization modulates the cloud size distribution, the amount and pattern of precipitation, as well as the moisture distribution, causing a drying in nonconvective regions that amplifies outgoing longwave radiation (e. g., *Bretherton et al.*, 2005; *Tobin et al.*, 2012). Differences in convective heating or longwave cooling are balanced by large-scale vertical motion, and thus the large-scale circulation is also affected by convective organization (e. g., *Houze*, 1982). In light of all the processes influenced by

[1] The photo was downloaded on October 17th, 2017 from:
https://eol.jsc.nasa.gov/SearchPhotos/photo.pl?mission=ISS040&roll=E&frame=88891

organization, it is not surprising that convective organization is capable to alter climate sensitivity. An increase of convective organization with temperature is found in observations (*Tan et al.*, 2015) and in some modeling studies (e. g., *Khairoutdinov and Emanuel*, 2010; *Wing and Emanuel*, 2014; *Coppin and Bony*, 2015; *Hohenegger and Stevens*, 2016), though other modeling studies only find a very weak temperature dependence of organization (*Wing and Cronin*, 2016; *Holloway and Woolnough*, 2016).

1.2. Barriers to an improved understanding of precipitating convection

The last section has shown that precipitating convection is very complex because it interacts with many different processes across many scales. In GCMs, convective processes are not resolved and thus have to be represented by a convective parameterization, which is difficult because of the aforementioned complexity of convection. The original purpose of a convective parameterization was just to represent the vertical heat transport associated with convection (e. g., *Manabe and Strickler*, 1964). However, in the following decades, a large number of diverse convective parameterizations has been developed, and the number of processes represented or at least affected by the convective parameterization has strongly increased (*Arakawa*, 2004): convective mass transport, generation of liquid and ice phase cloud, interactions with the subcloud layer, interactions with radiation, and mechanical interactions with the mean flow. Because of this broadening of scope, the convective parameterization interacts almost with the entire model physics.

The most essential parts of a convective parameterization are the trigger conditions (e. g., *Rochetin et al.*, 2014; *Peters et al.*, 2017) and the closure assumption (e. g., *Arakawa*, 2004). Not all convection schemes have trigger conditions, some adjust the temperature profile instantaneously towards equilibrium (e. g., *Manabe et al.*, 1965). However, with trigger conditions, the location and timing of convection can be better controlled because the coupling of convection to its local environment, to the surface fluxes and to the large-scale circulation can be better represented (e. g., *Suhas and Zhang*, 2014). For the closure assumption, which essentially determines the strength of convection, two different approaches exist. The first approach assumes that convection quickly responds to the production of convective instability through convective adjustment (*Manabe et al.*, 1965), resulting in a quasi-equilibrium closure (*Arakawa and Schubert*, 1974) based on convective available potential energy (CAPE). The CAPE closure is directly related to buoyancy, which is advantageous because convection feels its environment primarily through the buoyancy force. However, as CAPE is a very local quantity, mostly depending on the temperature in the boundary layer, the CAPE closure has the problem that it has no direct link to the large-scale circulation, especially over land. Furthermore, the quasi-equilibrium assumption is often not justified, especially on small scales. The second

approach assumes that large-scale moisture supply is balanced by the consumption of moisture through convection (*Ooyama*, 1964; *Charney and Eliassen*, 1964; *Kuo*, 1965), resulting in a moisture-convergence closure (*Tiedtke*, 1989).

Convection can only be parameterized if it can be well-defined as a function of variables that are resolved by the model, and if the sample size is large enough for a statistical representation. Especially at high resolution, in the so-called gray zone (with a grid spacing below 25 km), a statistical treatment of convection gets questionable because too few convective entities are present for the computation of meaningful averages. Thus, at high resolution the problem with the convective parameterization is that a statistical representation of convection under different grid-scale forcings is not always justified (e. g., *Arakawa*, 2004). A proposed solution is to average the large-scale state over several grid boxes (*Keane and Plant*, 2012).

To better reproduce observations, parameterizations need to be tuned (e. g., *Mauritsen et al.*, 2012). In case of the convective parameterization, the problem is that, to improve the representation of the mean state, like the top-of-atmosphere (TOA) radiation balance or the precipitation climatology, the tuning often happens within the coupled model (*Hourdin et al.*, 2017). This leads to compensating errors in the model, and to a barrier to an improved understanding, as it gets difficult to improve the model. Even though a process might be better represented by a new parameterization, the skill of the model relative to observations will get worse, as model errors will not compensate anymore. A better approach would be to perform the tuning outside the coupled model on the process level. This can be done with an adequate evaluation of the involved processes (e. g., *Klingaman et al.*, 2017; *Peters et al.*, 2017), and a focus on shorter timescales, like daily (*Stratton and Stirling*, 2012; *Peters et al.*, 2017) or intraseasonal (*Klingaman and Woolnough*, 2014; *Zhu and Hendon*, 2015) timescales.

A process that is of high relevance for the parameterization of convection, which this thesis will focus on, is the entrainment of environmental air into the convective updraft, first described by *Stommel* (1947). The entrainment parameter is exceptionally important for the climate and climate change simulated by the model (e. g., *Knight et al.*, 2007; *Klocke et al.*, 2011; *Sherwood et al.*, 2014; *Tomassini et al.*, 2015), and is often used as a tuning parameter (*Mauritsen et al.*, 2012) because it alters the updraft buoyancy and the updraft mass flux, and thus affects the vertical energy transport, static stability and the large-scale circulation. The entrainment parameter also affects the organization of convection, as convection is more strongly coupled to the free tropospheric relative humidity if the entrainment rate is large (e. g., *Oueslati and Bellon*, 2013; *Arnold and Randall*, 2015; *Tompkins and Semie*, 2017).

The entrainment parameter is challenging to constrain because it is very difficult to observe. Entrainment has been estimated based on aircraft measurements (e. g., *Warner*, 1955; *Raga et al.*, 1990), by combining observed large-scale heat and moisture budgets

(*Yanai et al.*, 1973), in water tank experiments (e. g., *Morton et al.*, 1956; *Turner*, 1963), and, more recently, from convection-permitting models (e. g., *Siebesma and Cuijpers*, 1995; *Siebesma et al.*, 2003; *Romps*, 2010; review article by *de Rooy et al.*, 2013). However, entrainment estimates are still uncertain, not only because entrainment cannot be measured directly, but also because it is very variable and strongly depends on the local conditions, especially in the transition phase between shallow and deep convection (e. g., *Khairoutdinov and Randall*, 2006; *Del Genio and Wu*, 2010; *de Rooy et al.*, 2013). This explains why the translation of observed entrainment rates into the bulk mass flux framework, which averages over an ensemble of updrafts, is problematic.

Given the issues with the convective parameterization discussed in the previous paragraphs, it is not surprising that some key problems remain. First, parameterized convection depends too weakly on the large-scale circulation. In fact, as parameterized convection often occurs in the wrong place, the large-scale circulation is biased (e. g., *Marsham et al.*, 2013; *Siongco et al.*, 2017; *Hohenegger et al.*, 2015). Second, convective parameterizations struggle to get both the mean state and the variability of convection right (*Mapes and Neale*, 2011; *Kim et al.*, 2011). If the entrainment rate is large, the mean state is biased because too much instability accumulates, and if the entrainment rate is small, the variability is underestimated. This problem is known as the entrainment dilemma (e. g., *Mapes and Neale*, 2011). Third, the timing of convective initiation over tropical land is wrong, with precipitating convection peaking too early during the day in many GCMs (e. g., *Bechtold et al.*, 2004; *Lawrence and Slingo*, 2005; *Stratton and Stirling*, 2012). And fourth, convection is too strongly coupled to the latent heat flux. Because of that, parameterized convection both favors precipitation over wet rather than dry soil (e. g., *Hohenegger et al.*, 2009; *Taylor et al.*, 2012), and over the ocean rather than over land in coastal regions (e. g., *Nguyen et al.*, 2017).

1.3. The way forward: How the understanding of precipitating convection can be improved

So how can the understanding of precipitating convection be improved, despite the complexity of convection and the problems that arise when parameterizing it? A shift of priority seems sensible. Rather than focusing on developing a model that simulates the mean state realistically, by tuning the coupled system, we should focus on a better representation of the coupling of convection to the large-scale circulation, and thus on a better understanding of the underlying physical processes.

A first approach how the understanding of the physical processes can be advanced is by putting more effort and manpower into improving the convective parameterization (e. g., *Jakob*, 2010; *Sherwood et al.*, 2013; *Holloway et al.*, 2014). First, a non-local parameterization would improve the representation of convection both in time (memory) and in space

(organization). A better representation of convective organization in the model could solve the entrainment dilemma (*Mapes and Neale*, 2011), and could represent the interaction of convection with the local environment more realistically (*Moncrieff*, 2004; 2010; *Redelsperger et al.*, 2000; *Grandpeix and Lafore*, 2010; *Tobin et al.*, 2013). In this thesis, we improve understanding of the processes that dominate this interaction, and enlighten the connection to convective organization. Second, instead of using a quasi-equilibrium closure, the closure should tie convection more closely to an observable quantity that characterizes the large-scale circulation (*Peters et al.*, 2013; *Davies et al.*, 2013; *Dorrestijn et al.*, 2015), for example the large-scale moisture distribution at mid levels. Third, a stochastic parameterization would have the advantage that it could better represent the large-scale state and history (*Berner et al.*, 2012; *Peters et al.*, 2013). Such a parameterization would also improve the scale-awareness at high resolution (*Sakradzija et al.*, 2016), which could reduce problems in the gray zone (*Plant and Craig*, 2008; *Arakawa and Wu*, 2013). And fourth, multi-plume parameterizations can better represent the cloud size distribution, in particular the transition between shallow and deep convection (e. g., *Wagner and Graf*, 2010; *Mapes and Neale*, 2011; *Guo et al.*, 2015).

A second approach how the understanding of the physical processes can be improved is by avoiding a parameterization of convection, and instead resolving convection explicitly on the grid scale. With increasing computer power, global cloud-resolving models (GCRMs), which explicitly resolve deep convection and thus do not need a convective parameterization anymore, become feasible. The oldest GCRM, the Nonhydrostatic ICosahedral Atmospheric Model (NICAM), has already existed for more than 10 years (*Tomita and Satoh*, 2004; *Satoh et al.*, 2008; 2012), and by now, global simulations with less than 1 km grid spacing are possible (*Miyamoto et al.*, 2013). The disadvantage of these global ultra-high resolution simulations is that they can only be run for very short time spans, making it difficult to study climate change. Thus, other popular approaches are near-global cloud-resolving simulations (*Bretherton and Khairoutdinov*, 2015; *Narenpitak et al.*, 2017), and global models with superparameterized convection which embed 2-dimensional CRM in each large-scale grid cell (e. g., *Grabowski and Smolarkiewicz*, 1999; *Khairoutdinov and Randall*, 2001; *Randall et al.*, 2003). All these models share the advantage that they avoid the problems introduced by a convective parameterization, as they explicitly resolve individual convective clouds and mesoscale organization.

A third approach how the understanding can be improved is by comparing models of different complexity, ranging from single-column models (SCMs) to GCMs, limited-area CRMs, and GCRMs. A model framework that can bridge the gap between all these models of different complexity is the radiative-convective equilibrium framework (*Wing et al.*, 2017a), which we will also use in this thesis to compare GCM and CRM simulations. SCMs, GCMs, CRMs and GCRMs can use the same horizontally homogeneous boundary conditions, allowing not only for an excellent comparability, but also for an undistracted

analysis of convection and convective organization in the absence of large-scale heterogeneity and forcing. In recent years, many studies have used the RCE framework in CRMs (e. g., *Tompkins and Craig*, 1998; *Bretherton et al.*, 2005; *Wing and Emanuel*, 2014) and GCMs (*Held et al.*, 2007; *Popke et al.*, 2013; *Becker and Stevens*, 2014). In particular, these studies enhance understanding of how subgrid-scale processes influence the coupling of clouds and precipitating convection to the large-scale environment (e. g., *Satoh and Matsuda*, 2009), and how this coupling depends on temperature (e. g., *Muller et al.*, 2011; *Romps*, 2011; *Singh and O'Gorman*, 2013; *Hohenegger and Stevens*, 2016). The central topic in these studies is the role of convective self-aggregation in RCE (*Wing et al.*, 2017b, and references therein), but some findings are quite model- and setup-dependent, and open questions remain how these findings can be interpreted with respect to the real climate system. Thus, the important next step is to test whether results can be reproduced in a more realistic simulation setup (e. g., *Holloway*, 2017), or even better, whether hypotheses can be verified with observations (e. g., *Tobin et al.*, 2012; *Stein et al.*, 2017; *Holloway*, 2017). In this context, extensive field experiments that directly link modeling studies and observations, like the Next Generation Aircraft Remote Sensing for Validation (NARVAL) campaigns (*Klepp et al.*, 2015; *Stevens et al.*, 2016) or the EUREC^{4}A campaign planned for 2020 (*Bony et al.*, 2017), are promising ways forward.

A fourth approach how the understanding can be enhanced is with model intercomparison projects, for example the Radiative-Convective Equilibrium Model Intercomparison Project (RCE-MIP, *Wing et al.*, 2017a). Model intercomparison projects have the advantage that shortcomings of individual models, as well as robust behavior among models, can be identified. Results in this thesis (in Chapter 2) contributed to a small RCE model intercomparison study that compared three RCE-GCMs. We found that a 'stability iris effect' is present in all models: as the climate warms, upper tropospheric stability increases, reducing the convective outflow and decreasing the tropical anvil cloud amount (*Bony et al.*, 2016).

1.4. Research Objectives

The goal of this thesis is to gain a better understanding of the interaction of precipitating convection with its environment, and to quantify the role of convective organization – in form of convective aggregation – in this interaction. We analyze the interaction in two ways. First, we investigate how convective aggregation is affected by the coupling of convection to the environment, in particular how this coupling depends on the entrainment parameter in the convective parameterization. And second, we investigate how convective aggregation affects the coupling of convection to the environment, and more specifically how the entrainment rate depends on the degree of convective aggregation. We approach these research objectives from a modeling perspective, using a general circulation model

in the RCE framework, a convection-permitting model in the RCE framework, and a convection-permitting model over the tropical Atlantic. The three main research questions are:

- **How does the convective parameterization control the temperature dependence of large-scale convective self-aggregation?**

  With this research question, we combine two aspects that have only been studied in separation before. First, an increase of the entrainment parameter has been shown to strengthen the coupling of convection to its local environment, especially to free tropospheric humidity (e. g., *Möbis and Stevens*, 2012; *Oueslati and Bellon*, 2013), and RCE simulations have shown that with a higher entrainment rate, convection is more aggregated (*Arnold and Randall*, 2015). Second, many RCE studies have examined how convective aggregation depends on sea-surface temperature (SST), mostly in convection-permitting simulations (e. g., *Wing and Emanuel*, 2014; *Reed et al.*, 2015; *Wing and Cronin*, 2016; *Holloway and Woolnough*, 2016), but also in GCMs (*Coppin and Bony*, 2015; *Arnold and Randall*, 2015). While some of these studies find that convective aggregation strongly increases with SST (e. g., *Wing and Emanuel*, 2014; *Reed et al.*, 2015; *Arnold and Randall*, 2015), other studies do not find a strong SST dependency (*Wing and Cronin*, 2016; *Holloway and Woolnough*, 2016). In Chapter 2, we combine these two aspects, and ask how the convective parameterization and the entrainment parameter affect the dependence of large-scale convective self-aggregation on SST. To understand which processes sustain convective aggregation, we use a fully-fledged GCM in the radiative-convective equilibrium framework. With a focus on the stationary state, we infer from the large-scale statistics how convection couples to the large-scale circulation. One important property that we extensively study is the vertically integrated distribution of moist static energy.

- **How does the bulk entrainment rate depend on the degree of convective aggregation?**

  With this research question, the prime objective is to understand how the interaction of precipitating convection with its environment depends on the degree of convective aggregation. The motivation behind this research question is that mesoscale convective organization is still not represented in most convective parameterizations, though some recent studies suggest to represent organization in convective parameterizations based on a new prognostic variable, to escape the entrainment dilemma (*Mapes and Neale*, 2011; *Tobin et al.*, 2013). Previous studies found that entrainment scales with the inverse of the largest eddy sizes in the updraft (*Morton et al.*, 1956; *Turner*, 1963; *Siebesma*, 1996), and updrafts are wider and steadier with aggregated

convection than with unaggregated convection (e. g., *Mapes and Neale*, 2011). Other studies found that aggregated updrafts have a moister local environment than unaggregated updrafts because the spacing between updrafts reduces (e. g., *Mapes and Neale*, 2011; *Feng et al.*, 2015). Based on all these studies, it can be hypothesized that the entrainment rate decreases with aggregation and that entrainment is less efficient in reducing updraft buoyancy in the aggregated state because aggregated updrafts have a moist environment. However, these two hypotheses have not been verified by any high-resolution, convection-permitting simulations. Thus, in Chapter 3, our aim is to investigate how entrainment depends on the degree of convective aggregation in a controlled environment, comparing two convection-permitting simulations in the radiative-convective equilibrium framework, one with unaggregated convection, and the other one with aggregated convection. The two simulations have identical boundary conditions, but are started from different initial conditions. We calculate bulk entrainment following *Betts* (1975), with the help of a 'radioactive tracer' that we design in a way that it is conserved in convective updrafts, and significantly higher in updrafts than in their environment.

- **What does the bulk entrainment rate over the tropical Atlantic depend on?**

  With this research question, the main objective is to investigate whether the findings from Chapter 3, in which we investigate how entrainment depends on convective aggregation, can be extended to more realistic simulation setups. For this purpose, Chapter 4 analyzes entrainment in convection-permitting simulations over the tropical Atlantic. We calculate bulk entrainment with frozen moist static energy as a tracer, which is almost conserved in moist convection below the freezing level. To investigate how entrainment depends on convective aggregation in those realistic simulations, we analyze how entrainment rate and updraft buoyancy depend on the size of updrafts, as well as on the spacing between updrafts.

In Chapter 5, the main findings of this thesis are summarized by revisiting the three main research questions, followed by some concluding remarks and an outlook.

Chapter 2

Imprint of the convective parameterization and sea-surface temperature on large-scale convective self-aggregation[1]

> Hence, our truth is at the intersection of independent lies.
>
> *(Richard Levins, 1966)*

In this chapter, we use radiative-convective equilibrium simulations with the general circulation model ECHAM6 to explore to what extent the dependence of large-scale convective self-aggregation on sea-surface temperature (SST) is driven by the convective parameterization. Within the convective parameterization, we concentrate on the entrainment parameter and show that large-scale convective self-aggregation is independent of SST when the entrainment rate for deep convection is set to zero or when the convective parameterization is removed from the model. In the former case, convection always aggregates very weakly, whereas in the latter case, convection always aggregates very strongly. With a nontrivial representation of convective entrainment, large-scale convective self-

[1] This chapter has been published with minor modifications as: Becker, T., B. Stevens and C. Hohenegger (2017): Imprint of the convective parameterization and sea-surface temperature on large-scale convective self-aggregation. J. Adv. Model. Earth. Syst., **9**(2), 1488–1505, doi:10.1002/2016MS000865.

aggregation depends nonmonotonically on SST. For SSTs below 295 K, convection is more aggregated the lower the SST because large-scale moisture convergence is relatively small, constraining convective activity to regions with high wind-induced surface moisture fluxes. For SSTs above 295 K, convection is more aggregated the higher the SST because entrainment is most efficient in decreasing updraft buoyancy at high SSTs, amplifying the moisture-convection feedback. When halving the entrainment rate, convection is less efficient in reducing updraft buoyancy, and convection is less aggregated, in particular at high SSTs. Despite most early work on self-aggregation highlighted the role of nonconvective processes, we conclude that convective self-aggregation and the global climate state are sensitive to the convective parameterization.

2.1. Introduction

Parameterizing moist convection is one of the greatest challenges in climate system modeling (e. g., *Randall et al.*, 2003; *Arakawa*, 2004; *Stevens and Bony*, 2013a; *Bony et al.*, 2015). Moist convection is difficult to parameterize because it is strongly coupled to the environment through a diversity of processes, ranging from gravity waves to radiative transfer, moisture perturbations and surface fluxes (e. g., *Bretherton and Smolarkiewicz*, 1989; *Bony and Emanuel*, 2005). The coupling occurs on a variety of space and time scales, which makes it difficult to separate convective processes and convection-controlling processes. Here we analyze radiative-convective equilibrium (RCE) simulations to understand how the convective parameterization, and in particular the entrainment parameter, controls the interaction of moist convection with the large-scale circulation, and how the governing mechanisms depend on the climate state.

With the RCE approach, the insolation and surface properties are assumed to be homogeneous and the planet is assumed to be nonrotating. The RCE approach has the advantages that it ensures a focus on the basic drivers of convection – radiation, tropospheric humidity, surface fluxes, and the convection-driven large-scale circulation – and that it is applicable in a hierarchy of models, bridging the gap between models that simulate convection and models that parameterize it. RCE has been used as a paradigm to understand climate for a long time (*Ramanathan and Coakley*, 1978, and references therein), but until recently the RCE framework has not been used in global models that parameterize convection. Running a general circulation model (GCM) in the RCE setup, as we do here, *Popke et al.* (2013) showed that RCE provides a good analog to the structure of the tropical circulation. Thus, RCE is emerging as an exciting new approach to address how parameterized convection interacts with its large-scale environment across all scales, and how the convective parameterization influences this coupling.

Convective organization may influence the interaction of convection and large-scale circulation. Observations show that organization emerges on all space scales in the climate

system, with mesoscale organization contributing about 50 % to tropical precipitation (*Nesbitt et al.*, 2000). Organization, and more specifically convective aggregation, can be associated with a drying in the free troposphere and a decrease in low to midlevel cloud fraction in nonconvecting areas (*Tobin et al.*, 2012). The expansion of dry areas causes an increase in outgoing longwave radiation (OLR) and an increase in shortwave radiation absorbed by the surface. Convective aggregation thus modulates the strength and pattern of precipitation, and also influences the atmospheric moisture distribution, the radiation budget and the large-scale circulation.

RCE studies with convection-permitting models show that convective self-aggregation is favored if domain size is larger than 200 km and if resolution is coarser than 2 km (*Muller and Held*, 2012; *Muller and Bony*, 2015). Assuming that the mechanisms responsible for convective self-aggregation on the mesoscale in convection-permitting models also apply on the large scale in GCMs, this finding suggests that convection would always be extremely aggregated in GCMs. However, the few studies that use GCMs in the RCE configuration find a more diverse representation of RCE compared to their convection-permitting counterparts (*Coppin and Bony*, 2015; *Arnold and Randall*, 2015; *Bony et al.*, 2016). To some extent, the increase in diversity can be attributed to the convective parameterization, and to assumptions therein that have an impact on large-scale convective self-aggregation. The entrainment parameter has been shown to affect the coupling of convection to the large-scale flow in aquaplanet simulations (e. g., *Möbis and Stevens*, 2012; *Oueslati and Bellon*, 2013), and RCE simulations suggest that convective self-aggregation increases with the entrainment rate (*Arnold and Randall*, 2015).

Another research question is how convective self-aggregation depends on the prescribed SST. Here the literature is less conclusive, with seemingly contradictory findings across studies. In two convection-permitting studies, convective self-aggregation is almost independent of SST (*Wing and Cronin*, 2016; *Holloway and Woolnough*, 2016), in other studies, both with convection-permitting models and GCMs, convective self-aggregation increases with SST (*Khairoutdinov and Emanuel*, 2010; *Wing and Emanuel*, 2014; *Arnold and Randall*, 2015; *Reed et al.*, 2015), and with one GCM, convective self-aggregation even depends nonmonotonically on SST (*Coppin and Bony*, 2015). The mechanisms that are responsible for the SST dependence include clear-sky longwave radiative feedbacks (*Emanuel et al.*, 2014), radiation-circulation coupling (*Coppin and Bony*, 2015), and WISHE-circulation coupling (*Coppin and Bony*, 2015). In this chapter, we combine both research questions, and analyze how the convective parameterization, and in particular the entrainment rate for deep convection, affects the dependence of large-scale convective self-aggregation on SST.

In Chapter 2.2, we sketch the main features of the convective parameterization, and outline our experimental strategy. Chapter 2.3 sets some terminology and gives a short overview over some results, whereas Chapter 2.4 discusses how the RCE climate is me-

diated by assumptions in the convective parameterization – directly and through their effect on convective self-aggregation. In Chapter 2.5, the response of the RCE climate to SST changes is discussed. The sensitivity of convective self-aggregation to SST and convection scheme arises as a particular point of emphasis. Chapter 2.6 briefly discusses the effect of self-aggregation on climate sensitivity. The study is summarized and concluded in Chapter 2.7.

2.2. Methods

2.2.1. Convective parameterization

In ECHAM6 (*Stevens et al.*, 2013), the convective parameterization of *Nordeng* (1994) is used by default; hereafter "Nordeng" refers both to this parameterization and to model configurations that use it. To test ideas as to the cause of differences among models concerning the SST dependence of convective self-aggregation, three additional representations of convection are investigated. Two representations are based on Nordeng, with the only difference that the entrainment rate for deep convection is halved (HalfEntrN) or set to zero (NoEntrN), respectively, and one representation prohibits all subgrid-scale convection (NoCnvPm), in analogy to the Selected Process On/Off Klima Intercomparison Experiment (SPOOKIE, *Webb et al.*, 2015). The NoCnvPm setup can be envisioned as a configuration where the entrainment rate is set to infinite for every type of parameterized convection.

The Nordeng convection scheme uses the mass flux approach (*Arakawa and Schubert*, 1974; *Tiedtke*, 1989) and differentiates between shallow, midlevel and deep convection. Because midlevel convection is very rarely triggered, we do not discuss it further. The convection scheme is triggered if total moisture convergence below cloud base is positive, if updraft humidity is higher than in the environment and if the updraft is positively buoyant. For the triggering of deep convection, column-integrated total moisture convergence must exceed surface evaporation by 10 % and cloud depth has to be more than 200 hPa in the first updraft calculation. For deep convection, the closure for the cloud base mass flux is based on convective available potential energy (CAPE). CAPE is relaxed to zero with a prescribed time scale, which is 7200 s when using the spectral resolution T63 (corresponding to 1.875° resolution). The change of net upward mass flux M_{up} with height depends on two qualitatively different types of mixing, turbulent (trb) and organized (org) mixing, expressed in the form of entrainment (ϵ) and detrainment (δ) of cumulus mass:

$$\frac{\partial M_{\mathrm{up}}}{\partial z} = \epsilon_{\mathrm{trb}} + \epsilon_{\mathrm{org}} - \delta_{\mathrm{trb}} - \delta_{\mathrm{org}}. \tag{2.1}$$

By definition, turbulent entrainment is proportional to the mass flux itself, with different constants of proportionality for shallow and deep convection. Turbulent entrainment

matches turbulent detrainment below the detrainment level z_D and turbulent entrainment is set to zero above z_D. Organized entrainment and detrainment are enabled only in case of deep convection. Organized entrainment is parameterized as a function of updraft buoyancy, whereas organized detrainment is zero below the level of neutral buoyancy of a prescribed updraft, and is vertically distributed with a sine function above that level. In the simulations HalfEntrN and NoEntrN, where the entrainment rate for deep convection (hereafter entrainment rate) is changed by a certain factor, turbulent and organized entrainment as well as turbulent detrainment are multiplied by that factor. Organized detrainment is not changed to avoid that all of the detrainment is constrained to one level in NoEntrN.

For more details on the Nordeng convection scheme, the reader is referred to *Möbis and Stevens* (2012) because the implementation in ECHAM6 differs in some important details from what is described in the original publications.

2.2.2. Simulations

In all simulations, we use the general circulation model ECHAM 6.3 in a radiative-convective equilibrium configuration with T63 spectral resolution and 47 levels in the vertical. The main differences between this version of ECHAM6 and the version described by *Stevens et al.* (2013) are a correction to the faulty implementation of the cloud scheme that was identified in their paper, a better treatment of the thermodynamics in the cloud and convective parameterization to address energy conservation, and a different treatment of cloud-radiation interactions using the McICA approach and PSRad (*Pincus and Stevens*, 2013). The RCE setup incorporates a spatially homogeneous diurnal cycle of insolation with a mean value of $340.3\,\mathrm{W\,m^{-2}}$, no rotation of the planet and homogeneous conditions at the surface. The RCE setup is similar to the one described in more detail in *Popke et al.* (2013) and *Becker and Stevens* (2014), the only fundamental difference is that the RCE model is not coupled to a mixed layer ocean. Instead, we use globally uniform prescribed SSTs.

To understand how the SST dependence of large-scale convective self-aggregation is controlled by the convective parameterization, we have performed some sensitivity studies. We use four different representations of convection, Nordeng, HalfEntrN, NoEntrN and NoCnvPm (defined in Chapter 2.2.1), and we alter the SST at 5 K intervals in the range from 285 K to 305 K for all convective parameterization setups. Some additional simulations have been performed, including simulations where clouds are made invisible to radiation, similar to the Clouds On/Off Klima Intercomparison Experiments (COOKIE, *Stevens et al.*, 2012), but no surprise emerged. These simulations are only discussed in so far as they help understand one or the other aspect of the base simulations.

All simulations start from a homogeneous dry initial state and were run for 5 simulation

years. In all simulations equilibrium is reached after 1 year at the latest, so the last 4 years are analyzed. A check confirmed that results are statistically significant when looking at a 4-year average.

2.3. Quantifying convective self-aggregation with subsidence fraction

Because convective aggregation has a strong impact on many different climate parameters, the degree of convective aggregation can be quantified in various ways. For example, convective aggregation can be quantified with the domain mean or spatial variance of outgoing longwave radiation, water vapor path, or surface fluxes (*Bretherton et al.*, 2005; *Tobin et al.*, 2012). However, these quantities share the problem that they depend on SST, which would greatly complicate their application to our results. Parameters that do not depend on SST are, for example, column relative humidity or saturation fraction, defined as column water vapor path divided by saturation water vapor path (*Wing and Cronin*, 2016). Here, we quantify convective aggregation with subsidence fraction (*Coppin and Bony*, 2015; *Bony et al.*, 2016), another parameter that does not depend on SST. Subsidence fraction is estimated as the area where the mass-weighted vertically integrated (1000 - 200 hPa) and daily averaged vertical velocity is directed downward.

Figure 2.1 demonstrates that the variations of convective self-aggregation with SST strongly depend on the representation of convection. Convective self-aggregation is independent of SST in the two extreme convection scheme setups, with NoCnvPm and NoEntrN. With the two less extreme setups, Nordeng and HalfEntrN, we observe a nonmonotonic dependence of convective self-aggregation on SST. With Nordeng, self-aggregation decreases with SST for SSTs below 295 K, while above 295 K, self-aggregation increases with SST. With HalfEntrN, self-aggregation only increases with SST if SST is above 300 K. Mechanisms that can explain why convective self-aggregation depends on SST nonmonotonically and the reasons why the response differs with Nordeng and HalfEntrN are discussed in Chapters 2.5.2 and 2.5.3.

Independent of SST, convection is always most aggregated with NoCnvPm, Nordeng is in most of the simulations more aggregated than HalfEntrN and NoEntrN, and HalfEntrN is slightly more aggregated than NoEntrN at 285 K and 305 K, but less aggregated in between. Hence, with a few exceptions, higher entrainment rates can be associated with more convective self-aggregation, similar to what was found by *Arnold and Randall* (2015). The following section analyzes why the degree of convective self-aggregation depends on the convective parameterization, and in particular on the entrainment parameter, restricting the analysis to the simulations with 305 K SST.

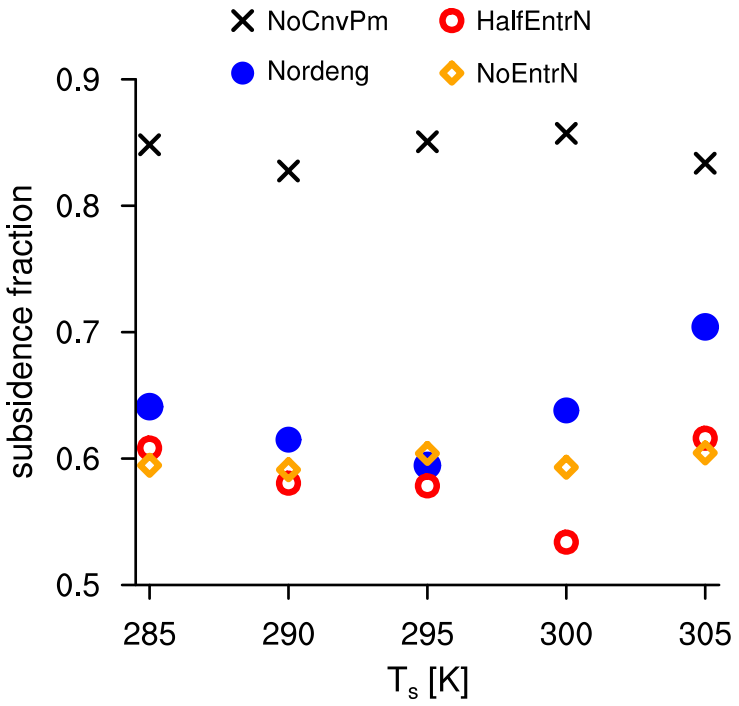

Figure 2.1.: Area fraction where mass-weighted vertically integrated (1000 - 200 hPa) vertical velocity is directed downward, with different convective parameterizations and SSTs, averaged over all daily means in the analysis period. For all simulations, the range between the 25th and 75th percentile of daily-mean subsidence fraction is on the order of the respective symbol sizes. The standard error is estimated to be smaller than 0.002 (based on a 10 day autocorrelation time scale for the time-series of subsidence fraction).

2.4. How does the convective parameterization affect convective self-aggregation?

2.4.1. Horizontal structure

Snapshots of precipitation and 10 m wind field, presented for the four different representations of convection in Figure 2.2, illustrate that in the global RCE model setup, convection aggregates on very large scales, with the largest convective systems being of the size of a continent. The snapshots also show that the simulations which aggregate more, like NoCnvPm but also Nordeng, have more clearly separated regions of subsidence and upward motion, larger individual subsidence regions, higher 10 m wind speeds, and more intense precipitation. In NoCnvPm, both the global mean 10 m wind speed and the difference between mean upward and mean downward velocity are almost three times larger than in NoEntrN (Table 2.1), confirming the impression of a much stronger overturning circulation in NoCnvPm than in NoEntrN. The increase of subsidence fraction is associated with a more pronounced increase of mean upward velocities in the convectively active areas than

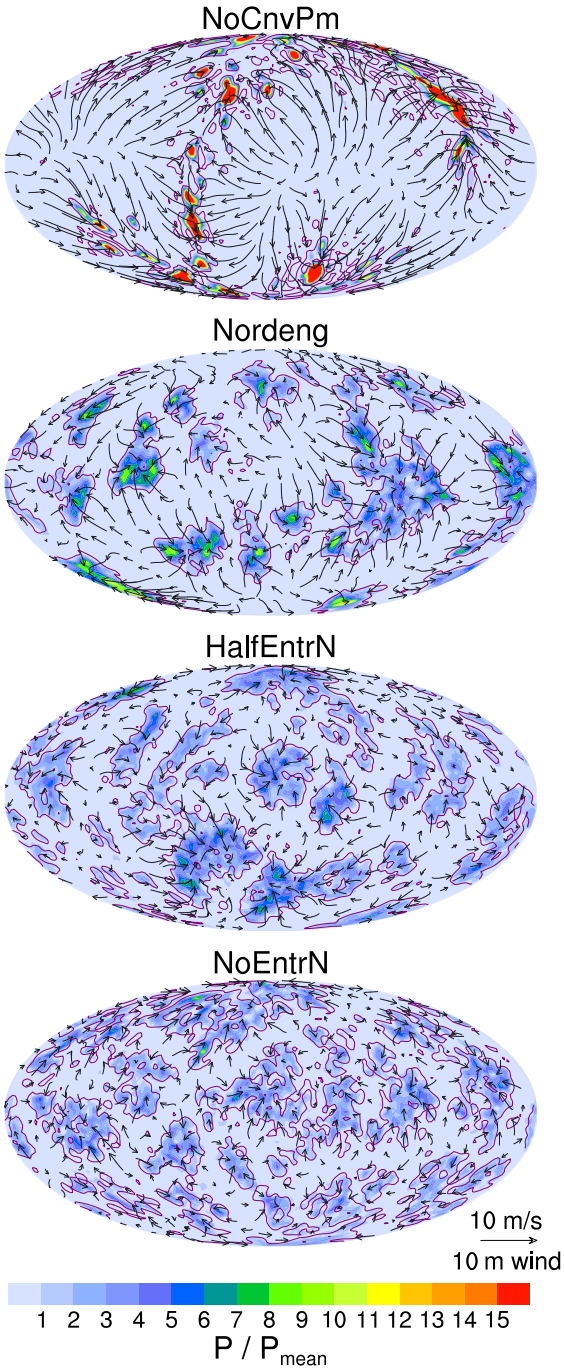

Figure 2.2.: Random snapshots of precipitation relative to the global mean precipitation and 10 m wind field with different convective parameterizations at 305 K SST, averaged over 1 day. Purple contour lines distinguish subsidence and upward motion areas, indicating where daily averaged mass-weighted vertically integrated vertical velocities are zero.

of mean downward velocities in the subsidence region (Table 2.1).

2.4.2. Vertical structure

Because in our simulations convection aggregates in response to changes in the model physics, the results are not necessarily the same as in a transient run with constant model physics but varying aggregation. For a given degree of aggregation, we can expect that with a larger entrainment rate, more updrafts detrain in the lower troposphere, moistening the lower troposphere and leading to more low clouds as compared to high clouds. For a given degree of aggregation, we can also expect the troposphere to be less stable with a larger entrainment rate because updrafts are more diluted, and therefore the concept of moist adiabatic ascent is less accurate. Those expectations are consistent with findings of *Tomassini et al.* (2015), who changed the entrainment rate in a coupled ocean-atmosphere model, in which convective aggregation plays less of a role. The question we answer in this subsection is whether those expectations are also fulfilled in the presence of convective aggregation.

Both in convection-permitting models (e. g., *Bretherton et al.*, 2005) and in observations (*Tobin et al.*, 2012), convective aggregation is accompanied by mid-tropospheric drying. However, in our simulations global mean free tropospheric relative humidity does not depend much on the degree of self-aggregation (Figure 2.3). Even though the subsidence region ex-

Table 2.1.: 10 m wind speed (v_{10}), mean upward velocity (ω_{up}), mean downward velocity (ω_{down}), and subsidence fraction (area fraction in which the daily averaged mass-weighted vertical integral from 200 to 1000 hPa of vertical velocity is directed downward, SF) with different convective parameterizations at 305 K SST, averaged over the analysis period.

Simulation	v_{10} [$m\,s^{-1}$]	ω_{up} [$hPa\,d^{-1}$]	ω_{down} [$hPa\,d^{-1}$]	SF [%]
NoCnvPm	5.5	-124	25	83
Nordeng	3.0	-53	22	70
HalfEntrN	2.2	-36	22	62
NoEntrN	2.0	-34	22	60

pands when aggregating and has a dry free troposphere (Figure 2.4), the larger subsidence region in more aggregated states does not project much on the mean state because the region with ascending air masses is moister in more aggregated states (Figure 2.4), almost balancing the drying on the global mean. The moistening of the region with ascending air masses does not only result from aggregation itself, including more vertical moisture advection by the resolved flow because of higher vertical velocities, but also results from changing the convective parameterization. Higher entrainment rates lead to an increase of relative humidity in the region with ascending air masses because high entrainment causes more organized detrainment at lower levels, which moistens the updraft's surrounding. In addition, updrafts with high entrainment rates concentrate in very moist columns wherein mixing does not strongly diminish updraft buoyancy. The moistening of the region with ascending air masses also leads to a higher precipitation efficiency and to less evaporating rain, decreasing water vapor residence time t_v, defined as the ratio of water vapor path to precipitation rate (Table 2.2). Had the circulation not changed, a higher entrainment rate would cause the opposite signal, an increase of t_v due to more mixing. So large-scale convective self-aggregation dominates the large-scale statistics, partly masking the direct but local effects from changing the entrainment rate that one might have expected had the circulation not changed.

Table 2.2.: Precipitation (P), water vapor residence time (ratio of water vapor path to precipitation rate, t_v), radiative imbalance of the atmosphere (R_{atm}) and at the top-of-atmosphere (R_{TOA}), top-of-atmosphere outgoing longwave radiation (OLR), top-of-atmosphere absorbed solar radiation (ASR) and virtual potential temperature difference between 200 and 1000 hPa ($\Theta_{v_{200}} - \Theta_{v_{1000}}$) with different convective parameterizations at 305 K SST, averaged over the analysis period.

Simulation	P [$mm\,d^{-1}$]	t_v [d]	R_{atm} [$W\,m^{-2}$]	R_{TOA} [$W\,m^{-2}$]	OLR [$W\,m^{-2}$]	ASR [$W\,m^{-2}$]	$\Theta_{v_{200}} - \Theta_{v_{1000}}$ [K]
NoCnvPm	5.2	9.8	-174	-72.6	292	220	57.5
Nordeng	4.4	11.1	-148	-8.5	283	275	54.6
HalfEntrN	4.1	10.9	-140	4.4	286	290	51.2
NoEntrN	3.7	12.7	-126	13.4	267	281	55.0

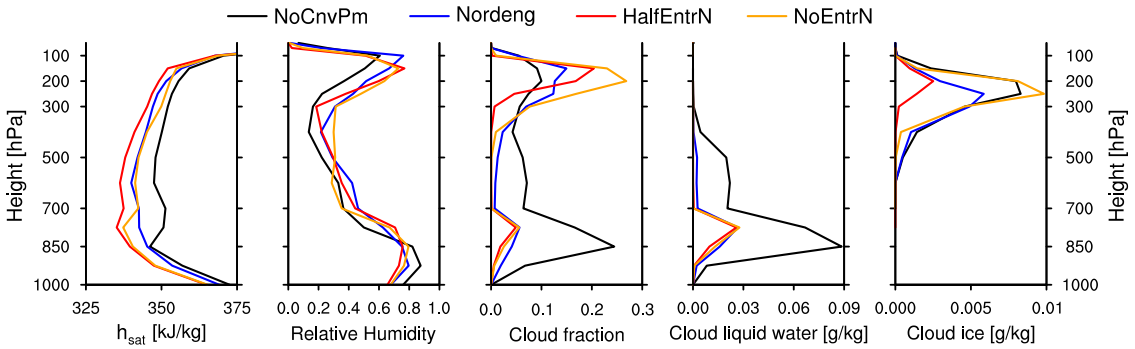

Figure 2.3.: Profiles of atmospheric state variables with different convective parameterizations at 305 K SST, averaged over the analysis period and plotted as a function of pressure level. h_{sat} is the saturated moist static energy.

Tropospheric stability increases with convective aggregation ($\Theta_{\mathrm{v}_{200}} - \Theta_{\mathrm{v}_{1000}}$ in Table 2.2) because convection occurs at a much warmer effective temperature, as explained in the next subsection. However, a consequence of changing the convective parameterization shows up in NoEntrN, where stability is high though convection is quite unaggregated. In the absence of entrainment, updrafts are fixed to the moist adiabat, stabilizing the temperature profile, in line with *Tomassini et al.* (2015). Hence, small entrainment rates keep the updraft close to the moist adiabat, which increases stability, but small entrainment rates also cause convection to be less aggregated, which reduces stability. Overall, convective aggregation dominates, masking the direct effect from changing the entrainment rate that one might have expected had the circulation not changed.

In NoCnvPm, vertical moisture transport through convection is limited, leading to a high cloud fraction at the top of the boundary layer, whereas in NoEntrN, the lack of entrainment induces a large cloud fraction at the tropopause (Figure 2.3) because the updrafts do not mix with their environment and instead deposit all their moisture at the tropopause. Observations also show a tendency of more high clouds per unit low cloud in less aggregated environments (*Stein et al.*, 2017). A study of *Bony et al.* (2016) also indicated that in less aggregated environments, anvil cloud fraction increases because stability close to the tropopause decreases, which implies that more clear-sky mass divergence is required to balance the vertical gradient in radiative cooling, leading to more extensive anvil clouds. This stability effect persists in our simulations, as the profiles of saturated moist static energy in Figure 2.3 illustrate. Thus, with respect to the vertical profile of cloud fraction, convective aggregation has the potential to amplify the direct effect from changing the entrainment rate.

Based on a more bottom-heavy profile of cloudiness in simulations with higher entrainment rates, we can expect a larger top-of-atmosphere (TOA) energy budget deficit. Convective aggregation perturbs the system in the same direction, also leading to a larger

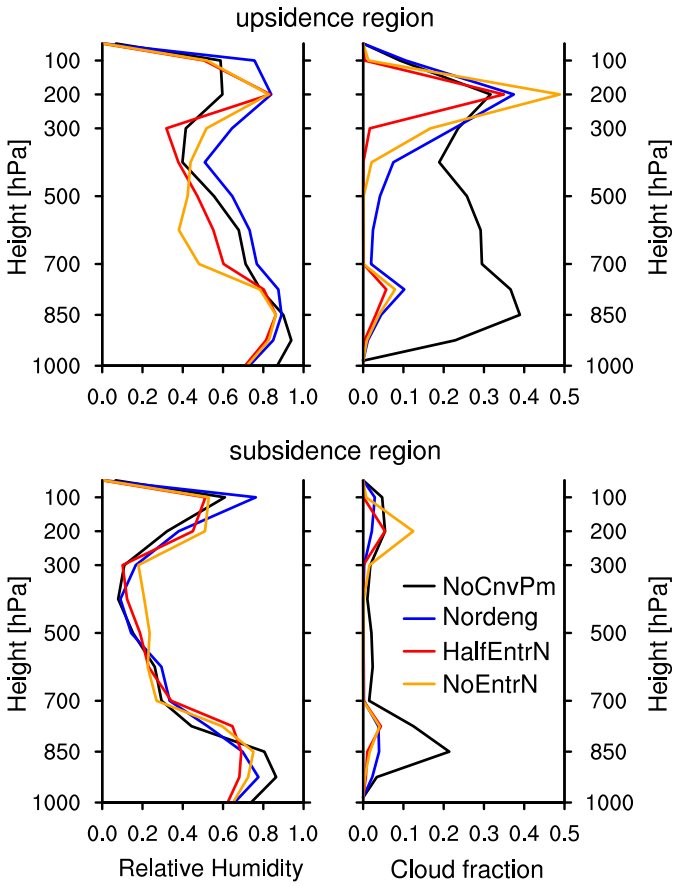

Figure 2.4.: As Figure 2.3, but focusing on relative humidity and cloud fraction, and separating where daily averaged mass-weighted vertically integrated (1000 - 200 hPa) vertical velocity is directed downward and upward.

TOA energy budget deficit in more aggregated situations, both in observations (*Tobin et al.*, 2012) and models (*Hohenegger and Stevens*, 2016). In our simulations, NoEntrN has indeed a 13 $\mathrm{W\,m^{-2}}$ TOA energy budget surplus, while NoCnvPm has a 73 $\mathrm{W\,m^{-2}}$ deficit (Table 2.2). In Nordeng, HalfEntrN, and NoEntrN, the changes of the TOA energy budget are primarily induced by changes in net atmospheric longwave cooling, which is in line with observations (*Tobin et al.*, 2012). Larger subsidence regions associated with more convective self-aggregation cool more efficiently, inducing an increase of atmospheric longwave cooling, for example, by 23 $\mathrm{W\,m^{-2}}$ in Nordeng compared to NoEntrN. Convective heating compensates, inducing rare but more intense precipitation which overcompensates on the global average the more frequent but less intense precipitation in less aggregated conditions (Table 2.2). Not in line with observations is that the negative TOA energy budget in NoCnvPm is caused by changes in absorbed solar radiation (ASR). In NoCnvPm, ASR is much smaller than with an activated convective parameterization because in the absence of parameterized shallow convection, a strong cloud-topped inversion at the top of

the boundary layer develops (Figure 2.3). These low-level clouds have a strong impact on the radiation budget because they are prevalent in the subsidence region (Figure 2.4). In summary, the convective parameterization affects the vertical profile of moisture, temperature and clouds, as well as the TOA energy budget directly. Nonetheless, the large-scale statistics are dominated by convective aggregation, either masking or amplifying the direct effects associated with the convective parameterization.

2.4.3. Moist static energy distribution

To understand which processes govern the interaction of convection and large-scale circulation and are thus responsible for convective self-aggregation, we analyze the spatial distribution of moist static energy. Moist static energy is an invariant for moist adiabatic processes and is defined as

$$h = c_p T + gz + L_\mathrm{v} q, \tag{2.2}$$

where c_p is the isobaric specific heat capacity, T is temperature, g is gravity, z is geopotential height, L_v is the enthalpy of vaporization, and q is specific humidity. The sum of the first two terms is also known as the dry static energy (s). Unlike other studies (*Wing and Emanuel*, 2014; *Arnold and Randall*, 2015), we neglect the contribution of ice to moist static energy for reasons of simplicity and because the influence of frozen particles on the moist static energy budget is very small in the RCE setup. It also proves useful to analyze the mass-weighted vertical integral of h,

$$\langle h \rangle = \frac{1}{p_\mathrm{s} - p_\mathrm{t}} \int_{p_\mathrm{s}}^{p_\mathrm{t}} h \, \mathrm{d}p, \tag{2.3}$$

with $p_\mathrm{s} = 1000\,\mathrm{hPa}$ and $p_\mathrm{t} = 50\,\mathrm{hPa}$. The column longwave and shortwave net radiative fluxes in the atmosphere ($\mathrm{R_{atm,LW}}$ and $\mathrm{R_{atm,SW}}$), the latent and sensible heat release from the surface (LH and SH) and large-scale horizontal convergence of the flux of $\langle h \rangle$ ($\nabla_\mathrm{h} \cdot \langle \vec{u} h \rangle$) are the only terms that can alter $\langle h \rangle$:

$$\frac{\partial \langle h \rangle}{\partial t} = \mathrm{R_{atm,LW}} + \mathrm{R_{atm,SW}} + \mathrm{LH} + \mathrm{SH} - \nabla_\mathrm{h} \cdot \langle \vec{u} h \rangle \tag{2.4}$$

In the RCE setup, perturbations in temperature, or density, are damped and radiated away by gravity waves. These weak temperature gradient (WTG) conditions (*Sobel and Bretherton*, 2000) imply that horizontal anomalies in h are essentially water vapor anomalies. For example, with Nordeng at 305 K, the standard deviation of $\langle h \rangle$, $\sigma_{\langle h \rangle}$, is 19 times larger than the standard deviation of $\langle s \rangle$, $\sigma_{\langle s \rangle}$. In all of the simulations, the distributions of $\langle h \rangle$ are very closely coupled to precipitation (Figure 2.5a). Upward motion (dashed line in Figure 2.5b) and precipitation only occur if $\langle h \rangle$ exceeds a certain value and precipitation

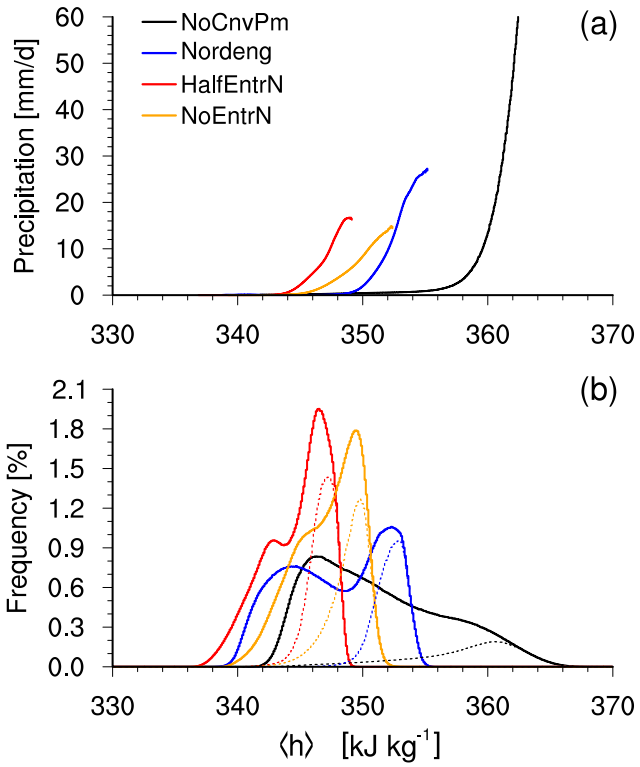

Figure 2.5.: (a) Precipitation versus daily mean column-integrated h, at 0.05 kJ kg^{-1} intervals, and (b) histograms of daily mean column-integrated h (solid line: global; dashed: only in the region where column-integrated vertical velocity is directed upward), with a bin size of 0.1 kJ kg^{-1}. Presented are simulations with different convective parameterizations at 305 K SST.

intensifies depending on how much this value is exceeded.

The coupling of precipitation to $\langle h \rangle$ is weakest in NoEntrN, resulting in a more gradual increase of precipitation with increasing $\langle h \rangle$ (Figure 2.5a). For example, the correlation coefficient of $\langle h \rangle$ and precipitation is 0.68 with Nordeng, 0.69 with HalfEntrN and 0.63 with NoEntrN. With NoEntrN the correlation coefficient is smaller than with Nordeng and HalfEntrN because the deactivation of entrainment decouples the convective updraft from its updraft environment, while in case of a high entrainment rate, precipitating convection can only occur in regions where the free troposphere is moist because otherwise entrainment of dry air would decrease updraft buoyancy too much (*Tompkins and Semie*, 2017). Likewise, the detrainment also moistens the environmental air. The arguments hold only qualitatively for NoCnvPm (correlation coefficient of 0.43), as quantitatively the variability of precipitation across regions of high $\langle h \rangle$ weakens the relationship. Because of the simple budget equation and the close relation to precipitating convection, $\langle h \rangle$ is used in the following sections as an analysis tool to better understand convective self-aggregation.

With convective parameterizations that make it hard to trigger and maintain convection, mostly with NoCnvPm but also with Nordeng, $\langle h \rangle$ needs to be closer to $\langle h_{\mathrm{sat}} \rangle$,

so stronger $\langle h \rangle$ perturbations are necessary before precipitating convection occurs (Figure 2.5a). In case of scattered convection, detrainment cannot simply drive convectively active columns towards saturation because large-scale mixing is too strong. Hence, a strong overturning circulation associated with a high degree of convective self-aggregation is needed to efficiently transport enough water vapor into the convectively active regions and to increase updraft buoyancy by a sufficient amount to successfully produce precipitating convection. Thus, σ_h increases in response to convective self-aggregation, also because the subsidence fraction increase leads to a shift of weight towards low h (Figure 2.5b). By stabilizing the subsidence region against convection, a large σ_h favors self-aggregation. Convective self-aggregation is accompanied by a rise of the convecting temperature (*Held et al.*, 1993; *Bretherton et al.*, 2005), and the static stability of the troposphere increases in the whole domain, assuming WTG conditions. Thus, CAPE reduces and larger h perturbations are necessary in the boundary layer for the onset of convection, in agreement with boundary-layer quasi-equilibrium theory (*Raymond*, 1997). This makes it more unlikely that sufficient h perturbations are created in the absence of a strong large-scale circulation. Cause and effect are hard to disentangle because large h perturbations are only possible if convection is aggregated, and convective self-aggregation causes an increase in σ_h.

The increase of static stability with aggregation affects the distribution of $\langle h \rangle$, shifting the whole distribution toward higher values because of enhanced upper-tropospheric temperatures. The higher values of $\langle h \rangle$ in NoEntrN compared to HalfEntrN are not associated with self-aggregation, but with convection strictly following the moist adiabat because updrafts do not lose any buoyancy through entrainment. To conclude, the global reorganization of convection dominates the statistics of the RCE stationary state, partly masking the subtle differences in how convection couples to that state induced by the differences in the convective parameterization.

2.5. How does the convective parameterization affect the SST dependence of convective self-aggregation?

In this section, we analyze why convective self-aggregation depends nonmonotonically on SST when using Nordeng, and why we find a different SST dependence with NoCnvPm, HalfEntrN and NoEntrN. Both with Nordeng and HalfEntrN, convective self-aggregation depends on SST in a similar way (Figure 2.1), suggesting that mechanisms that maintain self-aggregation are similar. The snapshots in Figure 2.6 illustrate that with Nordeng, convection aggregates at high SSTs in blobs, with diameters of about 5 000 km, while it aggregates at low SSTs in arcs, with scales of up to 20 000 km in length. The arcs move rapidly toward the subsidence region with the strongest overturning circulation (Figure 2.6). At low SSTs, convective structures often travel to the other side of the planet within a week, while at high SSTs, they remain mostly at the same location in the

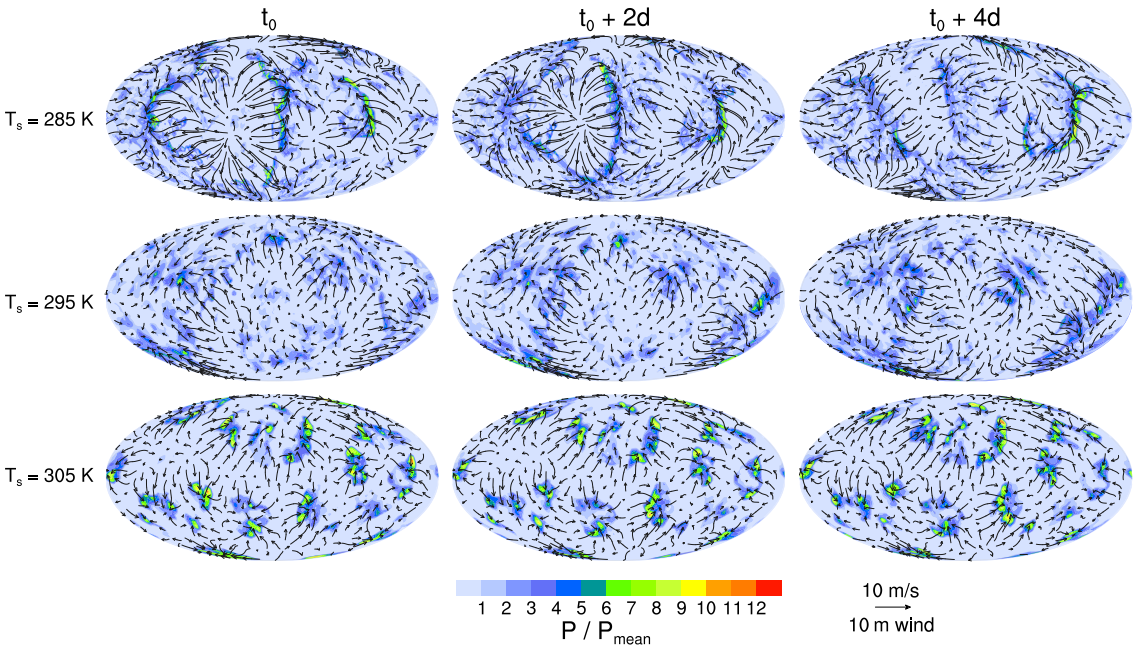

Figure 2.6.: Random snapshots of precipitation relative to the global mean precipitation and 10 m wind field with Nordeng at three different SSTs, averaged over 1 day, showing also the consecutive snapshot 2 days later and 4 days later, respectively.

same time frame (Figure 2.6). This emphasizes the need to use daily means or shorter time scales when analyzing subsidence fraction. The enhanced cluster movement is also apparent in the global mean 10 m wind speed, which increases with decreasing SST, from 2.3 $\mathrm{m\,s^{-1}}$ at 300 K to 3.8 $\mathrm{m\,s^{-1}}$ at 285 K, also hinting at a stronger overturning circulation at lower SSTs. The slight recovery of surface winds at 305 K (2.9 $\mathrm{m\,s^{-1}}$) associated with strong self-aggregation does not change the overall picture.

2.5.1. Moist static energy variance budget

As the analysis in Chapter 2.4.3 has shown, high values of $\sigma_{\langle h \rangle}$ are associated with a high degree of convective self-aggregation. In this subsection, the spatial variance budget of $\langle h \rangle$ is analyzed with the goal to understand how the convective parameterization determines which physical processes are related to convective self-aggregation, and how these processes depend on SST. Following *Wing and Emanuel* (2014), we analyze factors influencing convective self-aggregation with the aid of the spatial moist static energy variance budget:

$$\frac{1}{2}\frac{\partial \langle h \rangle'^2}{\partial t} = \langle h \rangle' \mathrm{R_{atm,LW}}' + \langle h \rangle' \mathrm{R_{atm,SW}}' + \langle h \rangle' \mathrm{LH}' + \langle h \rangle' \mathrm{SH}' - \langle h \rangle' \nabla_\mathrm{h} \cdot \langle \vec{u} h \rangle. \tag{2.5}$$

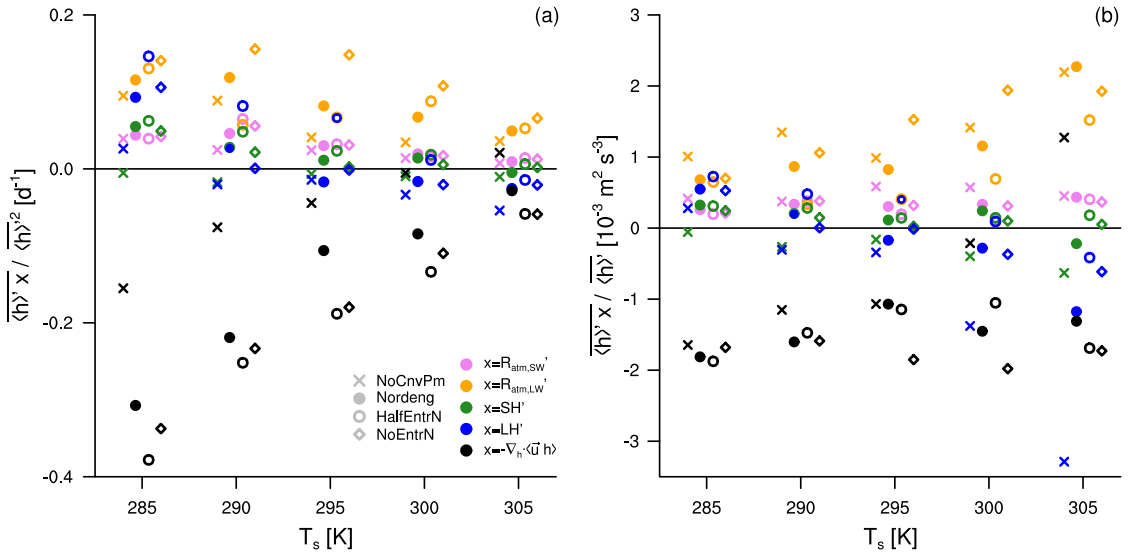

Figure 2.7.: Covariance of column-integrated moist static energy $\langle h \rangle$ and different sources of $\langle h \rangle$, averaged over the analysis period and (a) scaled with the global average of $\langle h \rangle$ variance, or (b) scaled with the global average of $\langle h \rangle$ standard deviation. The large-scale horizontal convergence of the flux of $\langle h \rangle$ is the residual.

Each term contains the covariance between $\langle h \rangle$ anomalies and $\langle h \rangle$ sources, or $\langle h \rangle$ convergence, respectively. Averaging over time and space and normalizing each term with $\overline{\langle h \rangle'^2}$ yields the contribution of the different diabatic source terms to the growth rate of $\langle h \rangle$ variance, while normalizing with $\overline{\langle h \rangle'}$ yields the contribution to $\langle h \rangle$ standard deviation. To emphasize that, when identifying the governing mechanisms involved in self-aggregation, the absolute values are less important than the fractional contribution of each term relative to the other source terms, Figure 2.7 shows the contribution of each term to both $\overline{\langle h \rangle'}$ variance and to $\langle h \rangle$ standard deviation. Many studies have shown that the mechanisms that lead to self-aggregation and that sustain self-aggregation can differ substantially (e. g., *Muller and Held*, 2012). Here, we focus on the mechanisms that sustain convective self-aggregation.

Convection-permitting studies show consistently that, given some initial self-aggregation, self-aggregation is maintained by cloud, water vapor and radiation feedbacks because dry regions expand and confine convection into moister regions (*Bretherton et al.*, 2005; *Muller and Held*, 2012; *Jeevanjee and Romps*, 2013; *Wing and Emanuel*, 2014; *Muller and Bony*, 2015; *Bretherton and Khairoutdinov*, 2015; *Wing and Cronin*, 2016; *Holloway and Woolnough*, 2016; literature overview by *Mapes*, 2016). In accordance with this, Figure 2.7 shows that in all of the simulations, except with HalfEntrN below 295 K, the longwave net atmospheric flux is the dominant source of $\langle h \rangle$ variance, maintaining convective self-aggregation in the equilibrium state. The reason is that in convectively active regions, clouds and enhanced water vapor concentrations increase the effective longwave emission

height, thus reducing the atmosphere's longwave cooling in regions of high $\langle h \rangle$, while dry subsidence regions have low effective emission heights, thus accelerating the atmosphere's cooling in regions of low $\langle h \rangle$. In NoEntrN, more condensate is detrained at higher levels. This leads to even more high clouds in the convectively active region, amplifying the cloud-radiative effect.

The net shortwave irradiance is an additional source of $\langle h \rangle$ variance in all simulations because clear-sky atmospheric shortwave absorption increases with column water vapor, but the magnitude of this effect is much smaller than the longwave radiative feedback. Surface fluxes and especially latent heat release are sources of $\langle h \rangle$ variance at low SSTs. This turns out to be very important for convective self-aggregation at low SSTs, as discussed in more detail in Chapter 2.5.2. The large-scale horizontal convergence of the flux of $\langle h \rangle$, which is calculated as residual from the budget, is a sink of $\langle h \rangle$ variance in almost all of the simulations, which means that the circulation is thermally direct, as it transfers moist static energy from high-h regions to low-h regions. However, the fractional contribution of $\langle h \rangle$ convergence to the $\langle h \rangle$ variance budget decreases with increasing SST (Figure 2.7).

2.5.2. Which mechanisms reinforce convective self-aggregation at low SSTs?

An increase of convective self-aggregation with decreasing SST has so far only been found by *Coppin and Bony* (2015) with the IPSL model in RCE mode. They explain the increase of convective self-aggregation at SSTs below 300 K with a more effective cooling from low clouds in the subsidence region, leading both to the formation of radiatively driven cold pools, and to a shallow overturning circulation. In ECHAM6-RCE, convective self-aggregation increases with decreasing SST at SSTs below 295 K with Nordeng, and below 300 K with HalfEntrN (Figure 2.1), while NoEntrN and NoCnvPm do not show any SST dependence.

Surface fluxes have the potential to be very important for convective self-aggregation because anomalies in sensible or latent heat flux are sources of h perturbations in the boundary layer. Properties which can influence surface fluxes are SST, wind speed, relative humidity, and stability at the lowest model level. At low SSTs, the latent heat flux tends to be stronger in regions of large $\langle h \rangle$ and is a source of $\langle h \rangle$ variance (Figure 2.7). This is counter-intuitive because, all else being equal, high h perturbations in the boundary layer imply less latent heat flux because h perturbations mostly reflect humidity perturbations. However, the lower the SST, the less do perturbations in latent and sensible heat flux depend on relative humidity and stability anomalies, but are dominated by the wind speed (Figure 2.8). The wind speed itself also shows an SST dependence. With Nordeng, at high SSTs, wind speeds maximize close to the median of $\langle h \rangle$ and differ only by about $1\,\mathrm{m\,s^{-1}}$, while at low SSTs, wind speeds in high $\langle h \rangle$ regions are on average more than $3\,\mathrm{m\,s^{-1}}$ higher than winds in low $\langle h \rangle$ regions (Figure 2.8a). Thus, sensible and especially latent

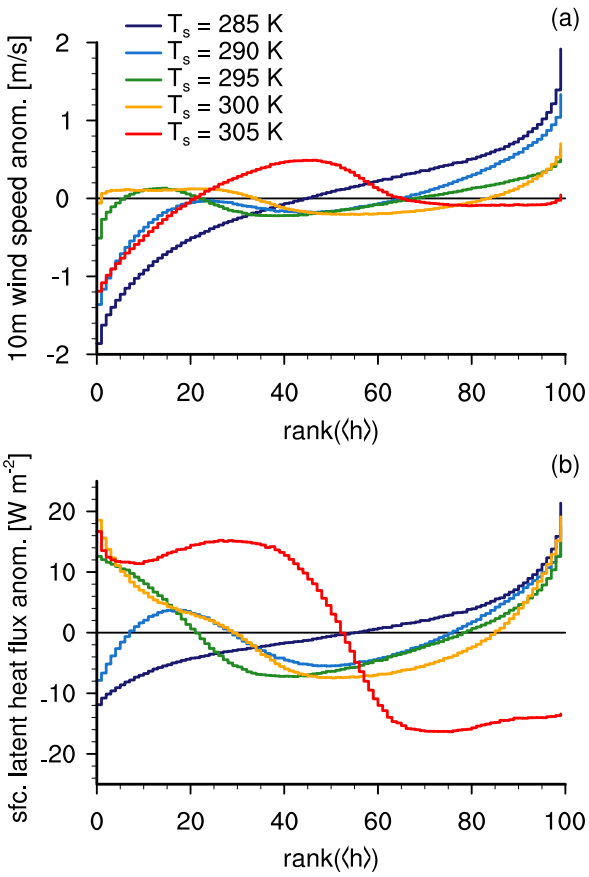

Figure 2.8.: (a) Anomaly of 10 m wind speed and (b) surface latent heat flux, sorted by column-integrated moist static energy, for five different SSTs with Nordeng, using daily mean values averaged over the analysis period.

heat fluxes are important for convective self-aggregation at low SSTs due to a stronger coupling of surface fluxes to the wind speed and due to a changing wind pattern.

The local moisture supply through surface evaporation, which becomes more important at low SSTs, can explain the changing wind pattern. As Figure 2.6 demonstrates, at low SSTs convection favors the edges of the largest subsidence regions. At the edges, the low-level flow converges, creating more favorable conditions for convective activity, in particular because the high surface wind speeds induce high surface heat fluxes (WISHE feedback). The size of large subsidence regions decreases with time because convective structures propagate toward the center of the subsidence region, always seeking the strongest surface fluxes, until the edges of another subsidence region are more favorable for convection. This is the reason for the fast movement of the convective structures at low SSTs. Because of these dynamics, it is not surprising that the ratio of the globally averaged absolute value of vertically integrated moisture convergence, $|\nabla_\mathrm{h} \cdot \langle \vec{u}q \rangle|$, and of surface moisture flux, E, shows an SST dependence. The resulting dimensionless number γ, which describes

Table 2.3.: Ratio of the daily-averaged absolute value of vertically integrated moisture convergence and of surface moisture flux ($|\nabla_\mathrm{h} \cdot \langle \vec{u}q \rangle| \,/\, (E\, g/p_\mathrm{s})$), column water vapor ($\langle q \rangle$), precipitation ($P$), water vapor residence time (t_v), vertical velocity in the subsidence region (ω_sub), and virtual potential temperature difference between 300 and 1000 hPa ($\Theta_{\mathrm{v}_{300}} - \Theta_{\mathrm{v}_{1000}}$) with different SSTs in Nordeng, averaged over the analysis period.

Simulation	$\lvert\nabla_\mathrm{h} \cdot \langle \vec{u}q \rangle\rvert \,/\, (E\, g/p_\mathrm{s})$	$\langle q \rangle$ [kg m^{-2}]	P [mm d^{-1}]	t_v [d]	ω_sub [hPa d^{-1}]	$\Theta_{\mathrm{v}_{300}} - \Theta_{\mathrm{v}_{1000}}$ [K]
285 K	1.20	8.6	2.3	3.8	36.8	15.0
290 K	1.26	14.0	2.8	5.1	30.7	19.4
295 K	1.56	21.7	3.1	7.0	25.8	24.9
300 K	2.38	31.1	3.4	9.1	23.8	30.6
305 K	3.17	49.0	4.4	11.1	22.2	46.2

how much water vapor in a column stems from horizontal convergence relative to surface evaporation, is close to 1 at low SSTs, and shows an increase of about $4.7\,\%\,\mathrm{K}^{-1}$, although less pronounced at low SSTs (Table 2.3).

Using thermodynamic reasoning, we can understand why, at low SSTs, surface moisture fluxes are relatively more important than horizontal moisture convergence for the onset of convection. In equilibrium state, E is equal to precipitation P, and $|\nabla_\mathrm{h} \cdot \langle \vec{u}q \rangle|$ can be assumed to scale with the product of column water vapor $\langle q \rangle$ and the average vertical velocity in the subsidence region, ω_sub, from which the strength of the large-scale overturning circulation can be inferred. The ratio of $\langle q \rangle$ and P defines the water vapor residence time t_v. So in total, γ can be constrained by

$$\gamma \sim \frac{|\nabla_\mathrm{h} \cdot \langle \vec{u}q \rangle|}{E} \sim \frac{\langle q \rangle}{P}\, \omega_\mathrm{sub} \sim t_\mathrm{v}\, \omega_\mathrm{sub}. \tag{2.6}$$

For a given strength of circulation, t_v measures how local the precipitation is: a shorter residence time implies that precipitation forms near where it evaporates, and suggests that latent heat fluxes are more important for precipitation than they would be for the same circulation but a longer residence time. With decreasing SST, t_v strongly decreases because $\langle q \rangle$ changes more with SST than P does. In Nordeng, $\langle q \rangle$ increases with $9.1\,\%\,\mathrm{K}^{-1}$ (Table 2.3), and thus is in the same range as in other studies (*O'Gorman and Muller*, 2010; *Muller et al.*, 2011). Though there is a super Clausius-Clapeyron (CC) scaling of $\langle q \rangle$, precipitation depends less on temperature than CC (*Held and Soden*, 2006). In Nordeng, precipitation increases with $3.2\,\%\,\mathrm{K}^{-1}$ (Table 2.3), which is, compared to the hydrological sensitivity parameter in other studies (*Fläschner et al.*, 2016), a rather large rate of increase. The differences in SST dependence of $\langle q \rangle$ and P result in an increase of t_v by $5.7\,\%\,\mathrm{K}^{-1}$ (Table 2.3). Hence, in the absence of a changing large-scale circulation, precipitating convection is more tied to local surface moisture fluxes at low SSTs.

The average vertical velocity in the subsidence region, ω_sub, decreases in Nordeng by about $-3.5\,\%\,\mathrm{K}^{-1}$ at low SSTs and by about $-1.5\,\%\,\mathrm{K}^{-1}$ at high SSTs (Table 2.3). The

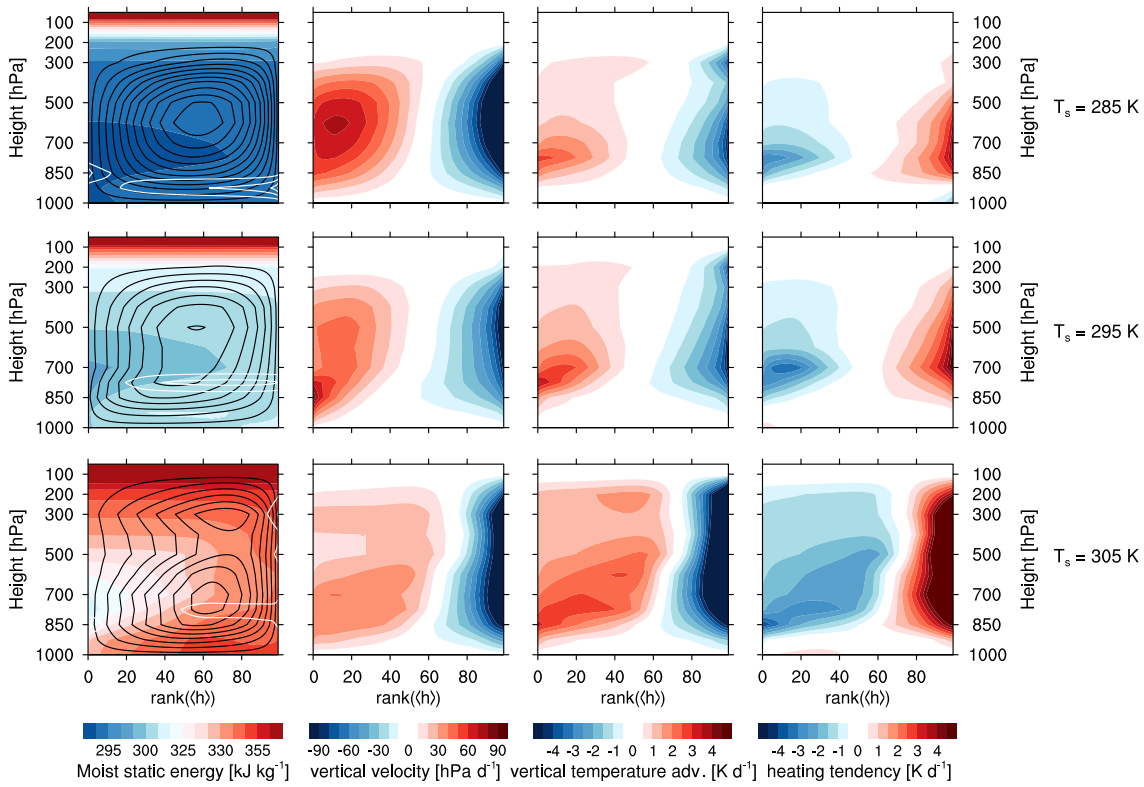

Figure 2.9.: Moist static energy, contours of streamfunction (in black, counter-clockwise, every $0.02\,\mathrm{kg\,m^{-2}\,s^{-1}}$) and contours of cloud water content (liquid + ice, in white, every $0.03\,\mathrm{g\,kg^{-1}}$) [1st column], vertical velocity [2nd column], warming associated with vertical motion [3rd column], and diabatic heating tendency [4th column], plotted as a function of pressure level and column-integrated moist static energy, for three different SSTs with Nordeng, using daily mean values averaged over the analysis period.

subsidence velocity is thermodynamically constrained by the ratio of diabatic cooling Q and static stability. The diabatic cooling, which is primarily longwave cooling, does not increase at low SSTs, if anything, it decreases (Figure 2.9). Thus, the increase in subsidence velocity (Figure 2.9) must be caused by a strong decrease in static stability, which overcompensates the decrease in Q. Considering the whole troposphere, in radiative-convective equilibrium Q is proportional to P and stability can be approximated from the virtual potential temperature difference between 1000 and 300 hPa:

$$\omega_{\mathrm{sub}} \sim \frac{Q}{\partial\Theta_{\mathrm{v}}/\partial p} \sim \frac{P}{\Theta_{\mathrm{v}_{300}} - \Theta_{\mathrm{v}_{1000}}}. \tag{2.7}$$

When constraining subsidence velocity with this approximation, a decrease rate of $-2.2\,\%\,\mathrm{K^{-1}}$ results (Table 2.3). In total, based on Equations (2.6) and (2.7), γ is thermodynamically constrained to increase with $3.4\,\%\,\mathrm{K^{-1}}$, which is a bit less than the actual rate of increase, $4.7\,\%\,\mathrm{K^{-1}}$. The difference between the thermodynamically constrained

and actual rate of increase of γ – as well as the SST-dependence of the actual rate of increase of γ – can mostly be explained with changes in convective self-aggregation. A higher degree of self-aggregation is accompanied by a stronger overturning circulation and higher subsidence velocity. This explains why γ increases relatively slowly with SST as long as convective aggregation decreases with SST (below 295 K), while γ increases much faster as soon as convective aggregation increases with SST.

Below 295 K, convective self-aggregation increases with a similar rate with decreasing SST both with Nordeng and HalfEntrN due to the WISHE feedback. In NoEntrN, the WISHE feedback is less effective because convection is less inhibited in the subsidence region, which is necessary for the formation of large subsidence regions. In NoCnvPm, convection is too slow to react to the wind-induced variations in surface fluxes. Irrespective of that, NoCnvPm is extremely aggregated because of the extremely high h perturbations that are required in the boundary layer for the onset of large-scale convection (see Chapter 2.4.3). The WISHE feedback is independent of cloud-induced cooling because when disabling the cloud-radiative effects in Nordeng, at low SSTs surface fluxes are similarly large sources of $\langle h \rangle$ variance as with enabled cloud-radiative effects. This outcome differs from *Coppin and Bony* (2015), as in their model enhanced longwave cooling from low-level clouds is crucial for cold pool expansion and the initialization of convective self-aggregation at low SSTs.

2.5.3. Which mechanisms reinforce convective self-aggregation at high SSTs?

An increase of convective self-aggregation with SST has been found with some GCMs (*Coppin and Bony*, 2015; *Arnold and Randall*, 2015) and some convection-permitting models (*Khairoutdinov and Emanuel*, 2010; *Wing and Emanuel*, 2014; *Hohenegger and Stevens*, 2016), but with other convection-permitting models, only a very weak SST dependence was found (*Wing and Cronin*, 2016; *Holloway and Woolnough*, 2016), and the governing mechanisms appear to differ among the models. On the one hand, *Emanuel et al.* (2014) explain the SST dependence of convective self-aggregation with a temperature-dependent moisture-longwave radiation feedback, on the other hand, *Beucler and Cronin* (2016) show that the longwave feedback likely is temperature-dependent, but that clouds and the vertical structure of humidity perturbations can strongly modulate this, and, as a consequence, the longwave feedback could favor self-aggregation even at lower SSTs. In contrast, *Coppin and Bony* (2015) relate the increase of convective self-aggregation at high SSTs to a strengthening of the WISHE feedback.

In our model, the WISHE feedback cannot sustain convective self-aggregation at high SSTs because the covariance of $\langle h \rangle$ and surface fluxes is negative at high SSTs, decreasing the $\langle h \rangle$ variance (Figure 2.7). Instead, the fractional contribution of the moisture-radiation feedback to $\langle h \rangle$ variance increases with SST (Figure 2.7). However, another

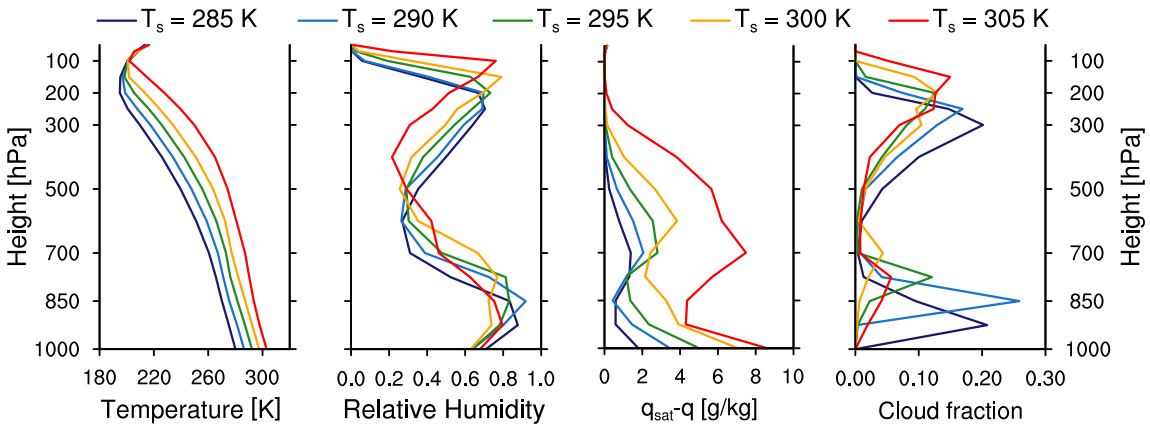

Figure 2.10.: Profiles of atmospheric state variables for different SSTs with Nordeng, averaged over the analysis period and plotted as a function of pressure level. $q_{\mathrm{sat}} - q$ is the difference between saturated specific humidity and domain-mean specific humidity.

self-aggregation mechanism is more directly related to the convective parameterization and is of most importance at high SSTs. The vertical profiles in Figure 2.10 show that the SST increase induces a temperature increase throughout the whole troposphere, while the relative humidity profile depends nonsystematically on SST, changing only by about 10 % in the low troposphere. Consequently, the absolute humidity difference between the saturated air in the updraft and the environmental air increases, which means that the same amount of entrained air can cause more evaporative cooling in the updraft. Hence, the higher the SST, the more effective is entrainment in reducing updraft buoyancy. This is in agreement with *Singh and O'Gorman* (2013) who find that an increase of saturation deficit with SST is accompanied by an increase of CAPE. Greater saturation deficits require higher h perturbations and, as Chapter 2.4.3 has shown, large h perturbations are associated with a high degree of convective self-aggregation (and vice versa).

The SST-dependent entrainment efficiency explains why a moisture-convection feedback (or water vapor-convection feedback, *Tompkins and Semie*, 2017) strengthens with increasing SST. Although *Emanuel et al.* (2014) argue that a moisture-convection feedback is not crucial for self-aggregation, *Craig and Mack* (2013) claim that it is the fundamental feedback. As this moisture-convection feedback directly depends on the convective parameterization, convective self-aggregation is more parameterization-dependent at high SSTs than at low SSTs. Convective self-aggregation increases at high SSTs most with Nordeng, where convection is most sensitive to entrainment, while the increase of convective self-aggregation is weaker and only starts at a higher SST when the entrainment rate is halved (HalfEntrN). In the two extreme cases, NoEntrN and NoCnvPm, convective self-aggregation does not increase at high SSTs because in the first case, no environmental unsaturated air is entrained into the updraft and in the second case, the explicit,

large-scale convection is only weakly influenced by large-scale mixing.

Another mechanism which is commonly associated with convective self-aggregation, an upgradient transport of h by a shallow overturning circulation (*Bretherton et al.*, 2005; *Muller and Held*, 2012; *Wing and Emanuel*, 2014; *Muller and Bony*, 2015), is apparent at high SSTs with Nordeng (Figure 2.9). A shallow overturning circulation causes an upgradient h transport, partly compensating the downgradient h transport by the deep overturning circulation. The overall h transport, calculated from the streamfunction in Figure 2.9, is 29,% smaller at 305 K than at 300 K SST. For the formation of the shallow overturning circulation, a cooling profile in the subsidence region that is more bottom-heavy than the stability profile is the key ingredient (following Equation (2.7)). However, though radiative cooling from low clouds has been found to be a necessary condition for a shallow overturning circulation during the initialization of self-aggregation (*Muller and Held*, 2012), this is not a necessary condition in the later stages of self-aggregation discussed here because the low-level circulation prevails even when cloud-radiative effects are disabled. Instead, a strong gradient in relative humidity at the top of the boundary layer is sufficient to cause enough low-level cooling to trigger the shallow overturning circulation. The shallow overturning circulation occurs at high SSTs with Nordeng, HalfEntrN and NoEntrN, and the governing mechanisms seem to be relatively independent of the convective parameterization.

2.6. Does convective self-aggregation have an effect on climate sensitivity?

Climate sensitivity can be estimated from simulations with different prescribed SSTs based on how the TOA energy budget changes with SST, in analogy to *Cess et al.* (1989; 1990; 1996) and many others. Over the whole range of SSTs, the TOA energy budget changes most with NoCnvPm, followed in decreasing order by Nordeng, HalfEntrN and NoEntrN (Table 2.4). Thus, simulations with strong self-aggregation have on average smaller climate sensitivities. This is presumably related to the uneven horizontal distribution of cloud and water vapor, reducing the impact of two positive feedbacks, the cloud and water vapor feedback. In those simulations where self-aggregation increases with SST, with Nordeng

Table 2.4.: Top-of-atmosphere radiation imbalance R_{TOA}, in $\mathrm{W\,m^{-2}}$. A strong decrease of R_{TOA} with SST implies a small climate sensitivity.

Simulation	285 K	290 K	295 K	300 K	305 K
NoCnvPm	-14.0	-32.7	-38.1	-58.2	-72.6
Nordeng	22.8	7.4	6.8	15.7	-8.5
HalfEntrN	26.7	11.0	16.4	23.8	4.4
NoEntrN	32.6	20.7	29.9	26.0	13.3

and HalfEntrN at high SSTs, climate sensitivity is small (Table 2.4). However, these results should be interpreted with caution because climate sensitivity varies very strongly among the simulations, and there are some ranges where the TOA energy imbalance increases with SST, suggesting that in a mixed-layer ocean simulation there could be jumps between a warm state and a cold state within some simulations. These occurrences of implied negative climate sensitivity are associated with low-level cloud fraction changes (Figure 2.10), leading to strong rates of increase of absorbed solar radiation with SST.

2.7. Summary and Conclusions

In this chapter, we examine how the SST dependence of large-scale convective self-aggregation depends on the convective parameterization. For this purpose, we use the general circulation model ECHAM6 in a nonrotating RCE framework and perform a sensitivity study, changing both the globally uniform SST and the convective parameterization, in particular the entrainment rate. In the analysis, we focus on the stationary state to infer from the large-scale statistics, for example, from the vertically integrated distribution of moist static energy (h), how convection couples to the large-scale circulation, and how the mechanisms that sustain convective self-aggregation differ among the simulations.

We find that the convective parameterization alters the structure of the troposphere through a global reorganization of the large-scale circulation. The emergence of self-aggregation dominates the large-scale statistics, making it difficult to find the trace of how convection is parameterized in the statistics, beyond the fact that the degree of convective self-aggregation depends substantially on the way in which convection is parameterized. The higher the entrainment rate, the higher the buoyancy at cloud base has to be to compensate for the less buoyant air that gets entrained. Stronger perturbations of moist static energy in the boundary layer are associated with enhanced convective self-aggregation for two reasons. First, strong h perturbations can only be created if convection is aggregated on large scales. And second, the high variance of h stabilizes the subsidence region against convection. Whether the h perturbations cause self-aggregation, or whether self-aggregation creates the h perturbations, cannot be distinguished, they just come together.

Large-scale convective self-aggregation is independent of SST when setting the entrainment rate for deep convection to zero, or when removing the convective parameterization from the model. In the first case self-aggregation is always weak, while in the latter case self-aggregation is always very strong. With a nontrivial representation of convective entrainment, we observe a nonmonotonic dependence of large-scale convective self-aggregation on SST. At low SSTs, the large-scale water vapor transport is relatively small compared to local surface fluxes, constraining convective activity to regions with high wind-induced surface moisture fluxes. Thus, for SSTs below 295 K, the increase of convec-

tive self-aggregation with decreasing SST can be explained with the wind-induced surface heat exchange (WISHE) feedback being most important at low SSTs. With Nordeng, convective self-aggregation increases with SST for SSTs above 295 K, while when halving the entrainment rate (HalfEntrN), self-aggregation only increases with SST for SSTs above 300 K. The reason is that the saturation deficit increases with increasing SST, enabling the same amount of entrained air to reduce updraft buoyancy much more efficiently, strengthening the moisture-convection feedback. Consequently, the setup with the highest entrainment rate (Nordeng) shows the strongest increase of convective self-aggregation at high SSTs because larger h perturbations and more convective self-aggregation are necessary to sustain deep convection in a warm atmosphere. Additionally, a strong moisture-longwave radiation feedback and a shallow overturning circulation help to maintain convective self-aggregation at high SSTs.

To conclude, we show that the mechanisms involved in sustaining convective self-aggregation depend on the convective parameterization and that inaccuracies in the parameterization of convection may affect the degree of convective self-aggregation and thus the interaction with the large-scale circulation substantially. Different entrainment rates might explain to some degree why previous literature finds so many different paths to self-aggregation, in particular when convection is parameterized. Especially at high SSTs, a realistic convective parameterization is of crucial importance because convective self-aggregation is mostly constrained by thermodynamic processes that directly depend on the convective parameterization, that is, entrainment efficiency, static stability and radiative cooling. From this perspective, it may well be that the most important task of a convective parameterization is to get the degree of convective aggregation right. An interesting approach might be to tune convective parameterizations based on some metric of convective aggregation in real-world simulations or observations.

This work emphasizes the importance of a realistic convective parameterization for modeling convective self-aggregation. Assumptions and uncertainties introduced by the convective parameterization have a strong influence on how the RCE climate organizes and responds to warming. With respect to climate change, this work implies that the entrainment rate is of particular importance for future projections because of its influence on large-scale convective self-aggregation at high SSTs.

Chapter 3

Estimating bulk entrainment with unaggregated and aggregated convection[1]

> Everything should be made as simple as possible, but not simpler.
>
> *(Albert Einstein, paraphrase)*

To investigate how entrainment is influenced by convective organization, we use the ICON model in a radiative-convective equilibrium framework, with a 1 km spatial grid mesh covering a 600 by 520 km domain. We analyze two simulations, with unaggregated and aggregated convection, and find that, in the lower free troposphere, the bulk entrainment rate increases when convection aggregates. The increase of entrainment rate with aggregation is caused by a strong increase of turbulence in the close environment of updrafts, masking other effects like the increase of updraft size and of static stability with aggregation. Even though entrainment rate increases with aggregation, updraft buoyancy reduction through entrainment decreases because aggregated updrafts are protected by a moist shell. Parameterizations that wish to represent mesoscale convective organization would need to model this moist shell.

[1]This chapter has been published with minor modifications as: Becker, T., C. S. Bretherton, C. Hohenegger and B. Stevens (2018): Estimating bulk entrainment with unaggregated and aggregated convection. *Geophys. Res. Lett.*, **45**, doi:10.1002/2017GL076640.

3.1. Introduction

Many general-circulation model (GCM) studies have identified the entrainment parameter of the convection scheme as being exceptionally important for the climate and climate change simulated by the models (e. g., *Knight et al.*, 2007; *Klocke et al.*, 2011; *Sherwood et al.*, 2014; *Tomassini et al.*, 2015), as well as for the organization of convection (e. g., *Oueslati and Bellon*, 2013; *Arnold and Randall*, 2015; *Tompkins and Semie*, 2017, see also Chapter 2). The concept of entrainment, as it appears in many models, arises from a bulk ansatz whereby convection is modeled by a mass flux whose properties are distinct from the environment through which it rises. Entrainment alters both the convection and its environment, affecting for instance the vertical energy transport, static stability and the cloud profile, as well as the overturning circulation and the organization of convection in the tropics. Although there have already been many attempts to estimate bulk entrainment rate, both from observations (e. g., *Yanai et al.*, 1973; *Esbensen*, 1978) and, more recently, from convection-permitting models (e. g., *Siebesma and Cuijpers*, 1995; *Siebesma et al.*, 2003; *Romps*, 2010; review article by *de Rooy et al.*, 2013), questions arise as to whether, for a cumulus layer of a given depth, the bulk entrainment rate shows a clear dependence on convective organization.

The bulk ansatz, together with a too small parameter space, results in the so-called entrainment dilemma in convective parameterizations: if the entrainment parameter is large, convection is too much suppressed, causing an accumulation of instability, and if the entrainment parameter is small, deep convection occurs too readily, causing a poor distribution of convection in space and time, associated with too little variability. *Mapes and Neale* (2011) hypothesized that the entrainment dilemma could be solved by incorporating convective organization as a new prognostic variable in the convection scheme, which acts as a throttle on the bulk entrainment parameter. When convection organizes, entrainment rate is believed to decrease because entrainment rate is assumed to scale with the inverse of the largest eddy sizes in the updraft (*Morton et al.*, 1956; *Turner*, 1963; *Siebesma*, 1996), and the size of the convective updrafts increases with organization (e. g., *Mapes and Neale*, 2011). When convection organizes into an aggregated cluster, entrainment is also believed to have less impact on updraft buoyancy because the spacing of updrafts reduces, moistening the local environment (e. g., *Mapes and Neale*, 2011; *Feng et al.*, 2015). Despite these hypotheses, the effect of convective organization on entrainment has not yet been systematically investigated.

In this chapter, we test whether convective organization – in the form of convective aggregation – results in the hypothesized decrease of entrainment rate and in the hypothesized decrease of updraft buoyancy reduction through entrainment. We compare bulk entrainment rate estimates for deep convection in two convection-permitting simulations, one with unaggregated and one with aggregated convection, using the ICON model in

a radiative-convective equilibrium (RCE) framework. Even though the bulk ansatz can lead to a substantial (factor of 2) underestimation of the actual entrainment rate (*Romps*, 2010), it has the advantage that results compare well to the entrainment parameter used in convective parameterizations (see Appendix A for how the here discussed results compare to the entrainment rate in the Nordeng convection scheme, Chapter 2).

3.2. Methods

ICON (ICOsahedral Nonhydrostatic) is a unified modeling system developed jointly by the Max Planck Institute for Meteorology and the German Weather Service for global numerical weather prediction and climate studies (*Zängl et al.*, 2015). We use its large-eddy mode (ICON-LEM), developed by *Dipankar et al.* (2015) and evaluated in simulations over Germany by *Heinze et al.* (2017). Our RCE setup is similar to the setup in Chapter 2, consisting of an inertial (nonrotating) frame of reference, a prescribed SST of 300 K, and spatially homogeneous but diurnally varying (solar zenith angle: 0°, solar constant: 1069.3 W m^{-2}) insolation. Analyzing convection and how it self-aggregates in a convection-permitting RCE setup has a long tradition (e. g., *Tompkins and Craig*, 1998; *Bretherton et al.*, 2005), and for the purposes of our study, the RCE setup has the advantage that the degree of convective aggregation can vary strongly, from totally unaggregated convection with a popcorn-like appearance to completely aggregated convection that organizes in a cluster. This makes RCE an attractive 'laboratory' for studying differences in how convection couples to its environment.

To resolve deep convection, the model is run on a triangular grid with 1 km edge length and 64 vertical levels, with a model top at 27 km. The model spans a 600 by 520 km domain in the horizontal ($600 \times 600 \times 2 = 720000$ grid points) with boundary conditions that are periodic in the horizontal. For parameterizations, we use classical Smagorinsky diffusion with the modifications by *Lilly* (1962) to account for thermal stratification, the two-moment mixed-phase bulk microphysical parameterization of *Seifert and Beheng* (2006), and the Rapid Radiation Transfer Model (RRTM) for radiation (*Mlawer et al.*, 1997). For clouds and convection, no parameterizations are used. Two simulations are mainly discussed in this paper: a 90-day simulation initialized from unaggregated conditions that does not self-aggregate and a 60-day simulation restarted from fully aggregated conditions that stays fully aggregated in a horizontally isotropic cluster. The latter simulation is restarted from a 90-day simulation with an identical setup, except that it is performed on a 3 km spatial grid. Due to its coarser resolution, this simulation self-aggregates, in line with *Muller and Held* (2012). Results are compared to this parent 3 km simulation whenever this is beneficial (see Appendix B for more details on the resolution dependence of self-aggregation in ICON-LEM).

To quantify bulk entrainment rate, previous studies have used different tracers, for example a 'purity tracer' (*Romps*, 2010) or a 'radioactive tracer' (*Romps and Kuang*, 2011). *Couvreux et al.* (2010) have used a 'radioactive tracer' to sample boundary-layer thermals. Here we quantify bulk entrainment with a 'radioactive tracer' that is injected in the lowest model level, both for simplicity and because this ensures that updrafts have higher tracer concentrations than their environment. In the atmosphere, the radioactive tracer decays with an e-folding time scale of 4 d. With this decay time scale, tracer decay within the updraft is at most 2 % of the change induced by entrainment, as calculated by dividing the ascent-decay time scale by the dilution time scale. In addition, with this decay time scale, the difference between updraft and environmental tracer concentration is high enough (see Chapter 3.3.1 for details) to get reliable bulk entrainment rate estimates.

Bulk entrainment rate is analyzed using three-hourly output from the last 30 days of each simulation. Grid points are defined to be convective updraft grid points if the upward velocity exceeds $1\,\mathrm{m\,s^{-1}}$ and if the sum of liquid and ice condensate exceeds $0.01\,\mathrm{g\,kg^{-1}}$. To decrease computational cost, the tracer concentration of the air that gets entrained into the updraft is calculated after nearest-neighbor remapping (effectively subsampling) to a 3 km grid. For every subsampled updraft grid point, the environmental tracer concentration is calculated by averaging over all non-updraft grid points on the same model level within a 10 km neighborhood. The updraft (ϕ_u) and environmental (ϕ_e) tracer concentrations are averaged over space and time, whereby an updraft mass flux weighting (*Hohenegger and Bretherton*, 2011) is applied for the updraft tracer concentration ($\hat{\phi}_\mathrm{u}$), to emphasize the importance of strong updrafts. After the weighted averaging, the bulk entrainment rate is estimated following *Betts* (1975):

$$\epsilon = \frac{-\partial_z \hat{\phi}_\mathrm{u}}{\hat{\phi}_\mathrm{u} - \phi_\mathrm{e}}. \tag{3.1}$$

3.3. Results

3.3.1. Aggregated and unaggregated convection in ICON-LEM

Snapshots of the two simulations with unaggregated and aggregated convection (Figure 3.1) illustrate that in the lower troposphere (784 hPa), precipitating and nonprecipitating regions can be well separated with the radioactive tracer. Radioactive tracer concentrations, set to 1.0 at the surface, are about 0.4 or more in the convective updrafts. Outside convective updrafts, the tracer concentration strongly depends on the degree of aggregation. In unaggregated states, the tracer is homogeneously distributed, with tracer concentrations of 0.1 to 0.2. In aggregated states, non-updraft grid points within the convective cluster have larger tracer concentrations (about 0.3), but outside the convective cluster, tracer concentrations are almost zero.

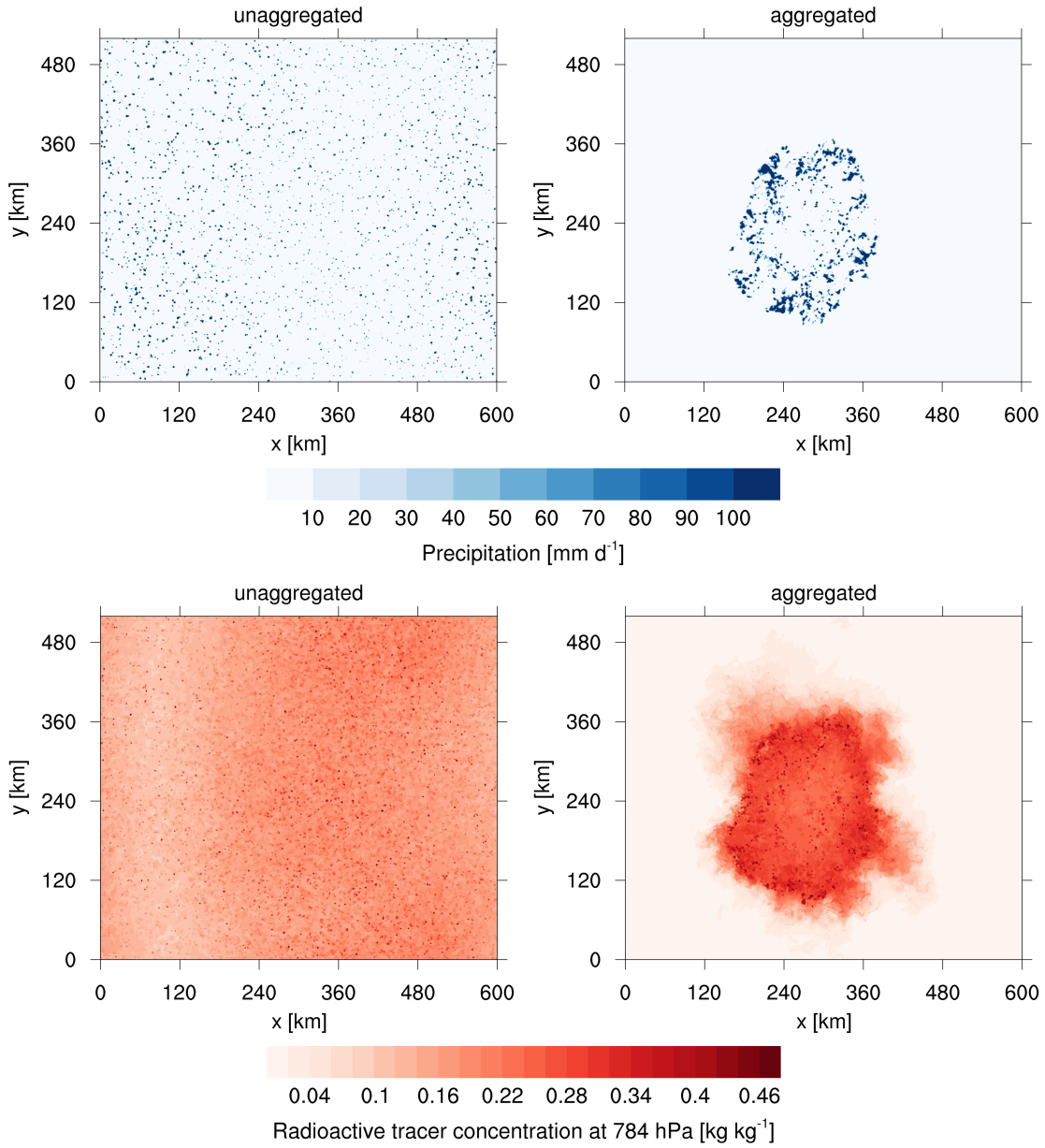

Figure 3.1.: Snapshots of precipitation (3 h mean, top) and radioactive tracer concentration (instantaneous, bottom) with unaggregated and aggregated convection at 784 hPa (2196 m), representing the lower troposphere.

The strongest updrafts, associated with the highest tracer concentration, occur at the edges of the aggregated cluster of convection, in agreement with *Hohenegger and Stevens* (2016). The reason is that these locations are very favorable for convection: moisture convergence in the boundary layer is high, and the free troposphere is relatively moist. Outside the aggregated convective cluster, the dry troposphere suppresses convection. The aggregated convective cluster is very stationary, which implies that the large-scale overturning circulation is well-organized.

3.3.2. Estimating the bulk entrainment rate

The profiles of vertical mass flux and updraft mass flux in Figure 3.2 show that, both with unaggregated and aggregated convection, most updrafts form at or below 900 hPa and detrain at 600 hPa, at the freezing level, or at 200 hPa, at the tropopause (see Appendix C for an analysis of the updraft mass flux profile and bulk detrainment rate). In layers where a lot of updrafts form or detrain, the bulk ansatz reaches its limits because the change of the bulk mean value with height does not necessarily represent the individual updrafts anymore. With aggregated convection, most of the updrafts that fail to penetrate further at the freezing level have small tracer concentrations (see inflection of solid black line in Figure 3.2), probably because those updrafts are too weak to undergo the transition to ice cloud thermodynamics. Because only the strong updrafts with high tracer concentrations survive, the bulk entrainment rate estimate is too small. With unaggregated convection, the bulk ansatz produces reliable results up to the 300 hPa level because updraft dissipation is mostly independent of tracer concentration. Within a 10 km neighborhood around each updraft, environmental tracer concentrations are, in the unaggregated state, close to the mean tracer concentration in the subsidence region. In the aggregated state, however, tracer concentrations are substantially higher close to the updraft than in the large-scale environment, in agreement with Figure 3.1.

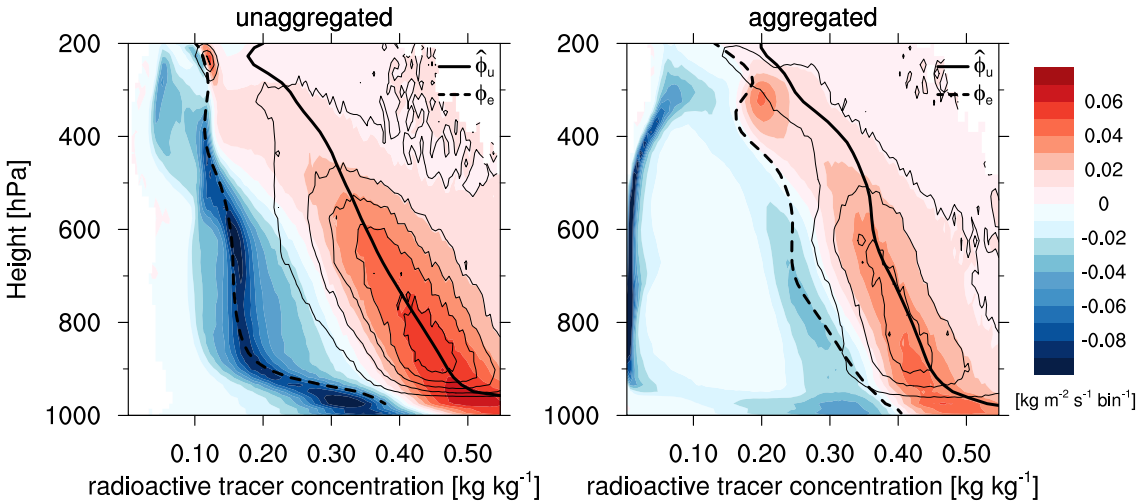

Figure 3.2.: Vertical mass flux in a height - tracer concentration space (bin width: 0.005), both with unaggregated and aggregated convection. Updraft mass flux ($w > 1\,\mathrm{m\,s^{-1}}$, saturated) is represented by black contour lines, with $0.01\,\mathrm{kg\,m^{-2}\,s^{-1}\,bin^{-1}}$ intervals, starting at $0.01\,\mathrm{kg\,m^{-2}\,s^{-1}\,bin^{-1}}$. The solid and dashed thick black lines show the mean vertical profiles of the radioactive tracer in the updraft (mass flux-weighted, $\hat{\phi}_\mathrm{u}$) and in the local environment (10 km neighborhood, ϕ_e), respectively.

Thus, both with unaggregated and aggregated convection, the bulk ansatz works well between 900 and 600 hPa. In line with this, bulk entrainment rate estimates are almost constant with height between 880 and 680 hPa (Figure 3.3). Surprisingly, given the litera-

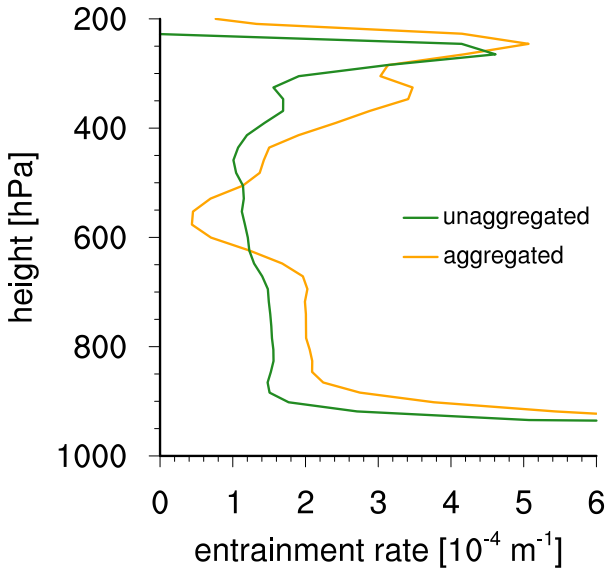

Figure 3.3.: Bulk entrainment rate for unaggregated and aggregated convection, calculated with the radioactive tracer. For the environmental tracer concentration, a 10 km neighborhood is considered around each updraft grid point.

ture cited above, the vertically-averaged (880 to 680 hPa) bulk entrainment rate estimate is in aggregated conditions 40 % higher than in unaggregated conditions (Table 3.1).

Using frozen moist static energy as tracer instead of the radioactive tracer leads to the same result. Over the same height range, the bulk entrainment rate is larger for aggregated ($2.2 \times 10^{-4}\,\mathrm{m}^{-1}$) than for unaggregated convection ($1.7 \times 10^{-4}\,\mathrm{m}^{-1}$). The increase of bulk entrainment rate with aggregation also does not depend on how the bulk environment is defined. For example, in case of aggregated convection, when considering values within a 30 km instead of 10 km neighborhood around each updraft, $\hat{\phi}_\mathrm{u} - \phi_\mathrm{e}$ increases, reducing the bulk entrainment rate estimate (Equation 3.1), but the bulk entrainment rate estimate is still 27 % higher than in case of unaggregated convection. Thus, the considered environmental neighborhood is not responsible for the increase of bulk entrainment rate with aggregation. This is confirmed when comparing, for the aggregated cluster of convection,

Table 3.1.: Vertical averages between 680 and 880 hPa of entrainment rate (ϵ), of domain-mean virtual potential temperature change with height ($\partial_z \Theta_v$), of updraft vertical velocity (w_u), of specific humidity difference between updraft and 10 km neighborhood ($q_\mathrm{v,u} - q_\mathrm{v,e}$), of updraft moist static energy reduction with height (mass flux-weighted, $-\partial_z \hat{h}_\mathrm{u}$), and of updraft buoyancy reduction through entrainment (B_red), calculated from the bulk entrainment rate and specific humidity in a 10 km neighborhood.

	ϵ [10^{-4} m^{-1}]	$\partial_z \Theta_v$ [K km^{-1}]	w_u [m s^{-1}]	$q_\mathrm{v,u} - q_\mathrm{v,e}$ [g kg^{-1}]	$-\partial_z \hat{h}_\mathrm{u}$ [J kg^{-1} m^{-1}]	B_red [J kg^{-1} m^{-1}]
unaggregated	1.52	4.31	3.3	2.51	1.32	0.95
aggregated	2.07	4.93	2.2	1.34	0.95	0.69

bulk entrainment rate estimates in the cluster's inner region (within a 90 km neighborhood around the center of the cluster, defined as the point where water vapor path maximizes, averaged over a 150 km neighborhood) and at its edges (outside the inner region). In the inner region of the aggregated cluster, bulk entrainment rate estimates are higher (inner region: $2.2 \times 10^{-4}\,\mathrm{m}^{-1}$, edge region: $1.9 \times 10^{-4}\,\mathrm{m}^{-1}$), even though the inner region has a more homogeneous environment, and thus the size of the considered updraft neighborhood is less relevant.

Finally, in the simulations with a 3 km grid, the bulk entrainment rate estimate seems to be rather independent of aggregation, or, if anything, its increase with aggregation is small. This suggests that the increase of entrainment rate with aggregation is not an artifact of underresolved convection (*Bryan et al.*, 2003). So there seems to be some resolution dependence, but to the extent that no new process emerges at higher resolution, these results suggest that the increase of entrainment rate with aggregation will become, if anything, more pronounced with increasing resolution. Note that the absolute values of bulk entrainment rate estimates are smaller with a 3 km grid than with a 1 km grid, which is counter to what one would expect if changes in entrainment rate would explain the dependence of self-aggregation on model resolution, as was suggested by *Tompkins and Semie* (2017).

3.3.3. Why does the bulk entrainment rate increase with aggregation?

To find out why bulk entrainment rate increases with aggregation, we analyzed a number of different processes that are known to affect entrainment rate: updraft size, static stability, updraft velocity, organized entrainment and turbulence near the updrafts.

In agreement with conventional wisdom (see also *Mapes and Neale* (2011)), updraft size increases when convection aggregates. At 700 hPa, the mean horizontal updraft extent is $1.9\,\mathrm{km}^2$ for unaggregated convection and $3.6\,\mathrm{km}^2$ for aggregated convection. As entrainment rate is, in the absence of other processes, antiproportional to updraft size (e. g., *Kuang and Bretherton*, 2006; *Khairoutdinov and Randall*, 2006), entrainment rate would decrease when aggregating. Domain mean static stability increases with aggregation (see $\partial_z \Theta_v$ in Table 3.1), which would also tend to decrease the entrainment rate by suppressing small-scale turbulence. A countervailing effect is that, because of the higher stability, updrafts themselves also have smaller vertical velocities when aggregated (Table 3.1). This gives the updrafts on the one hand more time to mix, but on the other hand induces less organized entrainment related to the convergence of mass. Organized entrainment might well be significantly larger in case of aggregated convection because it is accompanied by a more organized large-scale overturning circulation. However, the large-scale flow converges into the updraft grid columns almost entirely below 900 hPa. Directly above, the large-scale flow diverges, forming a shallow overturning circulation (see Appendix B). Though

the flow converges into the aggregated updrafts above that, between 680 and 780 hPa, the average horizontal velocity toward an updraft grid point in a 3 km radius around it is very small, only about $0.035\,\mathrm{m\,s^{-1}}$. As additionally the bulk entrainment rate estimate is constant with height between 680 and 880 hPa, the increase of entrainment rate with aggregation cannot be attributed to organized entrainment.

The only analyzed quantity that is consistent with an increase of entrainment rate with aggregation is resolved small-scale turbulence in the close environment of the updrafts. Because updrafts are very close together in the aggregated state, all of these densely packed updrafts with their respective inflows, outflows and downdrafts generate a lot of shear and turbulence. We quantify turbulence with horizontal turbulence kinetic energy (TKE), which we calculate from cross-sections in x-direction of u-velocity in the non-updraft environment of each individual updraft grid point. To calculate horizontal TKE, we first remove transient motion from the u-velocity, then calculate the kinetic energy, then average over all updraft grid points, and in a last step remove the imprint of the convective overturning circulation on the kinetic energy by subtracting the kinetic energy of the mean u-velocity field. In a 3 km radius around each updraft, the remaining mean horizontal TKE, averaged over 680 to 880 hPa, is $0.11\,\mathrm{J\,kg^{-1}}$ when unaggregated, but $0.65\,\mathrm{J\,kg^{-1}}$ when aggregated, so horizontal TKE has increased sixfold. With a 3 km grid, horizontal TKE increases only by 29 % when aggregating (in a 3 km radius around each updraft), probably because downdrafts are underresolved and less turbulence is resolved. This is in line with the bulk entrainment rate depending less on aggregation, as discussed in the last section.

As mentioned in Chapter 3.3.2, bulk entrainment rate estimates are highest in the inner region of the aggregated cluster. Horizontal TKE is 23 % smaller in the inner region of the convective cluster than at its edges. This seems to refute the idea that changes in horizontal TKE dominate changes in entrainment rate. However, updraft sizes are also slightly (4 %) smaller in the inner region, partly balancing the entrainment reduction effect induced by the decrease of TKE. In addition, the bulk entrainment rate might be underestimated in the edge region. In the edge region, there are often dry regions with very small radioactive tracer concentrations within the considered environmental 10 km neighborhood. If air from the dry regions does not actually get entrained, the bulk entrainment rate will be underestimated (according to Equation 3.1).

3.3.4. How does entrainment affect updraft buoyancy?

The higher entrainment rates in case of aggregated convection do not necessarily imply that updraft buoyancy decreases more with height. The efficiency of entrainment in reducing updraft buoyancy ($-\partial_z \hat{h}_\mathrm{u}$) can be estimated from the moist static energy deficit of the

environmental air (h_e) relative to that in the updraft (h_u),

$$-\partial_z \hat{h}_u = \epsilon \, (h_u - h_e). \tag{3.2}$$

Figure 3.4 shows that, on the 784 hPa level, up to a distance of 20 km to the nearest updraft, the environmental moist static energy is closer to the updraft moist static energy when convection is aggregated. When calculating the environmental moist static energy by averaging, for every updraft grid point, over all non-updraft grid points within a given neighborhood, the results are weighted strongly toward values close to the updrafts and the environmental moist static energy depends less on the selected distance (closed circles in Figure 3.4). In a 10 km neighborhood, the difference between updraft and environmental moist static energy is only half as large for aggregated as for unaggregated convection (Figure 3.4 and Table 3.1). Because of that, $-\partial_z \hat{h}_u$ is 28 % smaller when convection is aggregated (Table 3.1), despite higher entrainment rates. At the edge of the convective cluster, updraft moist static energy decreases even less over the same height range (32 % less than when unaggregated). An air parcel close to aggregated convective updrafts does not only have high values of moist static energy, it also has high values of radioactive tracer concentration, showing that the high moist static energy can be explained with the air parcels history: it got rather recently detrained from one of the nearby updrafts

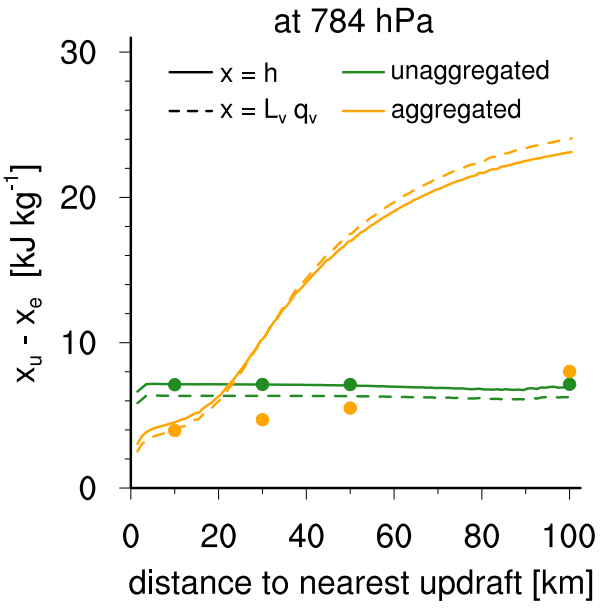

Figure 3.4.: Difference in moist static energy and vapor energy between updraft and environment at 784 hPa (2196 m), representing the lower troposphere. While for the updraft the bulk mean value is considered, the environmental value is sorted by the minimum distance to the closest updraft grid point. Closed circles show the difference in moist static energy between updraft and environment as well (also at 784 hPa), but for the environment, they consider the bulk mean value within the respective neighborhood, calculated in analogy to ϕ_e.

(Figure 3.1). As the differences in environmental moist static energy reflect changes in specific humidity (Figure 3.4), aggregated convection can be thought of being surrounded by a moist shell, even though the domain-averaged troposphere is drier overall.

Because aggregated convection has a moist shell, the same amount of entrained air causes less cloud water to evaporate and cool the updraft (compared to unaggregated convection). Thus, in case of aggregated convection, entrainment is less efficient in reducing updraft buoyancy – even though the bulk entrainment rate is higher. Table 3.1 shows that, in the lower troposphere (680 to 880 hPa), updraft buoyancy reduction through entrainment reduces by 28 % when convection aggregates, reflecting the change in $-\partial_z \hat{h}_\mathrm{u}$.

3.4. Conclusions

In this study, we analyze how bulk entrainment depends on convective aggregation. For this purpose, we use convection-permitting simulations in a nonrotating RCE framework. A 1 km grid is chosen to estimate bulk entrainment rates for deep convection with a 'radioactive tracer', set to 1 at the surface and decaying in the atmosphere with an e-folding time scale of 4 d. Against our initial expectation, we find that the bulk entrainment rate does not decrease with convective aggregation, but increases. Though updraft size and static stability increase, these effects are overcompensated by changes in resolved turbulence kinetic energy (TKE). TKE is much higher in the close environment of updraft grid points in case of aggregated convection because updrafts and downdrafts are very densely packed and generate a lot of shear and turbulence. However, as updrafts are surrounded by a moist shell in the aggregated case, the moister nearby environment wins over the higher entrainment rate, and therefore updrafts experience less buoyancy reduction through entrainment in the aggregated case.

Beyond our RCE study, further work will be needed to explore whether an increase of entrainment rate with aggregation can be reproduced in more realistic setups, for example with convection-permitting simulations of the tropical Atlantic (*Klocke et al.*, 2017).

Our results imply that, in order to represent the effect of aggregation in a convective parameterization, as suggested by *Mapes and Neale* (2011) and *Tobin et al.* (2013), it is not consistent with the involved physical processes to decrease the entrainment rate. Instead, the environment should be adapted. In case of aggregated convection, it is not valid to assume that the properties of the entrained air, especially specific humidity, are well represented by the mean value in the GCM grid cell. Instead, a value that is closer to the value in the updraft should be used. This differentiation between the convective and large-scale environment, the moist shell, thus emerges in our simulations as a fundamental ingredient of convective organization, and should be parameterized in convective parameterizations that wish to represent organization.

Chapter 4

Estimating bulk entrainment in convection-permitting simulations over the tropical Atlantic

> As soon as we have some large computers working, the problems of meteorology will be solved.
>
> *(John von Neumann, 1950)*

In this chapter, we use frozen moist static energy as conserved tracer to investigate how bulk entrainment depends on the aggregation of convection in convection-permitting simulations with a realistic simulation setup for the tropical Atlantic. We quantify aggregation with updraft size and updraft isolation, and find that, in line with Chapter 3, bulk entrainment rate increases when convection is more aggregated. The increase of entrainment rate with aggregation is compensated by a reinforcement of the moist shell, with the consequence that updraft buoyancy does not depend on convective aggregation. We conclude that the increase of entrainment rate with convective aggregation is a phenomenon worth more attention, as it can be reproduced with very different simulation setups.

4.1. Introduction

Radiative-convective equilibrium (RCE) is the simplest way to phrase many important questions about the climate system because RCE constrains the analysis to those processes that matter the most in the tropical troposphere, radiative cooling and convective heating (*Dines*, 1917). The radiative-convective equilibrium framework can be used for a hierarchy of models (e. g., *Jeevanjee et al.*, 2017; *Wing et al.*, 2017a), and thus can bridge the gap between simple models like single-column models (e. g., *Möller*, 1963; *Manabe and Strickler*, 1964) and complex models like cloud-resolving models (e. g., *Tompkins and Craig*, 1998; *Bretherton et al.*, 2005, see also Chapter 3) or general circulation models (e. g., *Held et al.*, 2007; *Popke et al.*, 2013, see also Chapter 2). Precisely for that reason, it is important to take advantage of the wide range of models that RCE studies are applicable to, and as a next step, to test whether findings in RCE studies can be reproduced in models with more realistic initial and boundary conditions (*Holloway*, 2017).

Regarding convective aggregation, taking the next step toward more realistic conditions means that following the analysis of how a process depends on the two extreme states, completely aggregated and completely unaggregated convection (Chapter 3), an analysis should follow on whether the same dependencies can be found when varying convective aggregation only over a range as observed in the tropics (*Tobin et al.*, 2012). The tropical atmosphere usually is in a state between aggregated and unaggregated convection because small-scale heterogeneities often accelerate aggregation, but before the aggregated clusters have had sufficient time to grow (at least 30 d in RCE, see for example *Wing and Emanuel*, 2014), they are mostly disturbed by another heterogeneity.

To calculate bulk entrainment rate, ideally a tracer should be implemented in the model, like a 'purity tracer' (*Romps*, 2010) or a 'radioactive tracer' (*Couvreux et al.*, 2010; *Romps and Kuang*, 2011, see also Chapter 3). If no such tracer is available, a variable that is conserved in convective updrafts can be used instead. Moist static energy (h) is conserved in adiabatic, hydrostatic conditions, even when water droplets fall out of the grid cell or when rain evaporates. Nonadiabatic effects can be neglected because radiative cooling is relatively small on convective time scales, as atmospheric radiative cooling rates are on the order of $1\,\mathrm{K\,d^{-1}}$ (e. g., *Haynes et al.*, 2013). That moist static energy conservation depends on the hydrostatic approximation can be a problem, as it is not precisely valid when applied to a moving, accelerating, convecting parcel. Because of that, *Raymond et al.* (2009) propose to use moist entropy as conserved variable, but here the throttle is that all processes that imply an irreversible generation of entropy need to be considered as source terms, including both liquid and frozen precipitation. Alternatively, liquid moist static energy can be used as conserved variable above the freezing level, and equivalent potential temperature below the freezing level (*Dauhut et al.*, 2017). Here, we use frozen moist static energy (h_f) to calculate bulk entrainment because we have shown in Chapter 3 that

below the freezing level, h_f can be used as conserved variable instead of the 'radioactive tracer'. Compared to the normal formulation of h, h_f has the advantage that it is also conserved under ice formation, though it is not conserved in case of frozen precipitation.

In this chapter, we test whether our finding that, in RCE simulations, bulk entrainment rate increases with aggregation (Chapter 3), is reproducible with convection-permitting simulations over the tropical Atlantic. In Chapter 4.2 we explain our methods and introduce the model we use, in Chapter 4.3 we calculate bulk entrainment for different subdomains, and in Chapter 4.4 we investigate how bulk entrainment rate depends on convective aggregation, which we quantify based on updraft size and updraft isolation.

4.2. Methods and Model

To estimate bulk entrainment over the tropical Atlantic, we take advantage of already existing convection-permitting simulations (*Klocke et al.*, 2017). These simulations were performed in support of the Next Generation Aircraft Remote Sensing for Validation (NARVAL)-South flight campaigns (*Klepp et al.*, 2015; *Stevens et al.*, 2016), which took place in December 2013 and August 2016. For the same time period, the NARVAL simulations were performed with the ICON model, with a 2.5 km horizontal grid spacing, covering the whole tropical Atlantic (68° W - 10° E, 10° S - 20° N, DOM01). Simulations with higher resolution (1.2 km grid spacing) were performed in the western part of DOM01 (64° W to 42° W and from 4° S to 18° N, DOM02), which were online coupled to DOM01 with 2-way nesting and a relaxation time scale of 3 h. In this chapter, we estimate bulk entrainment for DOM02 because the grid spacing in DOM02 resembles the 1 km mesh used in the RCE simulations in Chapter 3, allowing for a relatively easy comparison of results. The only main difference is that this NARVAL simulation was conducted using a different physics package (ICON-NWP). More precisely, the Raschendorfer turbulence scheme (*Raschendorfer*, 2001) and the Lin-type one-moment cloud microphysics scheme (*Lin et al.*, 1983; *Baldauf et al.*, 2011) were used, instead of Smagorinsky turbulence and 2-moment microphysics (see Chapter 3.2 for more details).

The NARVAL simulations were initialized daily at 00 UTC from the atmospheric analysis of the European Center for Medium-Range Weather Forecasts (ECMWF), with a 13 km grid mesh in 2013 and a 9.5 km grid mesh in 2016. Each simulation was run for 36 hours, nudged at the boundaries to the three-hourly ECMWF analyses. Here we use the last 24 hours of each simulation, with 3-hourly output. The NARVAL simulations were run with 75 model levels in the vertical, but because entrainment estimates with frozen moist static energy as tracer are only possible in the lower troposphere below the freezing level, we confine our analysis in the vertical, looking only at 3D fields between roughly 550 and 960 hPa.

With the NARVAL simulations, the 'Calms and Tornadoes' (*Halley*, 1686), later called doldrums, were scientifically rediscovered, an area of calm and variable winds in the deep tropics between the trades (*Klocke et al.*, 2017). This area hosts very different convective phenomena: shallow convection, vortex streets, squall lines, cold pools and organized deep convective clusters, mostly associated with the intertropical convergence zone (ITCZ). Figure 4.1 shows that the ITCZ position is often difficult to locate in individual snapshots, only monthly mean precipitation shows that the ITCZ is roughly located between 0° N and 5° N in December and between 5° N and 10° N in August (Figure 4.1).

We divide DOM02 in 9 subdomains, with $5^\circ \times 5^\circ$ domain size, as indicated in Figure 4.1 by the colored squares. Creating subdomains of this size serves three purposes. First, subdomains that are dominated by shallow convection can be ignored. Second, the subdomain is large enough to get statistically significant results, but small enough to profit from more homogeneous conditions than in the large domain, which allows for more sophisticated and precise estimates of bulk entrainment rate, especially because the dependencies are nonlinear. To be more concrete, a more homogeneous population of updraft moist static energy and updraft depth ensures that the change of updraft moist static energy with height is not biased by updrafts that start or stop in the respective level. And third, dividing into subdomains and calculating entrainment rate in each subdomain provides a sample of different realizations, which can be used to estimate uncertainties.

To calculate bulk entrainment rate, we use h_f as conserved variable, defined as

$$h_\mathrm{f} = c_p T + gz + L_\mathrm{v} q_\mathrm{v} - L_\mathrm{i} q_\mathrm{i}, \tag{4.1}$$

where c_p is the isobaric specific heat capacity, T is temperature, g is gravity, z is geopotential height, L_v is the enthalpy of vaporization, q_v is specific humidity, L_i is the enthalpy of fusion and q_i is specific cloud ice content (representing all ice phases). In agreement with Chapter 3, we calculate bulk entrainment by averaging h_f over all updraft ($w > 1\,\mathrm{m\,s^{-1}}$, $q_\mathrm{l}+q_\mathrm{i} > 0.01\,\mathrm{g\,kg^{-1}}$, $h_\mathrm{f,u}$) and environmental (10 km neighborhood, $h_\mathrm{f,e}$) grid points. When averaging over each subdomain and the respective month, $h_\mathrm{f,u}$ is weighted with the updraft mass flux, called $\hat{h}_\mathrm{f,u}$, in accordance with Chapter 3 and *Hohenegger and Bretherton* (2011). So in analogy to Equation 3.1, the bulk entrainment rate is computed as:

$$\epsilon = \frac{-\partial_z \hat{h}_\mathrm{f,u}}{\hat{h}_\mathrm{f,u} - h_\mathrm{f,e}}. \tag{4.2}$$

The results, averaged over the respective month, are significant. In the total domain, there are at least 1 million updraft grid points in every height layer, and in every subdomain, even well outside the ITCZ, there are at least 10000 updraft grid points in every height layer.

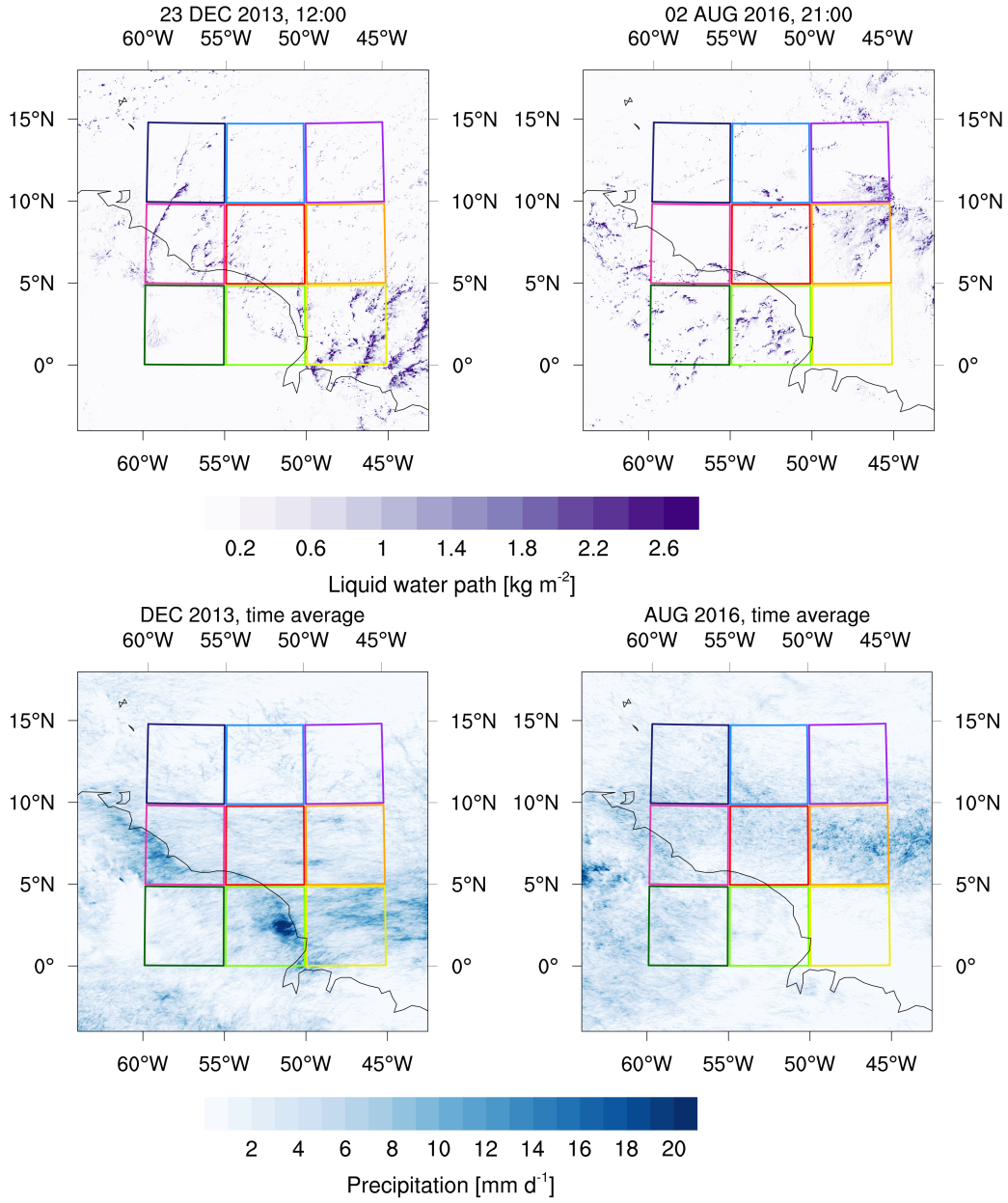

Figure 4.1.: Snapshots of liquid water path in December 2013 and August 2016 (top) and precipitation averaged over each respective month (bottom). The colored squares indicate the different subdomains that we analyze.

4.3. Estimating bulk entrainment in the NARVAL simulations

For each previously defined subdomain (Figure 4.1), we analyze the robustness of the bulk entrainment estimate for deep convection by analyzing the variations of $\hat{h}_{\mathrm{f,u}}$ with height. Subdomains that are located away from the ITCZ in the trade wind region, like in the 45-50 W, 10-15 N subdomain in December 2013, are dominated by shallow convection. Fig-

ure 4.2 shows that in these subdomains, updrafts associated with shallow convection have frozen moist static energies of around 330 K, while deep convective updrafts are associated with frozen moist static energies around 340 K. Because the fraction of shallow convection relative to deep convection decreases with height above 800 hPa, $\hat{h}_{\mathrm{f,u}}$ increases with height, resulting in negative entrainment estimates (see Equation 4.2). In contrast, the 45-50 W, 0-5 N subdomain in December 2013, located in the ITCZ region (Figure 4.1), does not show any of these problems because it is dominated by deep convection (Figure 4.2). With this line of argumentation, we have analyzed for each subdomain in which season the bulk entrainment estimate is less biased by averaging over both shallow and deep convection. We found that the 6 subdomains north of 5° N have robust bulk entrainment estimates for deep convection in August 2016, while the 45-50 W, 0-5 N and 50-55 W, 0-5 N subdomains show robust bulk entrainment estimates for deep convection in December 2013. We will constrain our analysis to this selection of subdomains in the following.

For the 55-60 W, 0-5 N subdomain, which is located over South America, we have decided to ignore entrainment estimates from both seasons because this subdomain is characterized by a deep boundary layer during the day and a high lifting condensation level, shifting the layer with robust bulk entrainment estimates upward. Besides, vertical profiles are influenced in this subdomain by orography, as the elevation reaches 1000 m in a few regions. So in order not to complicate the here presented results with the higher degree of complexity over land, we neglect this subdomain.

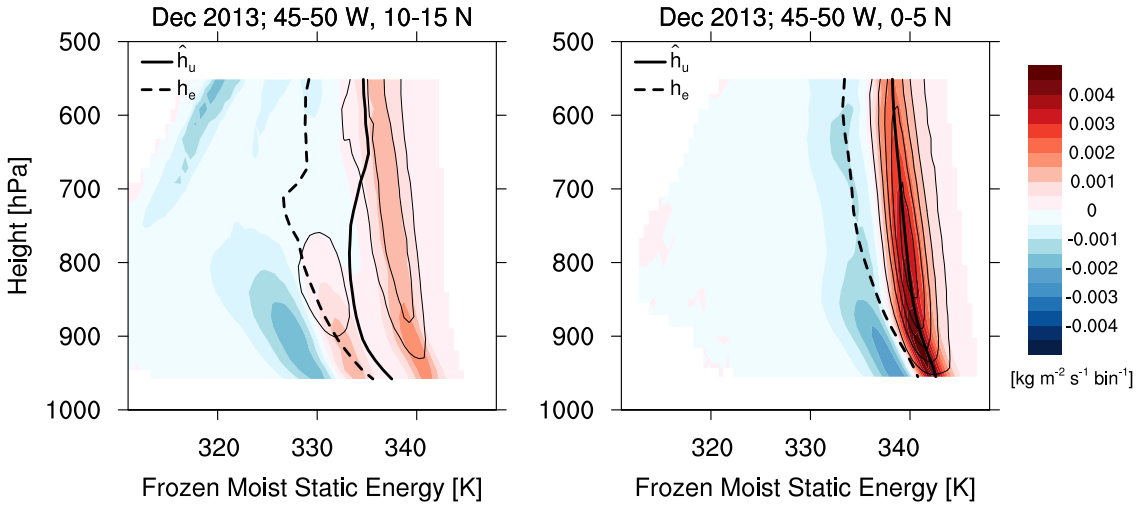

Figure 4.2.: Vertical mass flux in a height - frozen moist static energy space (scaled with the isobaric specific heat capacity; bin width: 0.5 K), for two different subdomains in December 2013. Updraft mass flux ($w > 1\,\mathrm{m\,s^{-1}}$, saturated) is represented by black contour lines, with $0.0005\,\mathrm{kg\,m^{-2}\,s^{-1}\,bin^{-1}}$ intervals, starting at $0.0005\,\mathrm{kg\,m^{-2}\,s^{-1}\,bin^{-1}}$. The solid and dashed thick black lines show the mean vertical profiles of the frozen moist static energy in the updraft (mass flux-weighted, $\hat{h}_{\mathrm{u}}$) and in the local environment (10 km neighborhood, h_{e}), respectively.

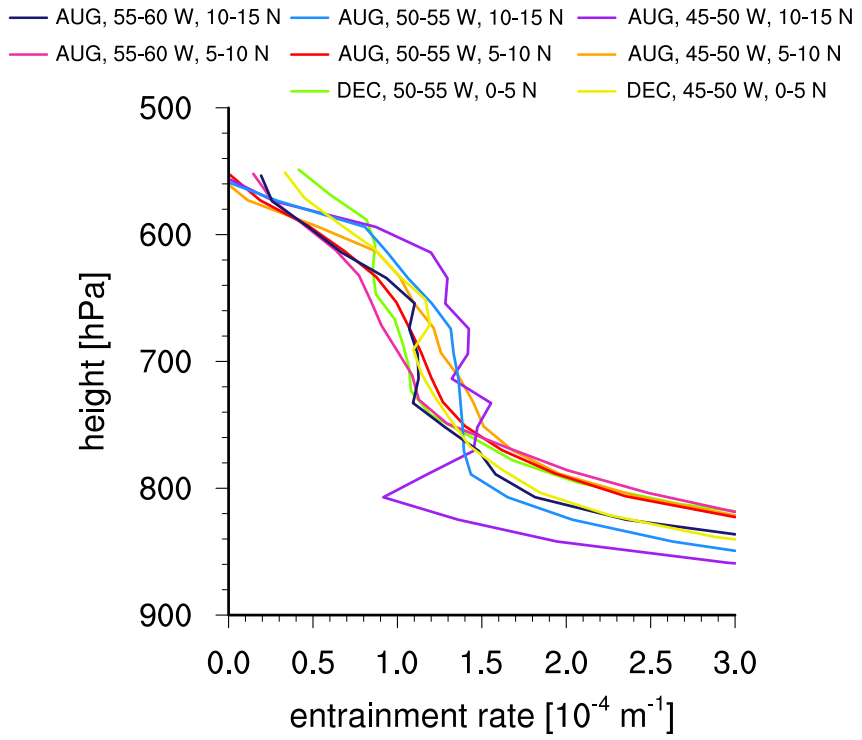

Figure 4.3.: Vertical profiles of bulk entrainment rates in all selected subdomains over December 2013 or August 2016, calculated with frozen moist static energy as conserved variable. The mean frozen moist static energy in the updraft is mass flux-weighted, and a 10 km neighborhood around each updraft grid point is considered for the environment.

For the selected subsample, vertical profiles of bulk entrainment rate are shown in Figure 4.3. Both the shape of the profiles and the average magnitude are in the expected range (e. g., *de Rooy et al.*, 2013, see also Chapter 3). In all subdomains, the bulk entrainment estimates are highest below 800 hPa. This is partly because the bulk entrainment estimates are more dominated by shallow convection here, and partly because of the limitations of the bulk approach. A necessary condition for the bulk approach to produce robust results is that the number of updrafts that originate or detrain in one level is small compared to the number of updrafts that penetrate through that layer (see Chapter 3.3.2 for more details). Figure 4.4 shows that updraft area fraction strongly increases with height roughly up to 800 hPa, and slowly decreases above. Above 800 hPa, bulk entrainment estimates tend to decrease slowly with height, before they decrease faster above 600 hPa. The freezing level is located on average at 570 hPa, but falling ice particles can also influence the layers below, depending on where they melt. This means that bulk entrainment estimates are only trustworthy between 600 and 800 hPa in the NARVAL simulations.

When averaging between 600 and 800 hPa, bulk entrainment estimates are similar in the different subdomains, ranging from 1.11 to $1.34 \times 10^{-4}\,\mathrm{m}^{-1}$ (Table 4.1). Compared to

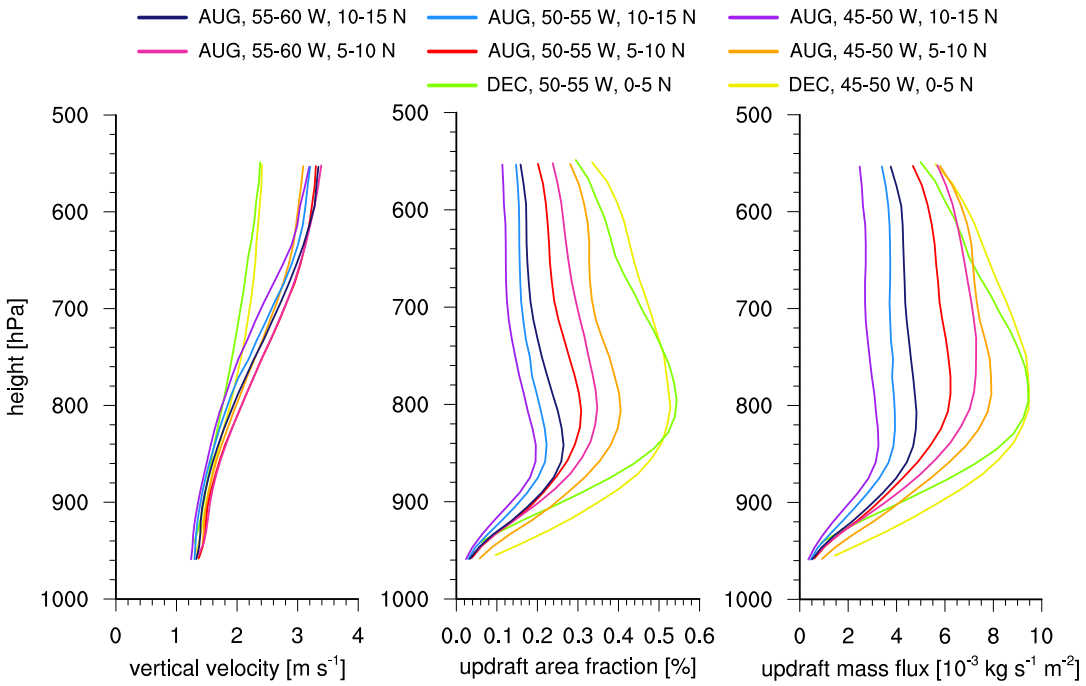

Figure 4.4.: Vertical profiles of bulk updraft velocity, updraft area fraction and updraft mass flux in the selected subdomains over December 2013 or August 2016.

the RCE simulations in Chapter 3, bulk entrainment rates are 20 % smaller than in the RCE case with unaggregated convection (Table 3.1). Nonetheless, the decrease in updraft moist static energy with height is similar to the RCE case with aggregated convection (Table 3.1), at least in all subdomains with August averages. This means that the moist

Table 4.1.: Updraft moist static energy change with height (mass flux-weighted, $-\partial_z \hat{h}_{\mathrm{f,u}}$), difference between frozen moist static energy in the updraft and 10 km neighborhood ($\hat{h}_{\mathrm{f,u}} - h_{\mathrm{f,e}}$) and entrainment rate based on the 10 km neighborhood (see Equation 4.2, ϵ), as well as difference between moist static energy in the updraft and large-scale environment (averaged over the subdomain, $\hat{h}_{\mathrm{f,u}} - h_{\mathrm{f,ls}}$) and entrainment rate when considering the large-scale environment (ϵ_{ls}). Values are given for vertical averages between 600 and 800 hPa for all selected subdomains, averaged over December 2013 or August 2016.

	$-\partial_z \hat{h}_{\mathrm{f,u}}$ [J kg^{-1} m^{-1}]	$\hat{h}_{\mathrm{f,u}} - h_{\mathrm{f,e}}$ [kJ kg^{-1}]	ϵ [10^{-4} m^{-1}]	$\hat{h}_{\mathrm{f,u}} - h_{\mathrm{f,ls}}$ [kJ kg^{-1}]	ϵ_{ls} [10^{-4} m^{-1}]
DEC, 45-50 W, 0-5 N	0.59	4.9	1.20	9.5	0.61
DEC, 50-55 W, 0-5 N	0.49	4.4	1.14	8.6	0.58
AUG, 45-50 W, 5-10 N	0.91	7.1	1.31	9.9	0.92
AUG, 50-55 W, 5-10 N	0.92	7.9	1.19	10.8	0.85
AUG, 55-60 W, 5-10 N	0.84	7.8	1.12	11.0	0.77
AUG, 45-50 W, 10-15 N	1.07	8.0	1.34	13.0	0.82
AUG, 50-55 W, 10-15 N	1.04	8.4	1.26	13.8	0.75
AUG, 55-60 W, 10-15 N	0.95	8.7	1.11	14.3	0.66

shell is less pronounced than in the RCE simulations with aggregated convection, but more pronounced than in the RCE simulation with unaggregated convection, confirming that the tropical troposphere is in a state between these two extremes. The moist shell is only present in the close environment of the updraft, and thus is less well-developed than in RCE with aggregated convection (Figure 4.5). In a 4 km distance to the closest updraft, the amplitude of the h perturbation has, averaged over all subdomains, already reduced to 50 % of the h perturbation in 1 km distance.

Comparing the different subdomains, it is striking that the differences in buoyancy reduction ($-\partial_z \hat{h}_{\mathrm{f,u}}$) are caused by the differences in the moist shell ($\hat{h}_{\mathrm{f,u}} - h_{\mathrm{f,e}}$), not by differences in entrainment, which does not vary much (Table 4.1). For example, the two subdomains with December averages have a well-developed moist shell, as the small values of $\hat{h}_{\mathrm{f,u}} - h_{\mathrm{f,e}}$ indicate, and entrainment is thus very inefficient in reducing updraft buoyancy, as the small values of $-\partial_z \hat{h}_{\mathrm{f,u}}$ indicate. Consequently, updrafts are close to the moist adiabat and, because of weak temperature gradient conditions, the large-scale environment is more stable, feeding back on updraft velocity, which does not increase as much with height as in the other subdomains (Figure 4.4). If instead of the 10 km neighborhood, the whole subdomain is considered ($\hat{h}_{\mathrm{f,u}} - h_{\mathrm{f,ls}}$), the resulting entrainment estimates (ϵ_{ls}) are, not surprisingly, smaller than when considering the 10 km neighborhood, but more importantly, the entrainment estimates vary much more among the subdomains. The

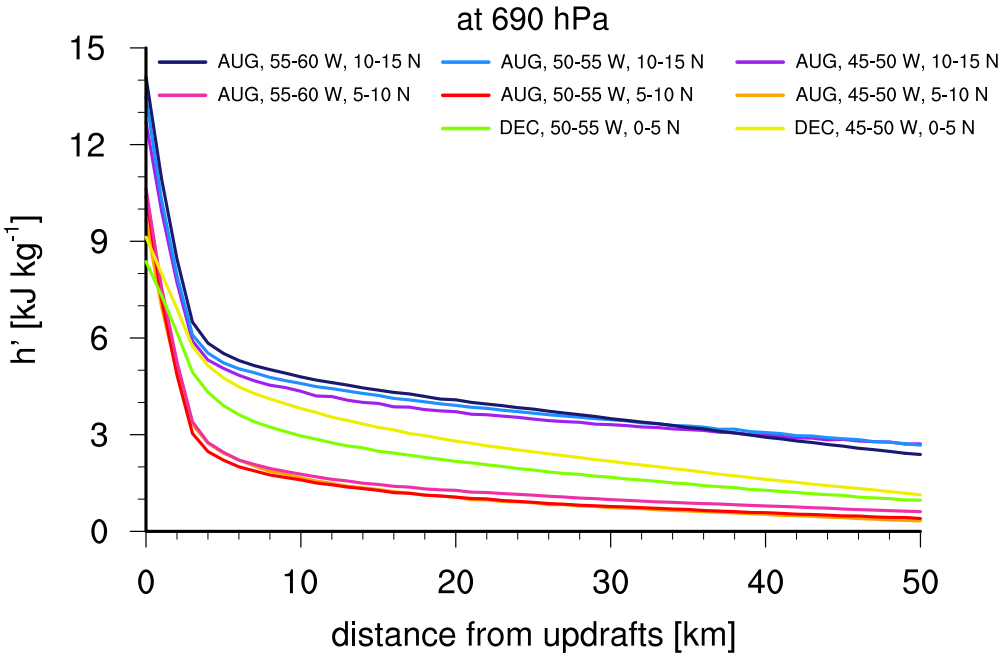

Figure 4.5.: Moist static energy perturbation relative to the large-scale environment (monthly mean, averaged over subdomain) at 690 hPa, sorted by the minimum distance to the closest updraft grid point, for all selected subdomains, averaged over December 2013 or August 2016.

large-scale environment can only in part capture the conditions close to the updraft, and the variability in the shell. So this result again encourages the representation of the moist shell in convective parameterizations, rather than the adjustment of the entrainment rate.

4.4. How does bulk entrainment depend on updraft size and updraft isolation?

To analyze how bulk entrainment depends on the degree of convective aggregation in the NARVAL simulations, we sample, with 3-hourly output, all updrafts in every subdomain based on two criteria: updraft size and updraft isolation. To sample for updraft size, we count with how many updraft grid points each updraft grid point is connected (forming one updraft). This analysis is performed after nearest-neighbor remapping to a rectangular grid with approximately 1.4 km grid spacing. Grid points are considered connected if they share one side (so-called 'four connectivity'). We divide the sample into three groups, 'small', 'medium' and 'large' updrafts, according to the three terciles of each updraft size distribution. Those distributions and some of the first and second terciles are shown in Figure 4.6. As there are fewer small updrafts in the December subdomains, larger updrafts occur more frequently, and thus the first and second terciles have higher values

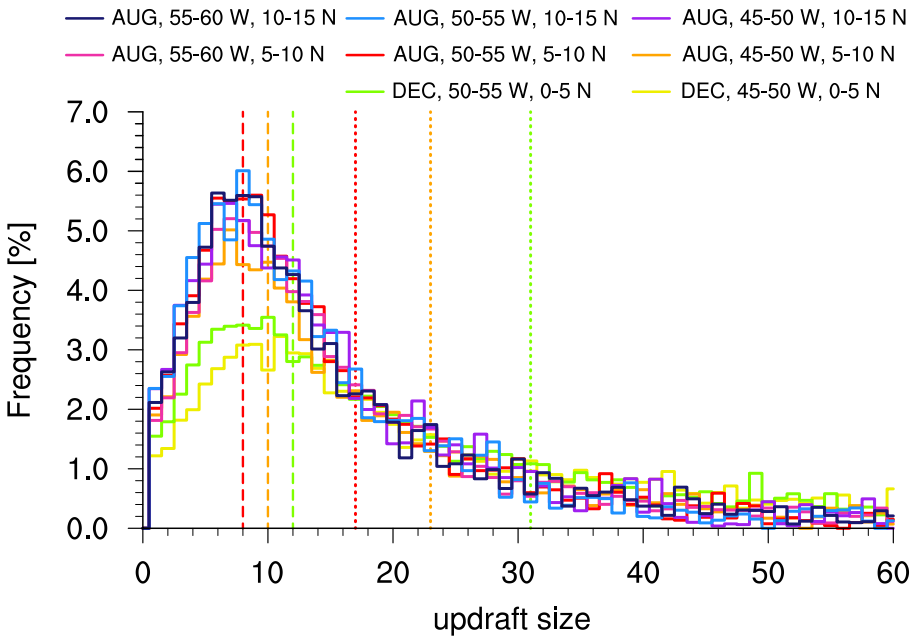

Figure 4.6.: Probability of an updraft grid point to be part of an updraft of a certain size (histogram of updraft size, weighted with the number of updraft grid points per updraft), at 690 hPa, in all selected regions over December 2013 or August 2016. One rectangular updraft grid point covers approximately 1.9 km^2. Vertical dashed lines indicate the first terciles and dotted lines the second terciles of the updraft size distribution for three subdomains.

than in the August subdomains. To sample for updraft isolation, we categorize updrafts in 'isolated' and 'nonisolated', depending on whether or not there are other independent (nonconnected) updrafts in a 10 km neighborhood around the center of the respective updraft. Both categories occur with roughly the same probability.

Figure 4.7 shows that bulk entrainment rate, averaged over the height range where the bulk ansatz provides robust results (600 to 800 hPa), is similar for small and medium size updrafts, but increases robustly by 27 % for large updrafts. In fact, the bulk entrainment estimate increases in every subdomain, both compared to small and medium size updrafts, though the increase is most pronounced for the December subdomains. Figure 4.7 also shows that for nonisolated updrafts, the bulk entrainment rate is about 22 % higher than for isolated updrafts. This again is a robust result, as nonisolated updrafts have higher entrainment rates in all subdomains.

Because both an increase of updraft size, as well as more nonisolated updrafts in a subdomain, are signs of high degrees of convective aggregation (Chapter 3), the here presented results are in line with Chapter 3. In Chapter 3.3.3, we explained the increase of bulk entrainment rate with aggregation with a higher density of updrafts in the local

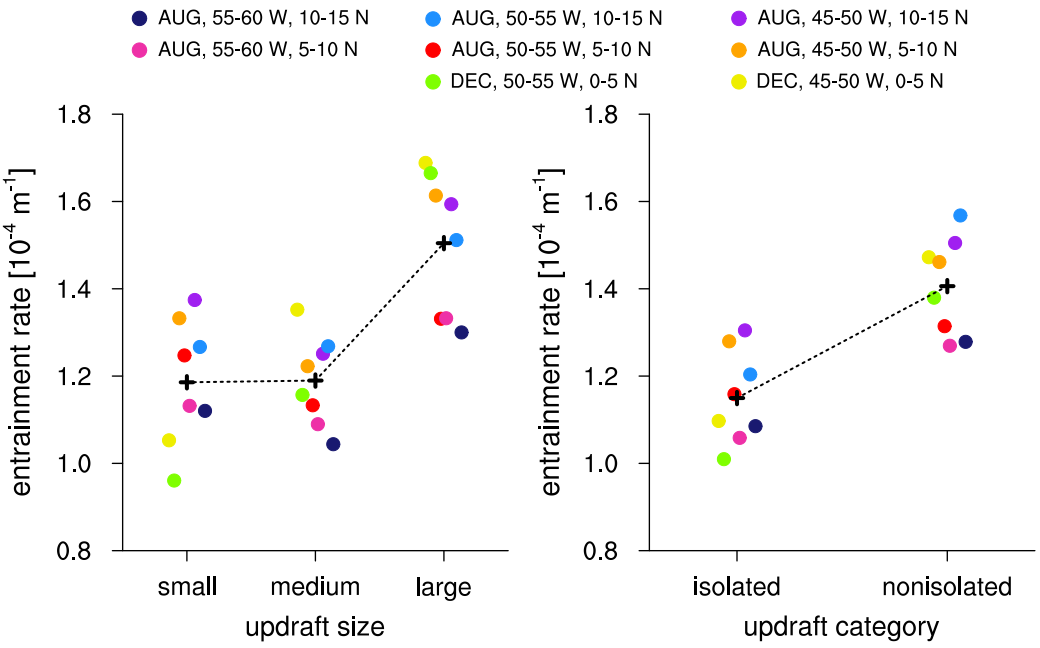

Figure 4.7.: Vertical averages (600 to 800 hPa) of bulk entrainment rates in all selected subdomains, averaged over December 2013 or August 2016. Entrainment rates are ordered by updraft size, where 'small' corresponds to the first tercile, 'medium' to the second tercile and 'large' to the third tercile of the updraft size distribution (left). Updrafts are also categorized in 'isolated' and 'nonisolated', depending on whether or not there are other independent (nonconnected) updrafts in a 10 km neighborhood (right). The black crosses represent the mean value, averaged over all selected subdomains.

environment. The densely packed updrafts, downdrafts, inflows and outflows create a lot of shear and turbulence. In the NARVAL simulations, in 3 grid points distance (3.7 km) to the updraft, horizontal TKE is much higher than in the RCE simulations (in the same distance). However, a direct comparison with the RCE simulations is difficult because the NARVAL setup is much less homogeneous and because the NARVAL and RCE simulations use different turbulence parameterizations. As parameterized turbulence differs, resolved turbulence will differ as well. In all NARVAL subdomains, horizontal TKE increases strongly with increasing updraft size, but horizontal TKE does not depend on updraft isolation. Some of the response must be caused by other mechanisms, a task for future research.

A main finding in Chapter 3 was that, although bulk entrainment rate is higher when convection is aggregated, the efficiency of entrainment to reduce updraft buoyancy is smaller, so $\hat{h}_\mathrm{u}$ decreases less with height. In the NARVAL simulations, the change of $\hat{h}_\mathrm{u}$ with height is relatively independent of updraft size and isolation (Figure 4.8). This means that the increase of bulk entrainment rate with updraft size and isolation is approximately balanced by a decrease of $\hat{h}_\mathrm{u} - h_\mathrm{e}$ (Figure 4.9). Thus, while the moist shell associated with aggregated convection dominates the overall response in RCE, the moist shell intensifies in the NARVAL simulations as well when aggregating, but this effect cannot overcompensate the increase of entrainment rate.

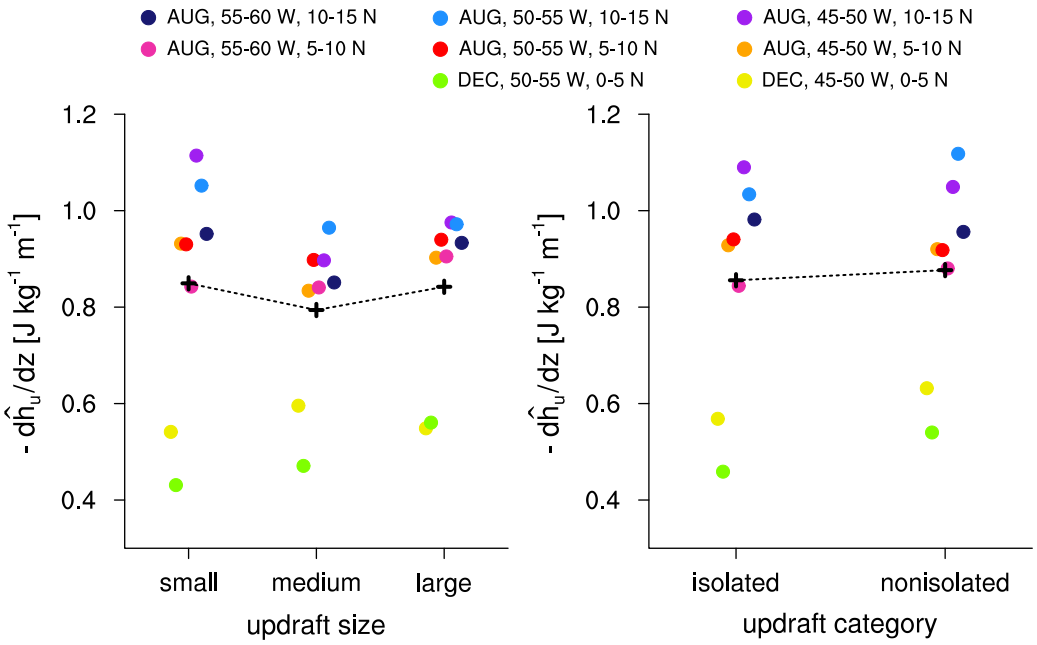

Figure 4.8.: Vertical averages (600 to 800 hPa) of mass flux-weighted updraft moist static energy change with height, in all selected subdomains over December 2013 or August 2016. Results are categorized in analogy to Figure 4.7.

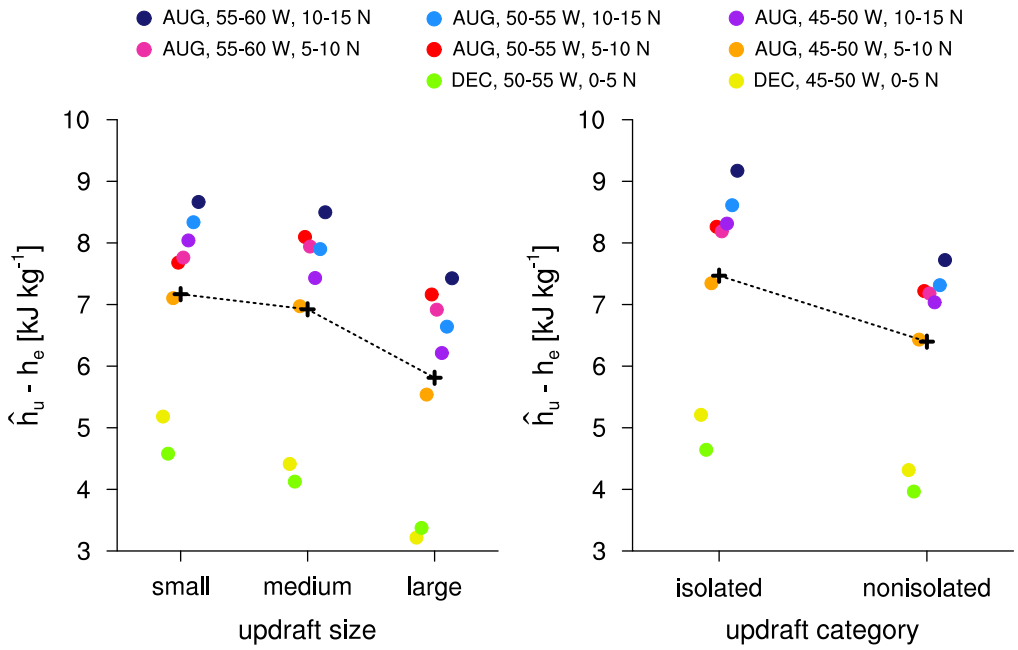

Figure 4.9.: Vertical averages (600 to 800 hPa) of the difference between frozen moist static energy in the updraft (mass flux-weighted) and in the local environment (10 km neighborhood), in all selected subdomains over December 2013 or August 2016. Results are categorized in analogy to Figure 4.7.

To analyze how much our bulk entrainment estimates and our conclusions drawn in this section are biased by shallow convection, we also have calculated bulk entrainment after removing shallow convection from the bulk mean value. For that purpose, we have used the synthetic ICON brightness temperature (T_B) at 10.8 micron (*Senf and Deneke*, 2017), and sampled for $T_B < 275$ K. With this critical value, we exclude the shallow convection that terminates below 700 hPa, but still represent most updrafts that grow deeper, even those that fail to penetrate further at the freezing level. Our conclusions hold also for this subsample: for large updraft sizes, bulk entrainment rate is 9 % higher than for small updraft sizes (in this case medium size updrafts have the smallest bulk entrainment rate), and nonisolated updrafts have a 17 % higher bulk entrainment rate than isolated updrafts.

However, for the $T_B < 275$ K subsample, bulk entrainment rates are 17 % higher than without subsampling (Table 4.1). On first impulse, this seems counter-intuitive, as transitions from shallow to deep convection are known to be accompanied by a reduction in entrainment rate (e. g., *Kuang and Bretherton*, 2006; *de Rooy et al.*, 2013). However, the smaller entrainment rate in case of no subsampling can be explained with the bulk approach: h_u is smaller in case of shallow convection, and as the amount of shallow convection relative to deep convection decreases with height (above 800 hPa, Figure 4.2), $-\partial_z \hat{h}_{f,u}$ is smaller than when subsampling for $T_B < 275$ K, affecting the bulk entrainment estimate as this is the numerator in Equation 4.2.

4.5. Summary and Conclusion

After having analyzed in Chapter 3 how bulk entrainment depends on the aggregation of convection in a radiative-convective equilibrium framework, with unaggregated and aggregated convection, we investigate in this chapter how bulk entrainment depends on convective organization under less idealized conditions. For this purpose, we use convection-permitting simulations over the tropical Atlantic with a 1.2 km spatial grid spacing, which have been run as part of the NARVAL campaigns for December 2013 and August 2016 (*Klocke et al.*, 2017). The NARVAL simulations were not run with a radioactive tracer. Thus, to compute bulk entrainment, we instead use frozen moist static energy as conserved variable. To reduce problems related to heterogeneity within the domain, we select in total 8 subdomains from both seasons that are dominated by deep convection and estimate bulk entrainment rates for these subdomains.

We find that, within a height range that we determined as robust (600 to 800 hPa), bulk entrainment estimates are somewhat smaller in the NARVAL simulations than in RCE. Both differences in the physics, mostly in the parameterization of turbulence, and differences in the setup could explain the smaller entrainment rate. Even though the moist shell is less well-developed than with aggregated convection in RCE, updraft buoyancy reduction through entrainment depends primarily on the strength of the moist shell, while entrainment rate does not depend much on the environment in the different subdomains.

Concerning convective aggregation, our main finding is that bulk entrainment rate increases when convection is more aggregated, which is in line with the results from Chapter 3. Here, we quantify aggregation based on updraft size and updraft isolation. Though small and medium size updrafts have similar bulk entrainment rates, bulk entrainment rate is 27 % higher for large updrafts. Nonisolated updrafts (updrafts that have at least one other separate updraft within a 10 km neighborhood) have 22 % higher entrainment rates than isolated updrafts. Just like in the RCE simulations, the aggregated updrafts find themselves in a moister environment, but unlike in the RCE simulations, the intensification of the moist shell does not overcompensate the increase of entrainment rate with aggregation. Instead, the increase of entrainment rate with aggregation is approximately balanced by the moist shell, with the consequence that the updraft buoyancy reduction through entrainment is relatively independent of convective aggregation.

To conclude, an increase of entrainment rate with convective aggregation is not just a peculiarity of RCE simulations, it can also be reproduced by a more realistic simulation setup that mimics convection over the tropical Atlantic. This chapter emphasizes the importance of the moist shell for updraft buoyancy and suggests that convective parameterizations should, to represent different environments and different degrees of organization, rather adjust the moist shell than the entrainment rate.

Chapter 5

Summary and Conclusions

> Science never solves a problem without creating ten more.
>
> *(George Bernard Shaw)*

In this thesis, our goal was to gain a better understanding of the interaction of precipitating convection with its environment, focusing in particular on the role of convective organization in this interaction. Our approach was to analyze the role of organization in this interaction in two ways, analyzing in Chapter 2 how convective organization depends on the convective parameterization across different climate states, and analyzing in Chapters 3 and 4 how convective organization affects the interaction of convection with its environment. In this chapter, we revisit the three research objectives raised in Chapter 1, followed by some general concluding remarks and an outlook.

5.1. Answering the Research Questions

- **How does the convective parameterization control the temperature dependence of large-scale convective self-aggregation?**

  We tackled this research question with the general circulation model ECHAM6 in a nonrotating radiative-convective equilibrium (RCE) configuration, by examining

how large-scale convective self-aggregation depends on the convective parameterization, in particular on the entrainment parameter, and on the sea-surface temperature (SST). We found that convective self-aggregation and its SST-dependence are very sensitive to the convective parameterization. In fact, the statistics of the large-scale state are dominated by how the convective parameterization controls the self-aggregation of convection, masking the direct impact of the convective parameterization on the large-scale state.

We found that large-scale self-aggregation is independent of SST when the entrainment rate for deep convection is set to zero or when the convective parameterization is removed from the model. When the entrainment parameter is set to zero, convection aggregates very weakly because small perturbations of moist static energy (h) in the boundary layer are sufficient to trigger deep convection, as the convecting plumes do not lose any of their buoyancy due to entrainment. When the convective parameterization is removed from the model, the opposite is true: h perturbations need to be very strong to trigger grid-scale convection. These h perturbations reflect the degree of large-scale convective self-aggregation because convective organization is a necessary condition for large h perturbations, and because a high variance of h stabilizes the subsidence region against convection.

With the default convective parameterization (*Nordeng*, 1994), we detected a non-monotonic dependence of large-scale convective self-aggregation on SST. Below 295 K SST, convection is more aggregated the lower the SST because the wind-induced surface heat exchange (WISHE) feedback is strongest at low SSTs. This can be understood based on thermodynamic reasoning, as surface moisture fluxes get relatively more important for the onset of convection than horizontal moisture convergence. Above 295 K SST, convection is more aggregated the higher the SST because the saturation deficit of entrained air increases with SST. The same amount of entrained air can reduce updraft buoyancy much more efficiently, strengthening the moisture-convection feedback. Thus, at high SSTs, convective aggregation is less controlled by thermodynamic constraints, but more by the entrainment parameter.

- **How does the bulk entrainment rate depend on the degree of convective aggregation?**

  We tackled this research question by using the ICON model in a radiative-convective equilibrium framework, with a 1 km horizontal mesh covering a 600 by 520 km domain. We estimated bulk entrainment rates for deep convection with a 'radioactive tracer' in two simulations, one with unaggregated convection and one with aggregated convection, and found that, against our initial expectation, entrainment rate does not decrease when convection aggregates, but increases by 40 % because updrafts are more densely packed, generating more turbulence. The increase of tur-

bulence masks other effects, like the increase of updraft size, which would in the absence of other effects decrease entrainment rate (*Morton et al.*, 1956; *Turner*, 1963; *Siebesma*, 1996). However, aggregated convection is surrounded by a very pronounced moist shell, and as the nearby moister environment wins over the higher entrainment rate, aggregated updrafts experience 30 % less buoyancy reduction through entrainment.

- **What does the bulk entrainment rate over the tropical Atlantic depend on?**

  To find out whether the main findings related to the previous research question can be reproduced with a more realistic simulation setup, we took advantage of some already existing convection-permitting simulations over the tropical Atlantic (the NARVAL simulations, *Klocke et al.*, 2017). We divided the output into $5° \times 5°$ subdomains, selected those subdomains dominated by deep convection, and estimated bulk entrainment rates below the freezing level with frozen moist static energy as conserved tracer. We found that bulk entrainment estimates are quite similar in the different subdomains, and on average 20 % smaller than in the radiative-convective equilibrium framework with aggregated convection discussed in Chapter 3.

  We quantified convective aggregation based on updraft size and updraft isolation, and found that bulk entrainment rate increases with aggregation, in line with the findings in RCE (Chapter 3). The moist shell intensifies when convection aggregates, but not as strongly as in RCE, with the consequence that the moistening of the convective shell is just strong enough to balance the increase of entrainment rate. Thus, updraft buoyancy reduction through entrainment is relatively independent of convective aggregation in simulations with a realistic simulation setup.

5.2. Conclusions and Implications

The results presented in this thesis show that, in GCMs, the organization of convection and the statistics of the large-scale state are very sensitive to the convective parameterization. To some degree, this might explain why previous literature finds so many different paths to convective self-aggregation, in particular when convection is parameterized. For example, although *Coppin and Bony* (2015) and our work both find an increase of self-aggregation with decreasing SST at low SSTs and with increasing SST at high SSTs, the responsible mechanisms differ. While *Coppin and Bony* (2015) relate this nonmonotonic SST dependency to a stronger radiation-circulation feedback at low SSTs and to a stronger WISHE feedback at high SSTs, we find a stronger WISHE feedback at low SSTs and a stronger moisture-convection feedback at high SSTs. Though these results have to be compared with caution, as *Coppin and Bony* (2015) focused at the mechanisms respon-

sible for the onset of self-aggregation, while we focused on the mechanisms that sustain self-aggregation in the equilibrium state, the comparison still confirms previous literature that has shown how diverse GCM responses in simplified simulation setups can be, mostly because of differences in the representation of clouds and convection (e. g., *Stevens and Bony*, 2013a; *Voigt et al.*, 2014). In this light, the Radiative-Convective Equilibrium Model Intercomparison Project (RCE-MIP) promises exciting results (*Wing et al.*, 2017a).

An increase of saturation deficit with increasing temperature – leading to a higher efficiency of entrainment to reduce updraft buoyancy – implies that in a warmer climate, the interaction of precipitating convection with its environment depends even more critically on the entrainment rate than in a colder climate. Consequently, a realistic convective parameterization is of particular importance for future projections. A collaboration with Gábor Drótos[1] has shown that with a very strong CO_2 forcing, global ECHAM6-RCE simulations coupled to a mixed-layer ocean enter a state where inter-annual variability of global surface temperature about the stationary state becomes very large, a model behavior that can be directly linked to the convective parameterization (*Stevens et al.*, 2018).

From the increase of the entrainment rate for deep convection with convective aggregation, found both in convection-permitting simulations with a radiative-convective equilibrium framework as well as with a more realistic simulation setup for the tropical Atlantic (Chapters 3 and 4), we can conclude that an increase of updraft size with aggregation does not necessarily imply a decrease of entrainment rate. Thus, the idea that convective organization could be represented in convective parameterizations by decreasing the entrainment parameter (*Mapes and Neale*, 2011) is not consistent with our findings. However, the main purpose of the entrainment parameter in a convective parameterization is to reduce updraft buoyancy. With respect to updraft buoyancy, the increase of entrainment rate with aggregation is compensated or overcompensated by a moistening in the local environment of aggregated updrafts (Chapters 3 and 4). This implies that a parameterization that decreases entrainment rate with aggregation, but does not represent the moistening in the local environment of updrafts, can have the right effect on updraft buoyancy, but for the wrong reason.

To conclude, to represent convective aggregation in a convective parameterization in a physically correct way, it would be beneficial to parameterize the convective shell, and to represent aggregation by a moistening of that shell, as the properties of the entrained air, especially specific humidity, are not well represented by the mean value in the GCM grid cell. Our findings also imply that the moist shell is more state-dependent than the entrainment rate for deep convection, which is another reason why a parameterization of the moist shell would be beneficial. To parameterize the moist shell, the shell would need to be defined based on large-scale properties, like large-scale moisture convergence.

[1] Instituto de Física Interdisciplinar y Sistemas Complejos (UIB-CSIC), Palma de Mallorca, Spain

Observations should be used to increase understanding of how the moist shell depends on its large-scale environment. So far, observations have shown that convection is often surrounded by a thin, negatively buoyant shell, with thermodynamic properties significantly different from the large-scale environment (e. g., *Jonas*, 1990; *Rodts et al.*, 2003).

The representation of entrainment in the Nordeng convection scheme, which is used as default convection scheme in ECHAM6 and ICON-ESM, still differs substantially from our bulk entrainment estimates for deep convection based on convection-permitting simulations, as the comparison in Appendix A shows. In the current version of the Nordeng convection scheme, entrainment is only allowed to vary based on how buoyant the updraft is, and how much the updraft is accelerated with height (organized entrainment), although the final entrainment rate is often set by an artificial upper entrainment limit (see Appendix A). We can conclude that, to constrain uncertainties in the entrainment parameter, further studies still need to increase the understanding of the processes that control entrainment rate, and the evolving hypotheses will need to be tested in observational datasets.

5.3. Outlook

During this dissertation, we focused on a few important questions, to which we tried to find some answers and where we wanted to advance the understanding of the underlying physics. But of course, further steps remain that are necessary to verify some of the stated hypotheses, in particular by using observations. In addition, some new interesting questions emerged during the PhD research and remained unanswered. Here we state the most important next steps and the most interesting questions that remain open.

In this thesis, we have shown that one of the most important tasks of a convective parameterization is to get the degree of convective organization right. Thus, it might be possible to tune convective parameterizations based on some metric of large-scale convective aggregation in real-world simulations (*Holloway*, 2017) or observations. In observations, large-scale convective aggregation can be quantified, for example, with the Simple Convective Aggregation Index (SCAI, *Tobin et al.*, 2012), which quantifies convective aggregation based on the number of convective clusters and their clumping. The size of deep convective clusters can be derived from brightness temperatures, which can be measured by operational meteorological satellites (*Tobin et al.*, 2012; *Stein et al.*, 2017). To take things a step further, new observational approaches will need to be explored to test which of the governing mechanisms found in the models are responsible for large-scale convective aggregation in the real world.

Constraining entrainment rate with observations will still remain difficult in the future. Previous work has shown that the entrainment rate is very variable, especially in the transition phase between shallow and deep convection (e. g., *Khairoutdinov and Randall*,

2006; *Del Genio and Wu*, 2010; *de Rooy et al.*, 2013). In light of the strong variability of entrainment rate, in-situ measurements from flight campaigns yield too small datasets, and ground-based measurements are lacking in accuracy to constrain entrainment based on a conserved variable like moist static energy. However, a new approach for a field experiment – in analogy to the 'radioactive tracer' used in Chapter 3 – might be to find an eco-friendly substance that can be emitted in large quantity at the surface below convective clouds, whose 3D distribution can be measured very accurately with ground-based instruments. Such a field experiment could also be used to get new insights into detrainment, which varies much more with height than entrainment, and therefore has a much larger impact on variations in the mass flux profile (*de Rooy and Siebesma*, 2008; *Böing et al.*, 2012, see also Appendix C).

In our convection-permitting RCE simulations, tropospheric stability increases with aggregation, which also has important consequences for convective mass flux, updraft velocity and entrainment. However, the increase of tropospheric stability with aggregation does not necessarily apply to convective aggregation in the tropics, under the assumption of weak temperature gradient conditions (e. g., *Sobel and Bretherton*, 2000). Thus, further convection-permitting RCE simulations that prescribe the large-scale vertical temperature profile would be interesting to analyze, in particular whether there would be any differences in how entrainment rate depends on convective aggregation.

With respect to the NARVAL simulations, the most important next step will be to analyze how entrainment and the convective shell vary across the largest simulation domain, which covers the tropical Atlantic, as well as parts of South America and Africa. Clusters of deep convection differ significantly across this domain, with the largest, most organized clusters of deep convection forming in summer over Africa. Another motivation why it might be interesting to better understand how and why entrainment and the convective shell vary across the Atlantic, is the study of *Siongco et al.* (2017), who looked at the same region with a GCM, and found that there is no simple adjustment to the entrainment parameter that would improve the model results compared to observations for all areas and all seasons.

It would also be useful to quantify convective aggregation in the NARVAL simulations with other metrics than updraft size and updraft isolation, for example with SCAI (*Tobin et al.*, 2012). In addition, more sophisticated approaches that can separate shallow and deep convection without influencing the bulk entrainment estimates should be explored. This would allow for an analysis of how bulk entrainment rates depend on convective aggregation for both shallow and deep convection, across a range of different resolutions and different physics, in particular different turbulence parameterizations. The NARVAL simulations, with their regional refinement of up to 150 m grid spacing, are very well suited to tackle these questions, although the region with regional refinement is located north of the ITCZ region, in which deep convection forms most frequently.

Appendix

A. Comparison of bulk entrainment rate in ICON-LEM with the entrainment parameter in the Nordeng convection scheme

Here we evaluate the entrainment parameter for deep convection that is used in the Nordeng convection scheme (Chapter 2), based on the bulk entrainment estimates in Chapter 3. In the Nordeng convection scheme, the total entrainment rate for deep convection is the sum of the turbulent entrainment rate, which is a constant ($10^{-4}\,\mathrm{m}^{-1}$), and organized entrainment rate, which is assumed to be a function of the acceleration of updraft velocity, and thus a function of CAPE (*Möbis and Stevens*, 2012, Equation 5-7):

$$\epsilon_{\mathrm{org}} = \frac{b}{2}\left(w_{\mathrm{cb}}^2 + \int_{z_{\mathrm{cb}}}^{z} b(z')\,\mathrm{d}z'\right)^{-1} + \frac{1}{\rho}\frac{\mathrm{d}\rho}{\mathrm{d}z}, \tag{A.1}$$

where $w_{\mathrm{cb}}^2 = 1\,\mathrm{m\,s}^{-1}$ is the vertical velocity at cloud base and buoyancy (b) is defined as the density difference between updraft (subscript 'u') and environment (in grid cell, no subscript):

$$b = g\left[\frac{T_{\mathrm{u}} - T}{T} + \left(\frac{R_{\mathrm{v}}}{R_{\mathrm{d}}} - 1\right)(q_{\mathrm{u}} - q) - q_{\mathrm{c,u}}\right], \tag{A.2}$$

where q is the water vapor mixing ratio and q_{c} the mixing ratio of the water condensate. The upper limit of organized entrainment is defined to be $3 \times 10^{-4}\,\mathrm{m}^{-1}$. We apply these formulas to the output of the ICON-LEM simulations both with unaggregated and aggregated convection, and also compare to the total entrainment rate in one of the ECHAM6 simulations from Chapter 2. For best comparability, we use the simulation with 300 K

SST, and average only over those grid points where deep convection is triggered.

We find that, compared to our bulk entrainment estimates in ICON-LEM, the total entrainment rate in ECHAM6, as defined in the Nordeng convection scheme, is too strong, in particular below 700 hPa, where organized entrainment is close to its upper limit (Figure A.1). Below 700 hPa, entrainment rate is almost twice as large as the bulk entrainment estimate for aggregated convection in ICON-LEM. With respect to updraft buoyancy reduction through entrainment, the difference between the two models must be even larger because in ECHAM6, the grid cell mean specific humidity and temperature get entrained, instead of the specific humidity and temperature in the local environment of updrafts.

When applying the formulas for entrainment, as defined in the Nordeng convection scheme (Equation A.1 and A.2), to the bulk updraft in ICON-LEM, the entrainment parameter decreases with aggregation (Figure A.1) because updraft buoyancy is smaller in case of aggregated convection due to a higher static stability. The decrease of entrainment rate with aggregation is opposite to our findings in Chapter 3, where bulk entrainment rate increases with aggregation. However, the decrease of entrainment rate with aggregation is consistent with a smaller buoyancy reduction in case of aggregated convection. Thus, one could argue that the Nordeng scheme is aggregation-aware, assuming that a troposphere with aggregated convection is more stable. However, in ICON-LEM, the smaller buoyancy reduction through entrainment is not caused by a smaller entrainment rate, but by an

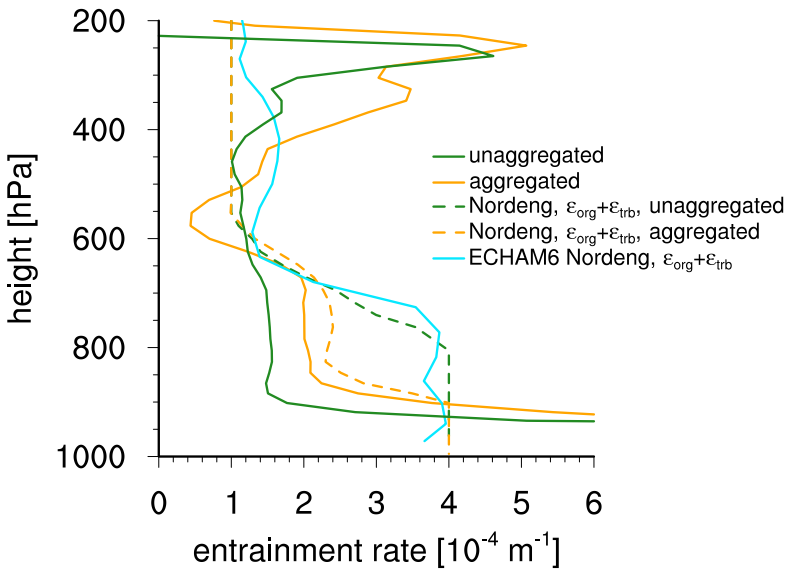

Figure A.1.: Bulk entrainment rate in ICON-LEM, total (sum of turbulent and organized) entrainment rate when applying the formula for organized entrainment in Nordeng (Equation A.1 and A.2) to the bulk updraft in ICON-LEM, and total entrainment rate for deep convection using the Nordeng convection scheme in ECHAM6. The ICON-LEM and ECHAM6 simulations use the same RCE framework with a fixed SST of 300 K. In ICON-LEM, both unaggregated and aggregated convection are considered.

amplification of the moist shell that surrounds the aggregated convection. As the moist shell cannot be modeled by the Nordeng convection scheme, a smaller updraft buoyancy reduction through entrainment in case of aggregated convection is the right result, but for the wrong reason.

Applying the formulas for entrainment in Nordeng to the bulk updraft in ICON-LEM leads, in case of unaggregated convection, to very similar entrainment rates as in ECHAM6 (Figure A.1). Because organized entrainment is a function of updraft buoyancy in the Nordeng convection scheme, the similar entrainment rates illustrate that updraft buoyancies are similar in the ICON-LEM experiment with unaggregated convection and in the simulation with ECHAM6 (using Nordeng with 300 K SST). This means that even though convection is in that ECHAM6 simulation rather aggregated (Figure 2.1), the vertical structure, especially static stability, still resembles more the ICON-LEM atmosphere with unaggregated convection.

B. Why self-aggregation depends on model resolution in ICON-LEM

The analysis in Chapter 3 has shown that ICON-LEM simulations in the RCE framework with 600 by 520 km domain size only self-aggregate if run on a 3 km spatial grid. With a 1 km spatial grid, a 90-day simulation does not self-aggregate, but when started from aggregated conditions it remains aggregated. This resolution dependence of self-aggregation cannot be explained with differences in the entrainment rate, as *Tompkins and Semie* (2017) speculate, because bulk entrainment rate estimates are higher with 1 km grid spacing than with 3 km grid spacing (Chapter 3.3.2).

A sensitivity of self-aggregation to grid spacing was also found by *Muller and Held* (2012), where simulations only self-aggregate if grid spacing is at least 2 km. They explain this finding with the sensitivity of shallow clouds to grid spacing. A cloud-resolving model with coarser grid spacing favors more shallow clouds, and the shallow clouds cause longwave cooling, driving a shallow circulation that induces an upgradient transport of moist static energy, an important ingredient of self-aggregation. In ICON-LEM we find the same mechanism. With a 1 km grid, low-level radiative cooling is weaker than with a 3 km grid, especially when convection is unaggregated (Figure B.1). Thus, with a 1 km grid, the low-level radiative cooling is not strong enough to trigger any significant shallow overturning circulation in case of unaggregated convection (Figure B.2).

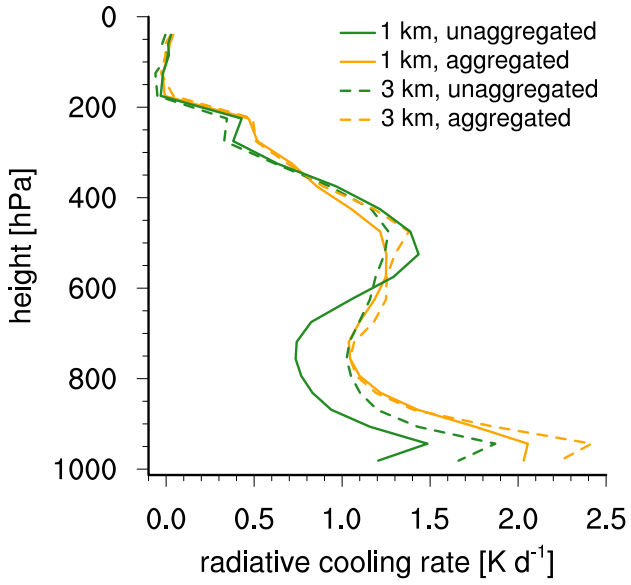

Figure B.1.: Radiative cooling rate with unaggregated and aggregated convection, in the ICON-LEM simulations with 1 km (solid) and 3 km (dashed) grid spacing. For '3 km, unaggregated', the 3 km simulation is averaged over simulation day 21-30, the time span just before the convection self-aggregates.

Once convection is aggregated, low clouds are less crucial for the maintenance of self-aggregation. *Muller and Held* (2012) demonstrate that the maintenance of convective aggregation, when starting the simulation from aggregated conditions, is not sensitive to the model grid spacing. This is because the maintenance of aggregation is primarily controlled by a strong longwave clear-sky cooling in the dry regions, especially at low levels, also yielding a shallow overturning circulation. This explains very well why, with a 1 km grid, there is hysteresis. Unaggregated convection does not self-aggregate because weak low-level radiative cooling does not trigger a shallow overturning circulation. However, in case of aggregated convection, the aggregation is maintained by a shallow overturning circulation (Figure B.2) because the dryness of the nonconvective region allows the boundary layer to cool very efficiently.

These results are in line with our findings in ECHAM6-RCE (Chapter 2.5.3), where an upgradient moist static energy transport helps maintaining convective aggregation. In that chapter we find that the shallow clouds are not a necessary condition for the shallow overturning circulation, but that a strong low-level moisture gradient is sufficient.

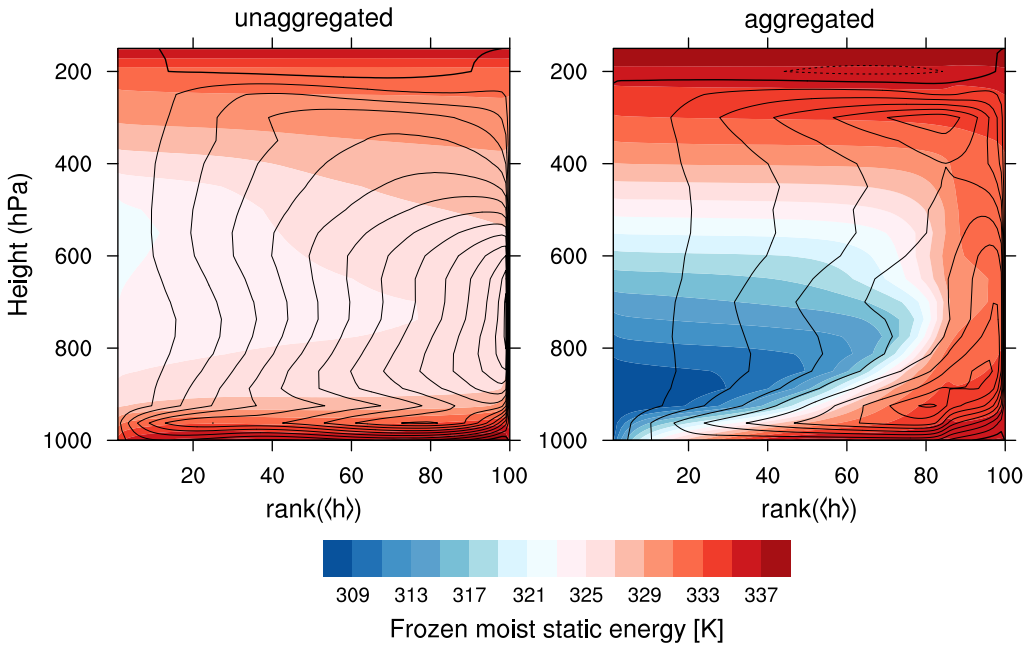

Figure B.2.: Frozen moist static energy and contours of streamfunction (solid: counter-clockwise, dashed: clockwise, thick: zero contour line, every $0.05\,\mathrm{kg\,m^{-2}\,s^{-1}}$), plotted as a function of pressure level and column-integrated frozen moist static energy, for unaggregated and aggregated convection in the ICON-LEM simulations with 1 km grid spacing.

C. Estimating bulk detrainment with unaggregated and aggregated convection

Detrainment regulates the convective outflow and thus the radiative fluxes because detrainment determines in which height levels stratiform clouds form. The bulk detrainment estimate (δ) is more uncertain than the bulk entrainment estimate because we calculate it as a residual from the bulk entrainment rate (ϵ) and from the change of fractional updraft mass flux (M_u) with height:

$$\delta = \epsilon - \frac{1}{M_\mathrm{u}} \frac{\partial}{\partial z} M_\mathrm{u}. \tag{C.1}$$

In general, δ primarily depends on the change of updraft mass flux with height, ϵ is in this equation only of secondary importance. This is true both for shallow convection (*de Rooy and Siebesma*, 2008) and for deep convection (*Böing et al.*, 2012). Thus, the bulk detrainment estimate critically depends on how an updraft is defined. In this thesis, all grid points where upward velocity exceeds $1\,\mathrm{m\,s^{-1}}$ and where the sum of liquid and ice condensate exceeds $0.01\,\mathrm{g\,kg^{-1}}$ are considered updrafts (Chapters 3.2 and 4.2).

The updraft mass flux profile shows that, both for unaggregated and aggregated convection, the updraft mass flux maximizes approximately at 850 hPa and strongly decreases above 600 hPa and at the tropopause, at 200 hPa, because a lot of updrafts are not positively buoyant anymore, resulting in a reduction of updraft area fraction (Figure C.1). In agreement with the mass flux profile, both for unaggregated and aggregated convec-

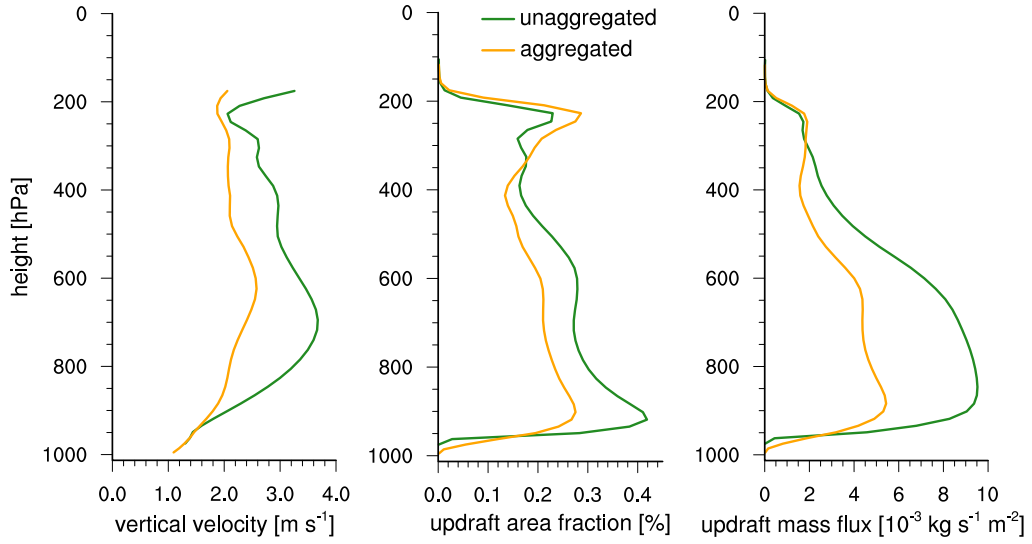

Figure C.1.: Vertical profiles of bulk updraft velocity, updraft area fraction and updraft mass flux with unaggregated and aggregated convection.

tion, bulk detrainment maximizes at 500 hPa and at the tropopause (Figure C.2). The detrainment maximum at or shortly above the freezing level (at 500 hPa) can be explained with an increase of stability in that layer, forcing those updrafts that are too weak to undergo the transition to ice cloud thermodynamics to detrain. With aggregated convection, there is in addition to the two detrainment maxima at 500 and 200 hPa also a maximum at 800 hPa, shortly above the level where the updraft mass flux maximizes. This detrainment maximum can be associated with the shallow overturning circulation (Appendix B).

An interesting side note is that total updraft mass flux is only about half as large for aggregated convection as for unaggregated convection (Figure C.1). This is because updrafts are more effective in convectively heating the troposphere because the troposphere is more stable (Table 3.1), in line with Equation 2.7. Even though radiative cooling is slightly stronger in case of aggregated convection (Figure B.1), which means that, in radiative-convective equilibrium, this has to be compensated by more convective heating, total updraft mass flux does not increase with aggregation because it is dominated by the increase of tropospheric stability.

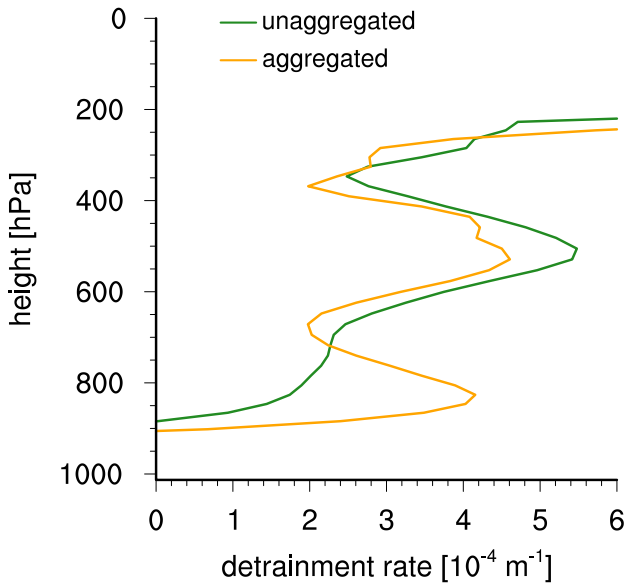

Figure C.2.: Bulk detrainment rate for unaggregated and aggregated convection, calculated based on Equation C.1. Bulk entrainment rate is calculated with the radioactive tracer, and for the environmental tracer concentration, a 10 km neighborhood is considered around each updraft grid point.

Bibliography

Arakawa, A. (2004), The cumulus parameterization problem: Past, present, and future, *Journal of Climate*, *17*(13), 2493–2525, doi:10.1175/1520-0442(2004)017<2493:RATCPP>2.0.CO;2.

Arakawa, A., and W. H. Schubert (1974), Interaction of a cumulus cloud ensemble with the large-scale environment, Part I, *Journal of the Atmospheric Sciences*, *31*(3), 674–701, doi:10.1175/1520-0469(1974)031<0674:IOACCE>2.0.CO;2.

Arakawa, A., and C.-M. Wu (2013), A unified representation of deep moist convection in numerical modeling of the atmosphere. Part I, *Journal of the Atmospheric Sciences*, *70*(7), 1977–1992, doi:10.1175/JAS-D-12-0330.1.

Arnold, N. P., and D. A. Randall (2015), Global-scale convective aggregation: Implications for the MJO, *Journal of Advances in Modeling Earth Systems*, *7*(4), 1499–1518, doi: 10.1002/2015MS000498.

Baldauf, M., A. Seifert, J. Förstner, D. Majewski, M. Raschendorfer, and T. Reinhardt (2011), Operational convective-scale numerical weather prediction with the COSMO model: Description and sensitivities, *Monthly Weather Review*, *139*(12), 3887–3905, doi:10.1175/MWR-D-10-05013.1.

Bechtold, P., J.-P. Chaboureau, A. Beljaars, A. K. Betts, M. Köhler, M. Miller, and J.-L. Redelsperger (2004), The simulation of the diurnal cycle of convective precipitation over land in a global model, *Quarterly Journal of the Royal Meteorological Society*, *130*(604), 3119–3137, doi:10.1256/qj.03.103.

Becker, T., and B. Stevens (2014), Climate and climate sensitivity to changing CO2 on an idealized land planet, *Journal of Advances in Modeling Earth Systems*, *6*(4), 1205–1223, doi:10.1002/2014MS000369.

Bergthorsson, P., B. R. Döös, S. Fryklund, O. Haug, and R. Lindquist (1955), Routine forecasting with the barotropic model, *Tellus*, *7*(2), 272–274, doi:10.1111/j.2153-3490.1955.tb01162.x.

Berner, J., T. Jung, and T. N. Palmer (2012), Systematic model error: The impact of increased horizontal resolution versus improved stochastic and deterministic parameterizations, *Journal of Climate*, *25*(14), 4946–4962, doi:10.1175/JCLI-D-11-00297.1.

Betts, A. K. (1975), Parametric interpretation of trade-wind cumulus budget studies, *Journal of the Atmospheric Sciences*, *32*(10), 1934–1945, doi:10.1175/1520-0469(1975)032<1934:PIOTWC>2.0.CO;2.

Beucler, T., and T. W. Cronin (2016), Moisture-radiative cooling instability, *Journal of Advances in Modeling Earth Systems*, *8*(4), 1620–1640, doi:10.1002/2016MS000763.

Böing, S. J., A. P. Siebesma, J. D. Korpershoek, and H. J. J. Jonker (2012), Detrainment in deep convection, *Geophysical Research Letters*, *39*(20), doi:10.1029/2012GL053735, l20816.

Bony, S., and J.-L. Dufresne (2005), Marine boundary layer clouds at the heart of tropical cloud feedback uncertainties in climate models, *Geophysical Research Letters*, *32*(20), doi:10.1029/2005GL023851, l20806.

Bony, S., and K. A. Emanuel (2005), On the role of moist processes in tropical intraseasonal variability: Cloud - radiation and moisture - convection feedbacks, *Journal of the Atmospheric Sciences*, *62*(8), 2770–2789, doi:10.1175/JAS3506.1.

Bony, S., J.-L. Dufresne, H. Le Treut, J.-J. Morcrette, and C. Senior (2004), On dynamic and thermodynamic components of cloud changes, *Climate Dynamics*, *22*(2), 71–86, doi:10.1007/s00382-003-0369-6.

Bony, S., et al. (2015), Clouds, circulation and climate sensitivity, *Nature Geoscience*, *8*(4), 261–268, doi:10.1038/ngeo2398.

Bony, S., B. Stevens, D. Coppin, T. Becker, K. A. Reed, A. Voigt, and B. Medeiros (2016), Thermodynamic control of anvil cloud amount, *Proceedings of the National Academy of Sciences of the United States of America*, *113*(32), 8927–8932, doi:10.1073/pnas.1601472113.

Bony, S., et al. (2017), EUREC4A: A field campaign to elucidate the couplings between clouds, convection and circulation, *Surveys in Geophysics*, doi:10.1007/s10712-017-9428-0.

Bretherton, C. S., and M. F. Khairoutdinov (2015), Convective self-aggregation feedbacks in near-global cloud-resolving simulations of an aquaplanet, *Journal of Advances in Modeling Earth Systems*, *7*(4), 1765–1787, doi:10.1002/2015MS000499.

Bretherton, C. S., and P. K. Smolarkiewicz (1989), Gravity waves, compensating subsidence and detrainment around cumulus clouds, *Journal of the Atmospheric Sciences*, *46*(6), 740–759, doi:10.1175/1520-0469(1989)046<0740:GWCSAD>2.0.CO;2.

Bretherton, C. S., P. N. Blossey, and M. F. Khairoutdinov (2005), An energy-balance analysis of deep convective self-aggregation above uniform SST, *Journal of the Atmospheric Sciences*, *62*(12), 4273–4292, doi:10.1175/JAS3614.1.

Bryan, G. H., J. C. Wyngaard, and J. M. Fritsch (2003), Resolution requirements for the simulation of deep moist convection, *Monthly Weather Review*, *131*(10), 2394–2416, doi:10.1175/1520-0493(2003)131<2394:RRFTSO>2.0.CO;2.

Cess, R. D., et al. (1989), Interpretation of cloud-climate feedback as produced by 14 atmospheric general circulation models, *Science*, *245*(4917), 513–516, doi:10.1126/science.245.4917.513.

Cess, R. D., et al. (1990), Intercomparison and interpretation of climate feedback processes in 19 atmospheric general circulation models, *Journal of Geophysical Research: Atmospheres*, *95*(D10), 16,601–16,615, doi:10.1029/JD095iD10p16601.

Cess, R. D., et al. (1996), Cloud feedback in atmospheric general circulation models: An update, *Journal of Geophysical Research: Atmospheres*, *101*(D8), 12,791–12,794, doi:10.1029/96JD00822.

Charney, J. G., and A. Eliassen (1964), On the growth of the hurricane depression, *Journal of the Atmospheric Sciences*, *21*(1), 68–75, doi:10.1175/1520-0469(1964)021<0068:OTGOTH>2.0.CO;2.

Charney, J. G., R. Fjörtoft, and J. Von Neumann (1950), Numerical integration of the barotropic vorticity equation, *Tellus*, *2*(4), 237–254, doi:10.1111/j.2153-3490.1950.tb00336.x.

Collins, M., et al. (2013), Long-term climate change: Projections, Commitments and Irreversibility, in *Climate Change 2013: The Physical Science Basis. Contribution of Working Group I to the Fifth Assessment Report of the Intergovernmental Panel on Climate Change*, edited by T. Stocker, D. Qin, G.-K. Plattner, M. Tignor, S. Allen, J. Boschung,

A. Nauels, Y. Xia, V. Bex, and P. Midgley, Cambridge University Press, Cambridge, United Kingdom and New York, NY, USA, doi:10.1017/CBO9781107415324.

Coppin, D., and S. Bony (2015), Physical mechanisms controlling the initiation of convective self-aggregation in a general circulation model, *Journal of Advances in Modeling Earth Systems*, *7*(4), 2060–2078, doi:10.1002/2015MS000571.

Couvreux, F., F. Hourdin, and C. Rio (2010), Resolved versus parametrized boundary-layer plumes. Part I: A parametrization-oriented conditional sampling in large-eddy simulations, *Boundary-Layer Meteorology*, *134*(3), 441–458, doi:10.1007/s10546-009-9456-5.

Craig, G. C., and J. M. Mack (2013), A coarsening model for self-organization of tropical convection, *Journal of Geophysical Research: Atmospheres*, *118*(16), 8761–8769, doi:10.1002/jgrd.50674.

Dauhut, T., J.-P. Chaboureau, P. Mascart, and O. Pauluis (2017), The atmospheric overturning induced by Hector the Convector, *Journal of the Atmospheric Sciences*, *74*(10), 3271–3284, doi:10.1175/JAS-D-17-0035.1.

Davies, L., C. Jakob, P. May, V. V. Kumar, and S. Xie (2013), Relationships between the large-scale atmosphere and the small-scale convective state for Darwin, Australia, *Journal of Geophysical Research: Atmospheres*, *118*(20), 11,534–11,545, doi:10.1002/jgrd.50645.

de Rooy, W. C., and A. P. Siebesma (2008), A simple parameterization for detrainment in shallow cumulus, *Monthly Weather Review*, *136*(2), 560–576, doi:10.1175/2007MWR2201.1.

de Rooy, W. C., et al. (2013), Entrainment and detrainment in cumulus convection: an overview, *Quarterly Journal of the Royal Meteorological Society*, *139*(670), 1–19, doi:10.1002/qj.1959.

Del Genio, A. D., and J. Wu (2010), The role of entrainment in the diurnal cycle of continental convection, *Journal of Climate*, *23*(10), 2722–2738, doi:10.1175/2009JCLI3340.1.

Derbyshire, S. H., I. Beau, P. Bechtold, J.-Y. Grandpeix, J.-M. Piriou, J.-L. Redelsperger, and P. M. M. Soares (2004), Sensitivity of moist convection to environmental humidity, *Quarterly Journal of the Royal Meteorological Society*, *130*(604), 3055–3079, doi:10.1256/qj.03.130.

Dines, W. H. (1917), The heat balance of the atmosphere, *Quarterly Journal of the Royal Meteorological Society*, *43*(182), 151–158, doi:10.1002/qj.49704318203.

Dipankar, A., B. Stevens, R. Heinze, C. Moseley, G. Zängl, M. Giorgetta, and S. Brdar (2015), Large eddy simulation using the general circulation model ICON, *Journal of Advances in Modeling Earth Systems*, *7*(3), 963–986, doi:10.1002/2015MS000431.

Dorrestijn, J., D. T. Crommelin, A. P. Siebesma, H. J. J. Jonker, and C. Jakob (2015), Stochastic parameterization of convective area fractions with a multicloud model inferred from observational data, *Journal of the Atmospheric Sciences*, *72*(2), 854–869, doi:10.1175/JAS-D-14-0110.1.

Emanuel, K., A. A. Wing, and E. M. Vincent (2014), Radiative-convective instability, *Journal of Advances in Modeling Earth Systems*, *6*(1), 75–90, doi:10.1002/2013MS000270.

Emanuel, K. A., D. J. Neelin, and C. S. Bretherton (1994), On large-scale circulations in convecting atmospheres, *Quarterly Journal of the Royal Meteorological Society*, *120*(519), 1111–1143, doi:10.1002/qj.49712051902.

Esbensen, S. (1978), Bulk thermodynamic effects and properties of small tropical cumuli, *Journal of the Atmospheric Sciences*, *35*(5), 826–837, doi:10.1175/1520-0469(1978)035<0826:BTEAPO>2.0.CO;2.

Feng, Z., S. Hagos, A. K. Rowe, C. D. Burleyson, M. N. Martini, and S. P. de Szoeke (2015), Mechanisms of convective cloud organization by cold pools over tropical warm ocean during the AMIE/DYNAMO field campaign, *Journal of Advances in Modeling Earth Systems*, *7*(2), 357–381, doi:10.1002/2014MS000384.

Fläschner, D., T. Mauritsen, and B. Stevens (2016), Understanding the inter-model spread in global-mean hydrological sensitivity, *Journal of Climate*, *29*(2), 801–817, doi:10.1175/JCLI-D-15-0351.1.

Grabowski, W. W., and P. K. Smolarkiewicz (1999), CRCP: a Cloud Resolving Convection Parameterization for modeling the tropical convecting atmosphere, *Physica D: Nonlinear Phenomena*, *133*(1), 171 – 178, doi:10.1016/S0167-2789(99)00104-9.

Grandpeix, J.-Y., and J.-P. Lafore (2010), A density current parameterization coupled with Emanuel's convection scheme. Part I: The models, *Journal of the Atmospheric Sciences*, *67*(4), 881–897, doi:10.1175/2009JAS3044.1.

Guo, H., J.-C. Golaz, L. J. Donner, B. Wyman, M. Zhao, and P. Ginoux (2015), CLUBB as a unified cloud parameterization: Opportunities and challenges, *Geophysical Research Letters*, *42*(11), 4540–4547, doi:10.1002/2015GL063672.

Halley, E. (1686), An historical account of the trade winds, and monsoons, observable in the seas between and near the tropicks, with an attempt to assign the phisical cause of the said wind, *Philosophical Transactions of the Royal Society*, *183*, 153–168.

Haynes, J. M., T. H. Vonder Haar, T. L'Ecuyer, and D. Henderson (2013), Radiative heating characteristics of Earth's cloudy atmosphere from vertically resolved active sensors, *Geophysical Research Letters*, *40*(3), 624–630, doi:10.1002/grl.50145.

Heinze, R., et al. (2017), Large-eddy simulations over Germany using ICON: a comprehensive evaluation, *Quarterly Journal of the Royal Meteorological Society*, *143*(702), 69–100, doi:10.1002/qj.2947.

Held, I. M., and B. J. Soden (2006), Robust responses of the hydrological cycle to global warming, *Journal of Climate*, *19*, 5686–5699.

Held, I. M., R. S. Hemler, and V. Ramaswamy (1993), Radiative-convective equilibrium with explicit two-dimensional moist convection, *Journal of the Atmospheric Sciences*, *50*, 3909–3927, doi:10.1175/1520-0469(1993)050<3909:RCEWET>2.0.CO;2.

Held, I. M., M. Zhao, and B. Wyman (2007), Dynamic radiative-convective equilibria using GCM column physics, *Journal of the Atmospheric Sciences*, *64*(1), 228–238, doi:10.1175/JAS3825.11.

Hohenegger, C., and C. S. Bretherton (2011), Simulating deep convection with a shallow convection scheme, *Atmospheric Chemistry and Physics*, *11*(20), 10,389–10,406, doi:10.5194/acp-11-10389-2011.

Hohenegger, C., and B. Stevens (2013), Preconditioning deep convection with cumulus congestus, *Journal of the Atmospheric Sciences*, *70*(2), 448–464, doi:10.1175/JAS-D-12-089.1.

Hohenegger, C., and B. Stevens (2016), Coupled radiative convective equilibrium simulations with explicit and parameterized convection, *Journal of Advances in Modeling Earth Systems*, *8*(3), 1468–1482, doi:10.1002/2016MS000666.

Hohenegger, C., P. Brockhaus, C. S. Bretherton, and C. Schär (2009), The soil moisture-precipitation feedback in simulations with explicit and parameterized convection, *Journal of Climate*, *22*(19), 5003–5020, doi:10.1175/2009JCLI2604.1.

Hohenegger, C., L. Schlemmer, and L. Silvers (2015), Coupling of convection and circulation at various resolutions, *Tellus A: Dynamic Meteorology and Oceanography*, *67*(1), 26,678, doi:10.3402/tellusa.v67.26678.

Holloway, C. E. (2017), Convective aggregation in realistic convective-scale simulations, *Journal of Advances in Modeling Earth Systems*, *9*(2), 1450–1472, doi:10.1002/2017MS000980.

Holloway, C. E., and S. J. Woolnough (2016), The sensitivity of convective aggregation to diabatic processes in idealized radiative-convective equilibrium simulations, *Journal of Advances in Modeling Earth Systems*, *8*(1), 166–195, doi:10.1002/2015MS000511.

Holloway, C. E., et al. (2014), Understanding and representing atmospheric convection across scales: Recommendations from the meeting held at Dartington Hall, Devon, UK, 28-30 January 2013, *Atmospheric Science Letters*, *15*(4), 348–353, doi:10.1002/asl2.508.

Hourdin, F., et al. (2017), The art and science of climate model tuning, *Bulletin of the American Meteorological Society*, *98*(3), 589–602, doi:10.1175/BAMS-D-15-00135.1.

Houze, R. A. (1982), Cloud clusters and large-scale vertical motions in the tropics, *Journal of the Meteorological Society of Japan. Ser. II*, *60*(1), 396–410, doi:10.2151/jmsj1965.60.1_396.

Houze, R. A. (2004), Mesoscale convective systems, *Reviews of Geophysics*, *42*(4), rG4003, doi:10.1029/2004RG000150.

IPCC (2013), Summary for policymakers, in *Climate Change 2013: The Physical Science Basis. Contribution of Working Group I to the Fifth Assessment Report of the Intergovernmental Panel on Climate Change*, edited by T. Stocker, D. Qin, G.-K. Plattner, M. Tignor, S. Allen, J. Boschung, A. Nauels, Y. Xia, V. Bex, and P. Midgley, pp. 1–30, Cambridge University Press, Cambridge, United Kingdom and New York, NY, USA, doi:10.1017/CBO9781107415324.004.

Jakob, C. (2010), Accelerating progress in global atmospheric model development through improved parameterizations: challenges, opportunities, and strategies, *Bulletin of the American Meteorological Society*, *91*(7), 869–875, doi:10.1175/2009BAMS2898.1.

Jeevanjee, N., and D. M. Romps (2013), Convective self-aggregation, cold pools, and domain size, *Geophysical Research Letters*, *40*(5), 994–998, doi:10.1002/grl.50204.

Jeevanjee, N., P. Hassanzadeh, S. Hill, and A. Sheshadri (2017), A perspective on climate model hierarchies, *Journal of Advances in Modeling Earth Systems*, *9*(4), 1760–1771, doi:10.1002/2017MS001038.

Jonas, P. R. (1990), Observations of cumulus cloud entrainment, *Atmospheric Research*, *25*, 105–127, doi:10.1016/0169-8095(90)90008-Z.

Keane, R. J., and R. S. Plant (2012), Large-scale length and time-scales for use with stochastic convective parametrization, *Quarterly Journal of the Royal Meteorological Society*, *138*(666), 1150–1164, doi:10.1002/qj.992.

Khairoutdinov, M., and D. Randall (2006), High-resolution simulation of shallow-to-deep convection transition over land, *Journal of the Atmospheric Sciences*, *63*(12), 3421–3436, doi:10.1175/JAS3810.1.

Khairoutdinov, M. F., and K. A. Emanuel (2010), Aggregated convection and the regulation of tropical climate, in *Extended Abstracts, 29th Conference on Hurricanes and Tropical Meteorology*, Tucson, AZ, Amer. Meteor. Soc., P2.69.

Khairoutdinov, M. F., and D. A. Randall (2001), A cloud resolving model as a cloud parameterization in the NCAR Community Climate System Model: Preliminary results, *Geophysical Research Letters*, *28*(18), 3617–3620, doi:10.1029/2001GL013552.

Kim, D., A. H. Sobel, E. D. Maloney, D. M. W. Frierson, and I.-S. Kang (2011), A systematic relationship between intraseasonal variability and mean state bias in AGCM simulations, *Journal of Climate*, *24*(21), 5506–5520, doi:10.1175/2011JCLI4177.1.

Klepp, C., F. Ament, S. Bakan, L. Hirsch, and B. Stevens (2015), The NARVAL Campaign Report, *Technical Report 164*, Max Planck Institute for Meteorology, Hamburg, Germany, doi:10.17617/2.2129055.

Klingaman, N. P., and S. J. Woolnough (2014), Using a case-study approach to improve the Madden-Julian Oscillation in the Hadley Centre model, *Quarterly Journal of the Royal Meteorological Society*, *140*(685), 2491–2505, doi:10.1002/qj.2314.

Klingaman, N. P., G. M. Martin, and A. Moise (2017), ASoP (v1.0): a set of methods for analyzing scales of precipitation in general circulation models, *Geoscientific Model Development*, *10*(1), 57–83, doi:10.5194/gmd-10-57-2017.

Klocke, D., R. Pincus, and J. Quaas (2011), On constraining estimates of climate sensitivity with present-day observations through model weighting, *Journal of Climate*, *24*(23), 6092–6099, doi:10.1175/2011JCLI4193.1.

Klocke, D., M. Brueck, C. Hohenegger, and B. Stevens (2017), Rediscovery of the doldrums in storm-resolving simulations over the tropical Atlantic, *Nature Geoscience*, *10*(12), 891–896, doi:10.1038/s41561-017-0005-4.

Knight, C. G., et al. (2007), Association of parameter, software, and hardware variation with large-scale behavior across 57,000 climate models, *Proceedings of the National Academy of Sciences*, *104*(30), 12259–12264, doi:10.1073/pnas.0608144104.

Kuang, Z., and C. S. Bretherton (2006), A mass-flux scheme view of a high-resolution simulation of a transition from shallow to deep cumulus convection, *Journal of the Atmospheric Sciences*, *63*(7), 1895–1909, doi:10.1175/JAS3723.1.

Kumar, V. V., C. Jakob, A. Protat, P. T. May, and L. Davies (2013), The four cumulus cloud modes and their progression during rainfall events: A C-band polarimetric radar perspective, *Journal of Geophysical Research: Atmospheres*, *118*(15), 8375–8389, doi: 10.1002/jgrd.50640.

Kuo, H. L. (1965), On formation and intensification of tropical cyclones through latent heat release by cumulus convection, *Journal of the Atmospheric Sciences*, *22*(1), 40–63, doi:10.1175/1520-0469(1965)022<0040:OFAIOT>2.0.CO;2.

Laing, A. G., and M. J. Fritsch (1997), The global population of mesoscale convective complexes, *Quarterly Journal of the Royal Meteorological Society*, *123*(538), 389–405, doi:10.1002/qj.49712353807.

Lawrence, D. M., and J. M. Slingo (2005), Weak land-atmosphere coupling strength in HadAM3: The role of soil moisture variability, *Journal of Hydrometeorology*, *6*(5), 670–680, doi:10.1175/JHM445.1.

Lilly, D. K. (1962), On the numerical simulation of buoyant convection, *Tellus*, *14*(2), 148–172, doi:10.1111/j.2153-3490.1962.tb00128.x.

Lin, Y.-L., R. D. Farley, and H. D. Orville (1983), Bulk parameterization of the snow field in a cloud model, *Journal of Climate and Applied Meteorology*, *22*(6), 1065–1092, doi:10.1175/1520-0450(1983)022<1065:BPOTSF>2.0.CO;2.

Manabe, S., and K. Bryan (1969), Climate calculations with a combined ocean-atmosphere model, *Journal of the Atmospheric Sciences*, *26*(4), 786–789, doi:10.1175/1520-0469(1969)026<0786:CCWACO>2.0.CO;2.

Manabe, S., and R. F. Strickler (1964), Thermal equilibrium of the atmosphere with a convective adjustment, *Journal of the Atmospheric Sciences*, *21*(4), 361–385, doi: 10.1175/1520-0469(1964)021<0361:TEOTAW>2.0.CO;2.

Manabe, S., and R. T. Wetherald (1967), Thermal equilibrium of the atmosphere with a given distribution of relative humidity, *Journal of the Atmospheric Sciences*, *24*(3), 241–259, doi:10.1175/1520-0469(1967)024<0241:TEOTAW>2.0.CO;2.

Manabe, S., J. Smagorinsky, and R. F. Strickler (1965), Simulated climatology of a general circulation model with a hydrologic cycle, *Monthly Weather Review*, *93*(12), 769–798, doi:10.1175/1520-0493(1965)093<0769:SCOAGC>2.3.CO;2.

Mapes, B., and R. Neale (2011), Parameterizing convective organization to escape the entrainment dilemma, *Journal of Advances in Modeling Earth Systems*, *3*(2), doi: 10.1029/2011MS000042, m06004.

Mapes, B. E. (2016), Gregarious convection and radiative feedbacks in idealized worlds, *Journal of Advances in Modeling Earth Systems*, *8*(2), 1029–1033, doi: 10.1002/2016MS000651.

Marsham, J. H., et al. (2013), The role of moist convection in the West African monsoon system: Insights from continental-scale convection-permitting simulations, *Geophysical Research Letters*, *40*(9), 1843–1849, doi:10.1002/grl.50347.

Mauritsen, T., et al. (2012), Tuning the climate of a gobal model, *Journal of Advances in Modeling Earth Systems*, *4*(M00A01), doi:10.1029/2012MS000154.

Miyamoto, Y., Y. Kajikawa, R. Yoshida, T. Yamaura, H. Yashiro, and H. Tomita (2013), Deep moist atmospheric convection in a subkilometer global simulation, *Geophysical Research Letters*, *40*(18), 4922–4926, doi:10.1002/grl.50944.

Mlawer, E. J., S. J. Taubman, P. D. Brown, M. J. Iacono, and S. A. Clough (1997), Radiative transfer for inhomogeneous atmospheres: RRTM, a validated correlated-k model for the longwave, *Journal of Geophysical Research: Atmospheres*, *102*(D14), 16,663–16,682, doi:10.1029/97JD00237.

Möbis, B., and B. Stevens (2012), Factors controlling the position of the intertropical convergence zone on an aquaplanet, *Journal of Advances in Modeling Earth Systems*, *4*(M00A04), doi:10.1029/2012MS000199.

Möller, F. (1963), On the influence of changes in the CO2 concentration in air on the radiation balance of the Earth's surface and on the climate, *Journal of Geophysical Research*, *68*(13), 3877–3886, doi:10.1029/JZ068i013p03877.

Moncrieff, M. W. (2004), Analytic representation of the large-scale organization of tropical convection, *Journal of the Atmospheric Sciences*, *61*(13), 1521–1538, doi:10.1175/1520-0469(2004)061<1521:AROTLO>2.0.CO;2.

Moncrieff, M. W. (2010), The multiscale organization of moist convection and the intersection of weather and climate, in *Climate Dynamics: Why Does Climate Vary?*, edited by D.-Z. Sun and F. Bryan, pp. 3–26, Geophysical Monograph Series, American Geophysical Union, Washington, doi:10.1029/2008GM000838.

Morton, B. R., G. Taylor, and J. S. Turner (1956), Turbulent gravitational convection from maintained and instantaneous sources, *Proceedings of the Royal Society of London A: Mathematical, Physical and Engineering Sciences*, *234*(1196), 1–23, doi: 10.1098/rspa.1956.0011.

Muller, C. J., and S. Bony (2015), What favors convective aggregation and why?, *Geophysical Research Letters*, *42*(13), 5626–5634, doi:10.1002/2015GL064260.

Muller, C. J., and I. M. Held (2012), Detailed investigation of the self-aggregation of convection in cloud-resolving simulations, *Journal of the Atmospheric Sciences*, *69*(8), 2551–2565, doi:10.1175/JAS-D-11-0257.1.

Muller, C. J., P. A. O'Gorman, and L. E. Back (2011), Intensification of precipitation extremes with warming in a cloud-resolving model, *Journal of Climate*, *24*(11), 2784–2800, doi:10.1175/2011JCLI3876.1.

Narenpitak, P., C. S. Bretherton, and M. F. Khairoutdinov (2017), Cloud and circulation feedbacks in a near-global aquaplanet cloud-resolving model, *Journal of Advances in Modeling Earth Systems*, *9*(2), 1069–1090, doi:10.1002/2016MS000872.

Nesbitt, S. W., E. J. Zipser, and D. J. Cecil (2000), A census of precipitation features in the tropics using TRMM: Radar, ice scattering, and lightning observations, *Journal of Climate*, *13*(23), 4087–4106, doi:10.1175/1520-0442(2000)013<4087:ACOPFI>2.0.CO;2.

Nguyen, H., A. Protat, H. Zhu, and M. Whimpey (2017), Sensitivity of the ACCESS forecast model statistical rainfall properties to resolution, *Quarterly Journal of the Royal Meteorological Society*, *143*(705), 1967–1977, doi:10.1002/qj.3056.

Nordeng, T. E. (1994), Extended versions of the convective parametrization scheme at ECMWF and their impact on the mean and transient activity of the model in the tropics, *Technical Report ECMWF*, *206*, European Center for Medium-Range Weather Forecasts, Reading, UK.

O'Gorman, P. A., and C. J. Muller (2010), How closely do changes in surface and column water vapor follow Clausius-Clapeyron scaling in climate change simulations?, *Environmental Research Letters*, *5*(2), 025,207, doi:10.1088/1748-9326/5/2/025207.

Ooyama, K. (1964), A dynamical model for the study of tropical cyclone development, *Geofísica Internacional,*, *4*, 187–198.

Oueslati, B., and G. Bellon (2013), Convective entrainment and large-scale organization of tropical precipitation: Sensitivity of the CNRM-CM5 hierarchy of models, *Journal of Climate*, *26*(9), 2931–2946, doi:10.1175/JCLI-D-12-00314.1.

Peters, K., C. Jakob, L. Davies, B. Khouider, and A. J. Majda (2013), Stochastic behavior of tropical convection in observations and a multicloud model, *Journal of the Atmospheric Sciences*, *70*(11), 3556–3575, doi:10.1175/JAS-D-13-031.1.

Peters, K., T. Crueger, C. Jakob, and B. Möbis (2017), Improved MJO-simulation in ECHAM6.3 by coupling a Stochastic Multicloud Model to the convection scheme, *Journal of Advances in Modeling Earth Systems*, *9*(1), 193–219, doi:10.1002/2016MS000809.

Phillips, N. A. (1956), The general circulation of the atmosphere: A numerical experiment, *Quarterly Journal of the Royal Meteorological Society*, *82*(352), 123–164, doi: 10.1002/qj.49708235202.

Pincus, R., and B. Stevens (2013), Paths to accuracy for radiation parameterizations in atmospheric models, *Journal of Advances in Modeling Earth Systems*, *5*(2), 225–233, doi:10.1002/jame.20027.

Plant, R. S., and G. C. Craig (2008), A stochastic parameterization for deep convection based on equilibrium statistics, *Journal of the Atmospheric Sciences*, *65*(1), 87–105, doi:10.1175/2007JAS2263.1.

Popke, D., B. Stevens, and A. Voigt (2013), Climate and climate change in a radiative convective equilibrium version of ECHAM6, *Journal of Advances in Modeling Earth Systems*, *5*(1), 1–14, doi:10.1029/2012MS000191.

Raga, G. B., J. B. Jensen, and M. B. Baker (1990), Characteristics of cumulus band clouds off the coast of Hawaii, *Journal of the Atmospheric Sciences*, *47*(3), 338–356, doi:10.1175/1520-0469(1990)047<0338:COCBCO>2.0.CO;2.

Ramanathan, V., and J. A. Coakley (1978), Climate modeling through radiative-convective models, *Reviews of Geophysics and Space Physics*, *16*(4), 465–489, doi: 10.1029/RG016i004p00465.

Randall, D., M. Khairoutdinov, A. Arakawa, and W. Grabowski (2003), Breaking the cloud parameterization deadlock, *Bulletin of the American Meteorological Society*, *84*(11), 1547–1564, doi:10.1175/BAMS-84-11-1547.

Randall, D., et al. (2007), Climate models and their evaluation, in *Climate Change 2007: The Physical Science Basis. Contribution of Working Group I to the Fourth Assessment Report of the Intergovernmental Panel on Climate Change*, edited by S. Solomon, D. Qin, M. Manning, Z. Chen, M. Marquis, K. B. Averyt, M. Tignor, and H. L. Miller, pp. 589–662, Cambridge University Press, Cambridge, United Kingdom and New York, NY, USA, doi:10.1017/CBO9781107415324.

Raschendorfer, M. (2001), The new turbulence parameterization of LM, *COSMO Newsletter No. 1*, pp. 89–97.

Raymond, D. J. (1995), Regulation of moist convection over the West Pacific Warm Pool, *Journal of the Atmospheric Sciences*, *52*(22), 3945–3959, doi:10.1175/1520-0469(1995)052<3945:ROMCOT>2.0.CO;2.

Raymond, D. J. (1997), *Boundary Layer Quasi-Equilibrium (BLQ)*, pp. 387–397, Springer Netherlands, Dordrecht, doi:10.1007/978-94-015-8828-7_15.

Raymond, D. J., S. L. Sessions, A. H. Sobel, and Fuchs, Ž. (2009), The mechanics of gross moist stability, *Journal of Advances in Modeling Earth Systems*, *1*(3), doi: 10.3894/JAMES.2009.1.9.

Redelsperger, J.-L. (1997), The Mesoscale Organization of Deep Convection, pp. 59–98, Springer Netherlands, Dordrecht, doi:10.1007/978-94-015-8828-7_3.

Redelsperger, J.-L., F. Guichard, and S. Mondon (2000), A parameterization of mesoscale enhancement of surface fluxes for large-scale models, *Journal of Climate*, *13*(2), 402–421, doi:10.1175/1520-0442(2000)013<0402:APOMEO>2.0.CO;2.

Redelsperger, J.-L., D. B. Parsons, and F. Guichard (2002), Recovery processes and factors limiting cloud-top height following the arrival of a dry intrusion observed during TOGA COARE, *Journal of the Atmospheric Sciences*, *59*(16), 2438–2457, doi:10.1175/1520-0469(2002)059<2438:RPAFLC>2.0.CO;2.

Reed, K. A., B. Medeiros, J. T. Bacmeister, and P. H. Lauritzen (2015), Global radiative-convective equilibrium in the community atmosphere model, version 5, *Journal of the Atmospheric Sciences*, *72*(5), 2183–2197, doi:10.1175/JAS-D-14-0268.1.

Rochetin, N., J.-Y. Grandpeix, C. Rio, and F. Couvreux (2014), Deep convection triggering by boundary layer thermals. Part II: Stochastic triggering parameterization for the LMDZ GCM, *Journal of the Atmospheric Sciences*, *71*(2), 515–538, doi:10.1175/JAS-D-12-0337.1.

Rodts, S. M. A., P. G. Duynkerke, and H. J. J. Jonker (2003), Size distributions and dynamical properties of shallow cumulus clouds from aircraft observations and satellite data, *Journal of the Atmospheric Sciences*, *60*(16), 1895–1912, doi:10.1175/1520-0469(2003)060<1895:SDADPO>2.0.CO;2.

Romps, D. M. (2010), A direct measure of entrainment, *Journal of the Atmospheric Sciences*, *67*(6), 1908–1927, doi:10.1175/2010JAS3371.1.

Romps, D. M. (2011), Response of tropical precipitation to global warming, *Journal of the Atmospheric Sciences*, *68*(1), 123–138, doi:10.1175/2010JAS3542.1.

Romps, D. M., and Z. Kuang (2011), A transilient matrix for moist convection, *Journal of the Atmospheric Sciences*, *68*(9), 2009–2025, doi:10.1175/2011JAS3712.1.

Sakradzija, M., A. Seifert, and A. Dipankar (2016), A stochastic scale-aware parameterization of shallow cumulus convection across the convective gray zone, *Journal of Advances in Modeling Earth Systems*, *8*(2), 786–812, doi:10.1002/2016MS000634.

Satoh, M., and Y. Matsuda (2009), Statistics on high-cloud areas and their sensitivities to cloud microphysics using single-cloud experiments, *Journal of the Atmospheric Sciences*, *66*(9), 2659–2677, doi:10.1175/2009JAS2948.1.

Satoh, M., T. Matsuno, H. Tomita, H. Miura, T. Nasuno, and S. Iga (2008), Nonhydrostatic Icosahedral Atmospheric Model (NICAM) for global cloud resolving simulations, *Journal of Computational Physics*, *227*(7), 3486–3514, doi:10.1016/j.jcp.2007.02.006.

Satoh, M., et al. (2012), The intra-seasonal oscillation and its control of tropical cyclones simulated by high-resolution global atmospheric models, *Climate Dynamics*, *39*(9), 2185–2206, doi:10.1007/s00382-011-1235-6.

Seifert, A., and K. D. Beheng (2006), A two-moment cloud microphysics parameterization for mixed-phase clouds. Part 1: Model description, *Meteorology and Atmospheric Physics*, *92*(1), 45–66, doi:10.1007/s00703-005-0112-4.

Senf, F., and H. Deneke (2017), Uncertainties in synthetic Meteosat SEVIRI infrared brightness temperatures in the presence of cirrus clouds and implications for evaluation of cloud microphysics, *Atmospheric Research*, *183*(Supplement C), 113 – 129, doi:10.1016/j.atmosres.2016.08.012.

Sherwood, S. C., et al. (2013), *Climate Processes: Clouds, Aerosols and Dynamics*, pp. 73–103, Springer Netherlands, Dordrecht, doi:10.1007/978-94-007-6692-1_4.

Sherwood, S. C., S. Bony, and J.-L. Dufresne (2014), Spread in model climate sensitivity traced to atmospheric convective mixing, *Nature*, *505*(7481), 3742, doi: doi:10.1038/nature12829.

Siebesma, A. P. (1996), On the mass flux approach for atmospheric convection, in *Workshop on New Insights and Approaches to Convective Parametrization*, pp. 25–57, ECMWF, ECMWF, Reading, UK.

Siebesma, A. P., and J. W. M. Cuijpers (1995), Evaluation of parametric assumptions for shallow cumulus convection, *Journal of the Atmospheric Sciences*, *52*(6), 650–666, doi:10.1175/1520-0469(1995)052<0650:EOPAFS>2.0.CO;2.

Siebesma, A. P., et al. (2003), A large eddy simulation intercomparison study of shallow cumulus convection, *Journal of the Atmospheric Sciences*, *60*(10), 1201–1219, doi: 10.1175/1520-0469(2003)60<1201:ALESIS>2.0.CO;2.

Singh, M. S., and P. A. O'Gorman (2013), Influence of entrainment on the thermal stratification in simulations of radiative-convective equilibrium, *Geophysical Research Letters*, *40*(16), 4398–4403, doi:10.1002/grl.50796.

Siongco, A. C., C. Hohenegger, and B. Stevens (2017), Sensitivity of the summertime tropical Atlantic precipitation distribution to convective parameterization and model resolution in ECHAM6, *Journal of Geophysical Research: Atmospheres*, *122*(5), 2579–2594, doi:10.1002/2016JD026093, 2016JD026093.

Sobel, A. H., and C. S. Bretherton (2000), Modeling tropical precipitation in a single column, *Journal of Climate*, *13*(24), 4378–4392, doi:10.1175/1520-0442(2000)013<4378:MTPIAS>2.0.CO;2.

Soden, B. J., and G. A. Vecchi (2011), The vertical distribution of cloud feedback in coupled ocean-atmosphere models, *Geophysical Research Letters*, *38*(12), doi:10.1029/2011GL047632, l12704.

Stein, T. H. M., C. E. Holloway, I. Tobin, and S. Bony (2017), Observed relationships between cloud vertical structure and convective aggregation over tropical ocean, *Journal of Climate*, *30*(6), 2187–2207, doi:10.1175/JCLI-D-16-0125.1.

Stevens, B., and S. Bony (2013a), What are climate models missing?, *Science*, *340*(6136), 1053–1054, doi:10.1126/science.1237554.

Stevens, B., and S. Bony (2013b), Water in the atmosphere, *Physics Today*, *66*(6), 29–34, doi:10.1063/PT.3.2009.

Stevens, B., S. Bony, and M. Webb (2012), Clouds On-Off Klimate Intercomparison Experiment (COOKIE), [Available at http://www.euclipse.eu/wp4/wp4.html].

Stevens, B., et al. (2013), Atmospheric component of the MPI-M Earth System Model: ECHAM6, *Journal of Advances in Modeling Earth Systems*, *5*(2), 146–172, doi:10.1002/jame.20015.

Stevens, B., et al. (2016), The Barbados Cloud Observatory: Anchoring investigations of clouds and circulation on the edge of the ITCZ, *Bulletin of the American Meteorological Society*, *97*(5), 787–801, doi:10.1175/BAMS-D-14-00247.1.

Stevens, B., G. Drótos, T. Becker, and T. Mauritsen (2018), Tropics as tempest, to Appear in *Tropical Climate Extremes: Natural Variability and Trends*, edited by V. Vuruputur, J. Sukhatme, R. Murtugudde, and R. Roca, Elsevier.

Stommel, H. (1947), Entrainment of air into a cumulus cloud, *Journal of Meteorology*, *4*(3), 91–94, doi:10.1175/1520-0469(1947)004<0091:EOAIAC>2.0.CO;2.

Stratton, R. A., and A. J. Stirling (2012), Improving the diurnal cycle of convection in GCMs, *Quarterly Journal of the Royal Meteorological Society*, *138*(666), 1121–1134, doi:10.1002/qj.991.

Suhas, E., and G. J. Zhang (2014), Evaluation of trigger functions for convective parameterization schemes using observations, *Journal of Climate*, *27*(20), 7647–7666, doi: 10.1175/JCLI-D-13-00718.1.

Tan, J., C. Jakob, W. B. Rossow, and G. Tselioudis (2015), Increases in tropical rainfall driven by changes in frequency of organized deep convection, *Nature*, *519*(7544), 451–454, doi:10.1038/nature14339.

Taylor, C. M., R. A. M. de Jeu, F. Guichard, P. P. Harris, and W. A. Dorigo (2012), Afternoon rain more likely over drier soils, *Nature*, *489*(7416), 423–426, doi: 10.1002/2013GL058511.

Tiedtke, M. (1989), A comprehensive mass flux scheme for cumulus parameterization in large-scale models, *Monthly Weather Review*, *117*(8), 1779–1800, doi:10.1175/1520-0493(1989)117<1779:ACMFSF>2.0.CO;2.

Tobin, I., S. Bony, and R. Roca (2012), Observational evidence for relationships between the degree of aggregation of deep convection, water vapor, surface fluxes, and radiation, *Journal of Climate*, *25*, 6885–6904, doi:10.1175/JCLI-D-11-00258.1.

Tobin, I., et al. (2013), Does convective aggregation need to be represented in cumulus parameterizations?, *Journal of Advances in Modeling Earth Systems*, *5*(4), 692–703, doi:10.1002/jame.20047.

Tomassini, L., A. Voigt, and B. Stevens (2015), On the connection between tropical circulation, convective mixing, and climate sensitivity, *Quarterly Journal of the Royal Meteorological Society*, *141*(689), 1404–1416, doi:10.1002/qj.2450.

Tomita, H., and M. Satoh (2004), A new dynamical framework of nonhydrostatic global model using the icosahedral grid, *Fluid Dynamics Research*, *34*(6), 357, doi: 10.1016/j.fluiddyn.2004.03.003.

Tompkins, A. M., and G. C. Craig (1998), Radiative-convective equilibrium in a three-dimensional cloud-ensemble model, *Quarterly Journal of the Royal Meteorological Society*, *124*(550), 2073–2097, doi:10.1002/qj.49712455013.

Tompkins, A. M., and A. G. Semie (2017), Organization of tropical convection in low vertical wind shears: Role of updraft entrainment, *Journal of Advances in Modeling Earth Systems*, *9*, doi:10.1002/2016MS000802.

Turner, J. S. (1963), The motion of buoyant elements in turbulent surroundings, *Journal of Fluid Mechanics*, *16*(1), 1–16, doi:10.1017/S0022112063000549.

Vial, J., J.-L. Dufresne, and S. Bony (2013), On the interpretation of inter-model spread in CMIP5 climate sensitivity estimates, *Climate Dynamics*, *41*(11-12), 3339–3362, doi: 10.1007/s00382-013-1725-9.

Voigt, A., S. Bony, J.-L. Dufresne, and B. Stevens (2014), The radiative impact of clouds on the shift of the Intertropical Convergence Zone, *Geophysical Research Letters*, *41*(12), 4308–4315, doi:10.1002/2014GL060354.

Wagner, T. M., and H.-F. Graf (2010), An ensemble cumulus convection parameterization with explicit cloud treatment, *Journal of the Atmospheric Sciences*, *67*(12), 3854–3869, doi:10.1175/2010JAS3485.1.

Warner, J. (1955), The water content of cumuliform cloud, *Tellus*, *7*(4), 449–457, doi: 10.1111/j.2153-3490.1955.tb01183.x.

Webb, M. J., F. H. Lambert, and J. M. Gregory (2013), Origins of differences in climate sensitivity, forcing and feedback in climate models, *Climate Dynamics*, *40*(3), 677–707, doi:10.1007/s00382-012-1336-x.

Webb, M. J., et al. (2015), The impact of parametrized convection on cloud feedback, *Philosophical Transactions of the Royal Society of London A: Mathematical, Physical and Engineering Sciences*, *373*(2054), doi:10.1098/rsta.2014.0414.

Wing, A. A., and T. W. Cronin (2016), Self-aggregation of convection in long channel geometry, *Quarterly Journal of the Royal Meteorological Society*, *142*(694), 1–15, doi: 10.1002/qj.2628.

Wing, A. A., and K. A. Emanuel (2014), Physical mechanisms controlling self-aggregation of convection in idealized numerical modeling simulations, *Journal of Advances in Modeling Earth Systems*, *6*(1), 59–74, doi:10.1002/2013MS000269.

Wing, A. A., K. A. Reed, M. Satoh, B. Stevens, S. Bony, and T. Ohno (2017a), Radiative-Convective Equilibrium Model Intercomparison Project, *Geoscientific Model Development*, doi:10.5194/gmd-2017-213.

Wing, A. A., K. A. Emanuel, C. E. Holloway, and C. Muller (2017b), Convective self-aggregation in numerical simulations: A review, *Surveys in Geophysics*, doi: 10.1007/s10712-017-9408-4.

Yanai, M., S. Esbensen, and J.-H. Chu (1973), Determination of bulk properties of tropical cloud clusters from large-scale heat and moisture budgets, *Journal of the Atmospheric Sciences*, *30*(4), 611–627, doi:10.1175/1520-0469(1973)030<0611:DOBPOT>2.0.CO;2.

Zängl, G., D. Reinert, P. Rípodas, and M. Baldauf (2015), The ICON (ICOsahedral Non-hydrostatic) modelling framework of DWD and MPI-M: Description of the non-hydrostatic dynamical core, *Quarterly Journal of the Royal Meteorological Society*, *141*(687), 563–579, doi:10.1002/qj.2378.

Zhang, C., B. E. Mapes, and B. J. Soden (2003), Bimodality in tropical water vapour, *Quarterly Journal of the Royal Meteorological Society*, *129*(594), 2847–2866, doi:10.1256/qj.02.166.

Zhu, H., and H. H. Hendon (2015), Role of large-scale moisture advection for simulation of the MJO with increased entrainment, *Quarterly Journal of the Royal Meteorological Society*, *141*(691), 2127–2136, doi:10.1002/qj.2510.

Acknowledgements

First and foremost, I would like to thank my PhD supervisors Bjorn Stevens and Cathy Hohenegger, who have been the best supervisors I could have hoped for. Our meetings and spontaneous discussions were always very fruitful and motivating, but I did not only profit from their huge knowledge of the climate system, but also from their helpful advice on soft skills like presenting and writing. They also strongly supported my plans to spend a few months of my PhD abroad, at the University of Washington. In Seattle, Chris Bretherton and all the people on the 7th floor welcomed me very warmly, and I thank Chris very much for hosting me and for his excellent supervision.

Special thanks go to Stefan Bühler, who not only accepted to become my panel chair, but also an evaluator of this thesis. In addition to Stefan, Bjorn and Cathy, I thank Johanna Baehr and Jörn Peckmann for their willingness to be members of my PhD Committee. I would like to thank Angela Gruber, Antje Weitz, Wiebke Böhm and Connie Kampmann, who always had an open ear for my problems or questions, and supported me throughout the course of my PhD with administrative advice.

I would like to express my thanks to Stefan Kinne for giving me the opportunity to experience climate science from an observational point of view, on board of the research vessel Polarstern. Spending five weeks on board, going from Bremerhaven to Cape Town, and thus crossing the whole tropics, allowed me to get a good impression of tropical convection in all its variety.

I would like to thank Cathy for organizing the HErZ group meetings, as they often let to very fruitful discussion and interesting new ideas. The people in that group who I would like to thank especially are Daniel, Karsten, Mirjana, Matthias, Ann Kristin, James and Raphaela. I would like to thank Sandrine Bony, David Coppin and Gábor Drótos for some very fruitful international collaboration beyond the borders of the Max Planck Institute. Special thanks also to Ann Kristin for sharing her thesis style template with me, to Ann

Kristin, Karsten and Raphaela for some good advice on how to write the Introduction of this thesis and to Cheska and Nicolas for internally reviewing my publications.

A big thanks also to all of my office mates I had over the years, at first Katrin, who taught me a lot about how to use NCL, and Malte, for always good advice and very interesting discussions about soccer, the latest forecast for the next skiing holiday and about weather in general. I would also like to thank Hauke, who is currently at the Neumayer Station in Antarctica, for a lot of interesting discussions on all sorts of topics, and last not least I would like to thank my new office mates, Diego and Paul, for a very good, productive atmosphere in the office that allowed me to focus on writing this thesis.

I would also like to thank all the people who joined me for lunch. In the lunch breaks, we often had some very interesting discussions and a good time, which was a good motivation to focus and work productively in the afternoon. Special thanks to Akio, Matthias, Sebastian, Tobias, Bernhard and Johannes. A very big thanks also to all of my friends who always supported me. On purpose, because I would always forget someone, I do not want to thank you all by name, but I hope that you know how important you are to me and how much I value our friendship.

Last but very surely not least, I would like to thank my family, who have always supported me, not only financially during my Bachelor and Master studies, but also morally, with all the decisions I have made in my life so far. My mother, my father, my brother, my sister, my four grandparents, and all of my uncles, aunts, and cousins have always given me the feeling to be home, safe and loved when I was with them. A special thanks to my father for all the proof-reading, not only of this thesis, but also of all my publications.

Aus dieser Dissertation hervorgegangene Vorveröffentlichungen

List of Publications

Becker, T. and B. Stevens (2014): Climate and climate sensitivity to changing CO2 on an idealized land planet. *J. Adv. Model. Earth. Syst.*, **6**(4), 1205–1223, doi:10.1002/2014MS000369.

Bony, S., B. Stevens, D. Coppin, T. Becker, K. A. Reed, A. Voigt and B. Medeiros (2016): Thermodynamic control of anvil cloud amount. *Proc. Natl. Acad. Sci. U. S. A.*, **113**(32), 8927–8932, doi:10.1073/pnas.1601472113.

Becker, T., B. Stevens and C. Hohenegger (2017): Imprint of the convective parameterization and sea-surface temperature on large-scale convective self-aggregation. *J. Adv. Model. Earth. Syst.*, **9**(2), 1488–1505, doi:10.1002/2016MS000865.

Becker, T., C. S. Bretherton, C. Hohenegger and B. Stevens (2018): Estimating bulk entrainment with unaggregated and aggregated convection. *Geophys. Res. Lett.*, **45**, doi:10.1002/2017GL076640.

Stevens, B., G. Drótos, T. Becker and T. Mauritsen (2018): Tropics as Tempest, to Appear in *Tropical Climate Extremes: Natural Variability and Trends*, Venugopal Vuruputur, Jai Sukhatme, Raghu Murtugudde and Remy Roca (Editors), Elsevier.

Eidesstattliche Versicherung

Declaration on oath

Hiermit erkläre ich an Eides statt, dass ich die vorliegende Dissertationsschrift selbst verfasst und keine anderen als die angegebenen Quellen und Hilfsmittel benutzt habe.

I hereby declare, on oath, that I have written the present dissertation by myself and have not used other than the acknowledged resources and aids.

Hamburg, den 20.10.2017